

Journal of Mechanics of Materials and Structures

Volume 9, No. 4

July 2014



JOURNAL OF MECHANICS OF MATERIALS AND STRUCTURES

msp.org/jomms

Founded by Charles R. Steele and Marie-Louise Steele

EDITORIAL BOARD

ADAIR R. AGUIAR	University of São Paulo at São Carlos, Brazil
KATIA BERTOLDI	Harvard University, USA
DAVIDE BIGONI	University of Trento, Italy
IWONA JASIUK	University of Illinois at Urbana-Champaign, USA
THOMAS J. PENCE	Michigan State University, USA
YASUhide SHINDO	Tohoku University, Japan
DAVID STEIGMANN	University of California at Berkeley

ADVISORY BOARD

J. P. CARTER	University of Sydney, Australia
D. H. HODGES	Georgia Institute of Technology, USA
J. HUTCHINSON	Harvard University, USA
D. PAMPLONA	Universidade Católica do Rio de Janeiro, Brazil
M. B. RUBIN	Technion, Haifa, Israel

PRODUCTION production@msp.org

SILVIO LEVY Scientific Editor

Cover photo: Mando Gomez, www.mandolux.com

See msp.org/jomms for submission guidelines.

JoMMS (ISSN 1559-3959) at Mathematical Sciences Publishers, 798 Evans Hall #6840, c/o University of California, Berkeley, CA 94720-3840, is published in 10 issues a year. The subscription price for 2014 is US \$555/year for the electronic version, and \$710/year (+\$60, if shipping outside the US) for print and electronic. Subscriptions, requests for back issues, and changes of address should be sent to MSP.

JoMMS peer-review and production is managed by EditFLOW[®] from Mathematical Sciences Publishers.

PUBLISHED BY

 **mathematical sciences publishers**
nonprofit scientific publishing

<http://msp.org/>

© 2014 Mathematical Sciences Publishers

RANDOM VIBRATION OF SHEAR DEFORMABLE FGM PLATES

VEDAT DOGAN

In this research, the vibration of the functionally graded material (FGM) plates under random excitation is presented. The FGM plate is assumed to be moderately thick. One of the refined plate theories, the first-order shear deformable theory (FSDT) is adopted to account for the transverse shear strain. The refined form of shear correction factor is used. The plate is assumed to be simply supported along all edges with movable ends. The mechanical properties of the FGM plate are graded in the thickness direction only according to a simple power-law distribution in terms of volume fraction of constituents. Mechanical properties of constituents (ceramic and metal) of the FGM plate are assumed temperature-dependent. The FGM plate is subjected to the random pressure that is considered as a stationary and homogenous random process with zero mean and Gaussian distribution. Both the spectral density method and Monte Carlo method are used for the linear responses. Thermal effects are only included in the Monte Carlo method. The root mean square (RMS) and mean responses of the FGM plate for different plate sizes, sound pressure levels, volume fractions and temperature distributions are presented.

1. Introduction

Functionally graded materials (FGMs) are advanced inhomogeneous composite materials. The compositions of the constituents of FGMs vary smoothly and continuously in certain directions (particularly in the thickness direction), and consequently, the FGMs eliminate the interface problems such as cracks and stress concentrations encountered in the traditional laminated composite plates. FGM plates are typically made of a metal and ceramic mixture and used as structural elements in high-temperature environments.

The FGMs have attracted the considerable attention of many researchers since they were first developed in Japan three decades ago [Koizumi 1997]. To the present, extensive research has been conducted on the dynamic, static, buckling, vibration and thermal stress analysis of FGM plates. Among them, Praveen and Reddy [1998] analyzed the static and dynamic response of FGM plates by using the first-order shear deformation theory (FSDT) and the von Karman strains. The stresses and deflections of the FGM plates are examined under mechanical and thermal loadings. They found that grading of material properties is very important for the plate responses. Reddy [2000] presented a formulation for the simply supported FGM plates based on the third-order shear deformation theory and developed the associated finite element model, which includes thermomechanical coupling and geometric nonlinearities. Praveen, Chin and Reddy [Praveen et al. 1999] investigated the response of FGM cylinders to rapid heating of the inner surface with temperature-dependent material properties. The finite element formulation and axisymmetric heat equation are used. The temperature and radial/hoop stress distributions versus radial distance due to rapid heating are reported. Alijani, Bakhtiari and Amabili [Alijani et al. 2011] analyzed the nonlinear vibrations of simply supported moderately thick FGM plates in a thermal environment by

Keywords: random, vibration, FGM.

using the first-order shear deformation theory. Zhang, Hao, Guo and Chen [Zhang et al. 2012] investigated the nonlinear responses of FGM plates subjected to combined in-plane and transverse excitations by using Reddy's third-order plate theory. They found that the nonlinear responses of the FGM plates are more sensitive to transverse excitation.

Effects of the micromechanics Voigt and Mori–Tanaka models on the vibration responses of FGM plates are investigated by Shen and Wang [2012]. They used a high-order shear deformation plate theory to develop the governing equations. Since the differences between two micromechanics models were small, the Voigt model can be reasonable for finding the responses of FGM plates and shells. Nguyen-Xuan, Tran, Thai and Nguyen-Thoi [Nguyen-Xuan et al. 2012] presented a finite element approach for analysis of FGM plates subjected to mechanical and thermal loading. This method is applied in several static/dynamic problems of FGM plates.

Hosseini and Fazelzadeh [2010] presented the nonlinear vibration and the aerothermoelastic postcritical analysis of the FGM panels in a supersonic airflow. Temperature-dependent material properties are considered, and the first-order piston theory is used for the aerodynamics loading. Prakash, Singha and Ganapathi [Prakash et al. 2012] investigated the nonlinear vibration of the FGM plates by a shear flexible finite element approach. The FGM plate is modeled with the FSDT, and third-order piston theory is employed for the aerodynamics loading.

Zhao, Lee and Liew [Zhao et al. 2009] examined the mechanical and thermal buckling behavior of the FGM plates using the element-free *kp*-Ritz method. Solid plates and plates with holes are analyzed. It was determined that the hole size and volume fraction greatly influenced the buckling loads and modes. Hosseini-Hashemi, Taher, Akhavan and Omidi [Hosseini-Hashemi et al. 2010] analyzed the free vibration of the moderately thick FGM plates on elastic foundations by using the FSDT. Parametric studies regarding the elastic foundation stiffness, aspect ratios, gradient indices and thickness to length ratios are conducted. Ghannadpour, Ovesy and Nassirnia [Ghannadpour et al. 2012] presented a finite strip method for analyzing the thermal buckling of the FGM plate. The classical plate theory (CPT) is used for the formulations, and three types of thermal loadings are considered. Mohammadi, Saidi and Jomehzadeh [Mohammadi et al. 2010] studied the Levy solution for the mechanical buckling of the FGM plate based on the CPT. Thai and Choi [2012] presented a refined shear deformation theory, which is used for free vibration analysis of FGM plates on Pasternak-type foundation. Closed-form solutions for natural frequency with different boundary conditions are obtained and compared to the natural frequencies found in the literature. Dynamic, bending, thermal and vibration analysis of FGM plates by using different-order plates theories are conducted by H.-S. Shen and his associates [Yang and Shen 2003; 2002; Huang and Shen 2004]. Extensive nonlinear analysis of shear deformable FGM plates and shell can be found in [Shen 2009].

Hasheminejad and Gheshlaghi [2012] studied the transient vibration of thick FGM plates resting on the elastic foundations under blast and moving loads using the linear elasticity theory. Yang and Gao [2013] studied dynamic stress analysis of the FGM plates with a circular hole under an in-plane compressive load at infinity. Fakhari, Ohadi and Yousefian [Fakhari et al. 2011] investigated the vibrations of FGM plates with piezoelectric layers under thermal, electrical and mechanical loadings. They used the finite element method based on HSDT with geometric nonlinearity. Elishakoff and Gentilini [2005] developed a three-dimensional linear elasticity solution using the Ritz minimum energy principle for the FGM plates with all edges clamped. Mantari and Soares [2012] analytically analyzed the bending of the FGM plates by using a newly developed HSDT. Comparison studies are carried out to validate the present theory.

Lee, Zhao and Reddy [Lee et al. 2010] analyzed the postbuckling behavior of the FGM plates under mechanical in-plane edge compressive and thermal loading by using the element-free kp -method. The FSDT and von Karman-type nonlinearity are employed.

In the present study, the linear vibration of the functionally graded material (FGM) plates under random excitation is presented. One of the shear deformable plate theories, FSDT, is employed for the formulation. A modified shear correction factor is used to take into account the transverse shear strain effects. It is assumed that the FGM plate is simply supported with movable edges. The FGM plates are considered as ceramic-metal mixtures whose mechanical properties vary exponentially through the thickness only. Temperature dependency of mechanical properties of the constituents are also taken into account for the random vibration in the thermal environment. Two approaches are used for random responses in this study. The first approach is based on the normal mode method to determine the spectral density of the response, and the second approach is based on the Monte Carlo simulation of the external random pressure, the multimode Galerkin technique and the numerical integration procedure. The temperature effect is taken into account only in the second approach.

2. Structural formulation

The equations of motion of an FGM plate shown in Figure 1 using the first-order shear deformation theory (FSDT) in terms of the mid-plane displacements $u_0(x, y, t)$, $v_0(x, y, t)$ and $w_0(x, y, t)$ in the x , y and z directions, respectively, and the rotations $\phi_x(x, y, t)$ and $\phi_y(x, y, t)$ of the transverse normal about the y and x axes, respectively, can be written as [Reddy 2004]

$$A_{11}u_{0,xx} + A_{12}v_{0,xy} + B_{11}\phi_{x,xx} + B_{12}\phi_{y,yy} + A_{66}(u_{0,yy} + v_{0,yx}) + B_{66}(\phi_{x,yy} + \phi_{y,yx}) - N_{xx,x}^T = I_0(\ddot{u}_0 + c\dot{u}_0) + I_1(\ddot{\phi}_x + c\dot{\phi}_x), \quad (1)$$

$$A_{22}v_{0,yy} + A_{12}u_{0,yx} + B_{22}\phi_{y,yy} + B_{12}\phi_{x,yy} + A_{66}(u_{0,xy} + v_{0,xx}) + B_{66}(\phi_{x,xy} + \phi_{y,xx}) - N_{yy,y}^T = I_0(\ddot{v}_0 + c\dot{v}_0) + I_1(\ddot{\phi}_y + c\dot{\phi}_y), \quad (2)$$

$$\kappa A_{55}(w_{0,xx} + \phi_{x,x}) + \kappa A_{44}(w_{0,yy} + \phi_{y,y}) + \theta(w_0) + p^r(x, y, t) = I_0(\ddot{w}_0 + c\dot{w}_0), \quad (3)$$

$$B_{11}u_{0,xx} + B_{12}v_{0,xy} + D_{11}\phi_{x,xx} + D_{12}\phi_{y,xy} + B_{66}(u_{0,yy} + v_{0,xy}) + D_{66}(\phi_{x,yy} + \phi_{y,yx}) - \kappa A_{55}(w_{0,x} + \phi_x) - M_{xx,x}^T = I_2(\ddot{\phi}_x + c\dot{\phi}_x) + I_1(\ddot{u}_0 + c\dot{u}_0), \quad (4)$$

$$B_{22}v_{0,yy} + B_{12}u_{0,xy} + D_{22}\phi_{y,yy} + D_{12}\phi_{x,yx} + B_{66}(u_{0,yx} + v_{0,xx}) + D_{66}(\phi_{x,xy} + \phi_{y,xx}) - \kappa A_{44}(w_{0,y} + \phi_y) - M_{yy,y}^T = I_2(\ddot{\phi}_y + c\dot{\phi}_y) + I_1(\ddot{v}_0 + c\dot{v}_0), \quad (5)$$

where

$$\theta(w_0) = (N_{xx}w_{0,x} + N_{xy}w_{0,y})_{,x} + (N_{xy}w_{0,x} + N_{yy}w_{0,y})_{,y} \quad (6)$$

with

$$N_{xx}(x, y, t) = A_{11}u_{0,x} + A_{12}v_{0,y} + B_{11}\phi_{x,x} + B_{12}\phi_{y,y} - N_{xx}^T, \quad (7)$$

$$N_{yy}(x, y, t) = A_{12}u_{0,x} + A_{22}v_{0,y} + B_{12}\phi_{x,x} + B_{22}\phi_{y,y} - N_{yy}^T, \quad (8)$$

$$N_{xy}(x, y, t) = A_{66}(u_{0,y} + v_{0,x}) + B_{66}(\phi_{x,y} + \phi_{y,x}), \quad (9)$$

in which a subscript comma denotes the partial derivative with respect to the indicated coordinates and

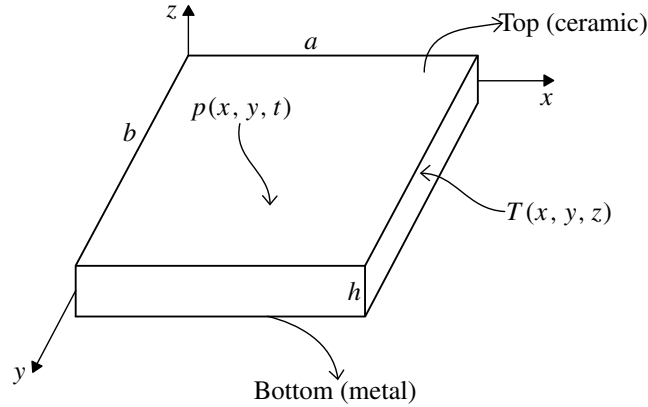


Figure 1. Shear deformable FGM plate geometry, loading and coordinate system.

time t , κ is the shear correction factor, $p^r(x, y, t)$ is the random pressure, c is the viscous damping coefficient and I_0 , I_1 and I_2 are the mass inertias defined as

$$(I_0, I_1, I_2) = \int_{-h/2}^{h/2} \rho(z, T) \cdot (1, z, z^2) dz, \quad (10)$$

in which ρ is the mass density and h is the thickness of the FGM plate. Furthermore,

$$(A_{ij}, B_{ij}, D_{ij}) = \int_{-h/2}^{h/2} Q_{ij} \cdot (1, z, z^2) dz, \quad i, j = 1, 2, 6, \quad (11)$$

$$A_{ij} = \int_{-h/2}^{h/2} Q_{ij} dz, \quad i, j = 4, 5, \quad (12)$$

where

$$\begin{aligned} Q_{11} = Q_{22} &= \frac{E(z, T)}{1 - \nu^2(z, T)}, & Q_{12} &= \frac{\nu(z, T)E(z, T)}{1 - \nu^2(z, T)}, \\ Q_{16} = Q_{26} &= 0, & Q_{44} = Q_{55} = Q_{66} &= \frac{E(z, T)}{2[1 + \nu(z, T)]}, \end{aligned} \quad (13)$$

where the elasticity modulus $E(z, T)$, the density of the plate $\rho(z, T)$, Poisson's ratio $\nu(z, T)$ and the thermal expansion coefficient $\alpha(z, T)$ are all assumed to be functions of temperature T and coordinate z in the thickness direction according to a power law distribution as [Praveen and Reddy 1998; Reddy 2000; Shen 2009]

$$E(z, T) = (E_t(T) - E_b(T)) \left(\frac{2z+h}{2h} \right)^n + E_b(T), \quad (14)$$

$$\rho(z, T) = (\rho_t(T) - \rho_b(T)) \left(\frac{2z+h}{2h} \right)^n + \rho_b(T), \quad (15)$$

$$\nu(z, T) = (\nu_t(T) - \nu_b(T)) \left(\frac{2z+h}{2h} \right)^n + \nu_b(T), \quad (16)$$

$$\alpha(z, T) = (\alpha_t(T) - \alpha_b(T)) \left(\frac{2z+h}{2h} \right)^n + \alpha_b(T), \quad (17)$$

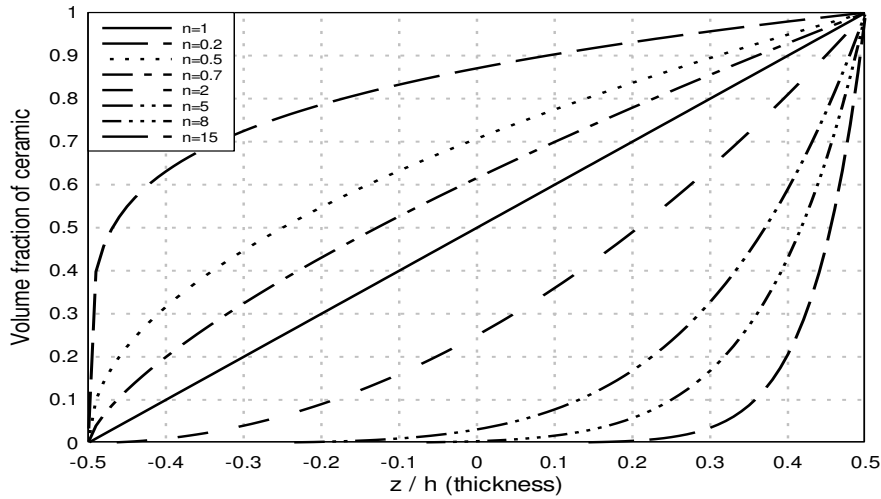


Figure 2. Volume fraction of ceramic through the thickness for the different volume fraction n .

where subscripts t and b denote the top and bottom of the plate and n is the material distribution parameter. When the material distribution parameter n increases, the volume fraction of ceramic diminishes and the FGM plate becomes more metal-rich as shown in Figure 2. The temperature dependent material properties $P(T)$ of the constituents of the FGM plate can be expressed by [Reddy and Chin 1998]

$$P(T) = P_0(P_{-1}T^{-1} + 1 + P_1T + P_2T^2 + P_3T^3), \tag{18}$$

where P_0, P_{-1}, P_1, P_2 and P_3 are the coefficients of temperature T (in K) in the cubic fit of the material property and are unique to the materials.

The shear correction factor for an FGM plate can be defined as [Efraim and Eisenberger 2007; Efraim 2011]

$$\kappa(T) = \frac{5}{6 - (\nu_1(T)V_1 - \nu_2(T)V_2)}, \tag{19}$$

where V_1 and V_2 are the volume fractions of constituents in the whole cross-section.

In this study, a simply supported FGM plate with movable ends is considered. For an FSTD plate, the boundary conditions are given as follows. At $x = 0, a$,

$$v_0(x, y, t) = w_0(x, y, t) = \phi_y(x, y, t) = 0, \tag{20}$$

$$N_{xx}(x, y, t) = A_{11}u_{0,x} + A_{12}v_{0,y} + B_{11}\phi_{x,x} + B_{12}\phi_{y,y} - N_{xx}^T = 0, \tag{21}$$

$$M_{xx} = B_{11}u_{0,x} + B_{12}v_{0,y} + D_{11}\phi_{x,x} + D_{12}\phi_{y,y} - M_{xx}^T = 0. \tag{22}$$

At $y = 0, b$,

$$u_0(x, y, t) = w_0(x, y, t) = \phi_x(x, y, t) = 0, \tag{23}$$

$$N_{yy}(x, y, t) = A_{12}u_{0,x} + A_{22}v_{0,y} + B_{12}\phi_{x,x} + B_{22}\phi_{y,y} - N_{yy}^T = 0, \tag{24}$$

$$M_{yy} = B_{12}u_{0,x} + B_{22}v_{0,y} + D_{12}\phi_{x,x} + D_{22}\phi_{y,y} - M_{yy}^T = 0, \tag{25}$$

where the thermal force and moment resultants are

$$\left(\left\{ \begin{matrix} N_{xx}^T \\ N_{yy}^T \\ N_{xy}^T \end{matrix} \right\}, \left\{ \begin{matrix} M_{xx}^T \\ M_{yy}^T \\ M_{xy}^T \end{matrix} \right\} \right) = \int_{-h/2}^{h/2} \left\{ \begin{matrix} (Q_{11} + Q_{12})\alpha(z, T) \\ (Q_{12} + Q_{22})\alpha(z, T) \\ 0 \end{matrix} \right\} \cdot \Delta T(x, y, z) \cdot (1, z) dz, \quad (26)$$

where ΔT is the temperature change from a stress-free state.

3. Solution procedure

For undamped free vibration analysis, by setting all mechanical and thermal loads to zero, it can be shown that the following functions satisfy the boundary conditions (20)–(25) [Reddy 2000]:

$$u_0(x, y, t) = \widehat{U} \cos(\alpha_m x) \sin(\beta_n y) e^{i\omega t}, \quad (27)$$

$$v_0(x, y, t) = \widehat{V} \sin(\alpha_m x) \cos(\beta_n y) e^{i\omega t}, \quad (28)$$

$$w_0(x, y, t) = \widehat{W} \sin(\alpha_m x) \sin(\beta_n y) e^{i\omega t}, \quad (29)$$

$$\phi_x(x, y, t) = \widehat{X} \cos(\alpha_m x) \sin(\beta_n y) e^{i\omega t}, \quad (30)$$

$$\phi_y(x, y, t) = \widehat{Y} \sin(\alpha_m x) \cos(\beta_n y) e^{i\omega t}, \quad (31)$$

where

$$\alpha_m = \frac{m\pi}{a} \quad \text{and} \quad \beta_n = \frac{n\pi}{b}. \quad (32)$$

By substituting (27)–(31) into the equations of motion, (1)–(5), one can obtain

$$([K] - \omega^2[M])\{\psi\} = 0, \quad (33)$$

where

$$\{\psi\} = \{\widehat{U}, \widehat{V}, \widehat{W}, \widehat{X}, \widehat{Y}\}^T \quad (34)$$

and $[K]$ and $[M]$ are the stiffness and mass matrices, and ω is the natural frequency of the vibration. Elements of the stiffness and mass matrices are given in Appendix A.

For each (m, n) , there are five natural frequencies ω_{mni}^2 and corresponding natural modes $\{\widehat{U}_{mni}, \widehat{V}_{mni}, \widehat{W}_{mni}, \widehat{X}_{mni}, \widehat{Y}_{mni}\}^T$ ($i = 1, 2, 3, 4, 5$).

Random vibration.

Isothermal case. For the random forced vibration without thermal effect, the responses are expanded in terms of natural modes [Cederbaum et al. 1992; Elishakoff 1999]

$$u_0(x, y, t) = \sum_m \sum_n \sum_{i=1}^5 U_{mni}(x, y) q_{mni}(t), \quad (35)$$

$$v_0(x, y, t) = \sum_m \sum_n \sum_{i=1}^5 V_{mni}(x, y) q_{mni}(t), \quad (36)$$

$$w_0(x, y, t) = \sum_m \sum_n \sum_{i=1}^5 W_{mni}(x, y) q_{mni}(t), \quad (37)$$

$$\phi_x(x, y, t) = \sum_m \sum_n \sum_{i=1}^5 X_{mni}(x, y) q_{mni}(t), \quad (38)$$

$$\phi_y(x, y, t) = \sum_m \sum_n \sum_{i=1}^5 Y_{mni}(x, y) q_{mni}(t), \quad (39)$$

where

$$U_{mni}(x, y) = \widehat{U}_{mni} \cos(\alpha_m x) \sin(\beta_n y), \quad (40)$$

$$V_{mni}(x, y) = \widehat{V}_{mni} \sin(\alpha_m x) \cos(\beta_n y), \quad (41)$$

$$W_{mni}(x, y) = \widehat{W}_{mni} \sin(\alpha_m x) \sin(\beta_n y), \quad (42)$$

$$X_{mni}(x, y) = \widehat{X}_{mni} \cos(\alpha_m x) \sin(\beta_n y), \quad (43)$$

$$Y_{mni}(x, y) = \widehat{Y}_{mni} \sin(\alpha_m x) \cos(\beta_n y) \quad (44)$$

by introducing (35)–(39) into (1)–(5); and using free vibration analysis and orthogonality of eigenmodes, one can obtain

$$\ddot{q}_{mni} + 2\xi_{mni}\omega_{mni}\dot{q}_{mni} + \omega_{mni}^2 q_{mni} = Q_{mni}^r, \quad (45)$$

where

$$2\xi_{mni}\omega_{mni} = c \quad (46)$$

and the generalized random force

$$Q_{mni}^r(t) = \frac{1}{M_{mni}} \int_0^a \int_0^b p^r(x, y, t) W_{mni}(x, y) dx dy, \quad (47)$$

where the generalized mass

$$M_{mni} = \int_0^a \int_0^b \{I_0(U_{mni}^2 + V_{mni}^2 + W_{mni}^2) + 2I_1(X_{mni}U_{mni} + Y_{mni}V_{mni}) + I_2(X_{mni}^2 + Y_{mni}^2)\} dx dy. \quad (48)$$

By using random vibration theory [Lin 1976; Elishakoff 1999; Maymon 1998], the deflection response spectral density for $w_0(x, y, t)$ can be derived as

$$S_{WW}(x_1, y_1, x_2, y_2, \omega) = \sum_{mni} \sum_{rsj} W_{mni}(x_1, y_1) W_{rsj}(x_2, y_2) H_{mni}(\omega) H_{rsj}^*(\omega) S_{Q_{mni}^r Q_{rsj}^r}(\omega), \quad (49)$$

where

$$S_{Q_{mni}^r Q_{rsj}^r}(\omega) = \frac{1}{M_{mni}} \frac{1}{M_{rsj}} \int_0^a \int_0^b \int_0^a \int_0^b S_p(x_1, y_1, x_2, y_2, \omega) W_{mni}(x_1, y_1) W_{rsj}(x_2, y_2) dx_1 dy_1 dx_2 dy_2 \quad (50)$$

and

$$H_{mni}(\omega) = \frac{1}{\omega_{mni}^2 [\omega_{mni}^2 - \omega^2 + 2i\xi_{mni}\omega_{mni}\omega]}, \quad (51)$$

and * indicates a complex conjugate. We define

$$R_{WW}(x_1, y_1, x_2, y_2, \tau) = \int_{-\infty}^{\infty} S_{WW}(x_1, y_1, x_2, y_2, \omega) e^{i\omega\tau} d\omega. \quad (52)$$

The root mean square (RMS) values of deflection at a point ($x = x_1 = x_2$ and $y = y_1 = y_2$) can be computed from

$$\text{RMS} = \sqrt{\int_{-\infty}^{\infty} S_{ww}(x, y, \omega) d\omega}. \quad (53)$$

Thermal case. When thermal effects are included, due to multiplication of thermal terms and deflection terms, a time domain approach is used to develop the solution. For the time domain solution, displacements are expanded into double Fourier series as

$$u_0(x, y, t) = \sum_m \sum_n U_{mn}(t) \cos(\alpha_m x) \sin(\beta_n y), \quad (54)$$

$$v_0(x, y, t) = \sum_m \sum_n V_{mn}(t) \sin(\alpha_m x) \cos(\beta_n y), \quad (55)$$

$$w_0(x, y, t) = \sum_m \sum_n W_{mn}(t) \sin(\alpha_m x) \sin(\beta_n y), \quad (56)$$

$$\phi_x(x, y, t) = \sum_m \sum_n X_{mn}(t) \cos(\alpha_m x) \sin(\beta_n y), \quad (57)$$

$$\phi_y(x, y, t) = \sum_m \sum_n Y_{mn}(t) \sin(\alpha_m x) \cos(\beta_n y), \quad (58)$$

where

$$\alpha_m = \frac{m\pi}{a} \quad \text{and} \quad \beta_n = \frac{n\pi}{b}. \quad (59)$$

Temperature in (26) is also expanded in a double Fourier sine series as

$$T(x, y, z) = \sum_{m=1} \sum_{n=1} T_{mn}(z) \sin(\alpha_m x) \sin(\beta_n y), \quad (60)$$

where

$$T_{mn}(z) = \frac{4}{a \cdot b} \int_0^a \int_0^b T(x, y, z) \sin(\alpha_m x) \sin(\beta_n y) dx dy. \quad (61)$$

It is also assumed that temperature varies only in the z direction or uniformly throughout the plate. Then the temperature change can be written in the form

$$\Delta T(x, y, z) = \Delta T(z) \sum_m \sum_n \frac{1}{m \cdot n} \sin(\alpha_m x) \sin(\beta_n y), \quad (62)$$

where

$$\Delta T(z) = T(z) - T_0, \quad (63)$$

where T_0 is a stress-free reference temperature ($T_0 = 300$ K is taken).

The following temperature distributions through the thickness (z direction) in (63) are considered. For linear distribution,

$$T(z) = T_b + (T_t - T_b) \left(\frac{2z + h}{2h} \right), \quad (64)$$

where T_b and T_t are the temperatures of the bottom and top of the FGM plate, respectively. For nonlinear distribution of the temperature through the thickness, the heat conduction equation

$$-\frac{d}{dz} \left(k(z) \frac{dT}{dz} \right) = 0 \quad (65)$$

is solved, where the temperature dependency of the thermal conductivity k is not considered. Solution of (65) is carried out by using polynomial series as [Javaheri and Eslami 2002]

$$T(z) = T_b + \frac{T_t - T_b}{C_{tb}} \left[V - \frac{k_{tb}}{(n+1)k_b} V^{n+1} + \frac{k_{tb}^2}{(2n+1)k_b^2} V^{2n+1} - \frac{k_{tb}^3}{(3n+1)k_b^3} V^{3n+1} + \frac{k_{tb}^4}{(4n+1)k_b^4} V^{4n+1} - \frac{k_{tb}^5}{(5n+1)k_b^5} V^{5n+1} \right], \quad (66)$$

where

$$C_{tb} = 1 - \frac{k_{tb}}{(n+1)k_b} + \frac{k_{tb}^2}{(2n+1)k_b^2} - \frac{k_{tb}^3}{(3n+1)k_b^3} + \frac{k_{tb}^4}{(4n+1)k_b^4} - \frac{k_{tb}^5}{(5n+1)k_b^5} \quad (67)$$

and

$$V = \frac{2z + h}{2h} \quad \text{and} \quad k_{tb} = k_t - k_b, \quad (68)$$

where k_b and k_t are the thermal conductivity of the bottom and top surfaces of the plate, respectively. Above, n is the material distribution parameter as used in (14)–(17).

The assumed solutions that satisfy the boundary conditions, (20)–(25), are substituted into (1)–(5), then Galerkin's method is employed and the following sets of equations in time domain are obtained:

$$\begin{aligned} \ddot{U}_{mn} + 2\xi_{mn}\omega_{mn}\dot{U}_{mn} + \frac{I_1}{I_0}(\ddot{X}_{mn} + 2\xi_{mn}\omega_{mn}\dot{X}_{mn}) \\ + \frac{1}{I_0} \left(k_{11}U_{mn} + k_{12}V_{mn} + k_{14}X_{mn} + k_{15}Y_{mn} + \bar{N}_{xx}^T \frac{\pi}{n \cdot a} \Big|_{n \text{ odd}} \right) = 0, \end{aligned} \quad (69)$$

$$\begin{aligned} \ddot{V}_{mn} + 2\xi_{mn}\omega_{mn}\dot{V}_{mn} + \frac{I_1}{I_0}(\ddot{Y}_{mn} + 2\xi_{mn}\omega_{mn}\dot{Y}_{mn}) \\ + \frac{1}{I_0} \left(k_{21}U_{mn} + k_{22}V_{mn} + k_{24}X_{mn} + k_{25}Y_{mn} + \bar{N}_{yy}^T \frac{\pi}{m \cdot b} \Big|_{m \text{ odd}} \right) = 0, \end{aligned} \quad (70)$$

$$\begin{aligned} \ddot{W}_{mn} + 2\xi_{mn}\omega_{mn}\dot{W}_{mn} + \frac{1}{I_0}(k_{33}W_{mn} + k_{34}X_{mn} + k_{35}Y_{mn}) \\ + \bar{N}_{xx}^T \sum_{k \text{ odd}} \sum_{l \text{ odd}} \sum_r \sum_s W_{rs} \frac{\alpha_r}{k \cdot l} \xi_1(l, s, n) [\alpha_r \gamma_1(k, r, m) - \alpha_k \gamma_2(k, r, m)] \\ + \bar{N}_{yy}^T \sum_{k \text{ odd}} \sum_{l \text{ odd}} \sum_r \sum_s W_{rs} \frac{\beta_s}{k \cdot l} \gamma_1(k, r, m) [\beta_s \xi_1(l, s, n) - \beta_l \xi_2(l, s, n)] = Q_{mn}(t), \end{aligned} \quad (71)$$

$$\ddot{X}_{mn} + 2\xi_{mn}\omega_{mn}\dot{X}_{mn} + \frac{I_1}{I_2}(\ddot{U}_{mn} + 2\xi_{mn}\omega_{mn}\dot{U}_{mn}) + \frac{1}{I_2}\left(k_{41}U_{mn} + k_{42}V_{mn} + k_{43}W_{mn} + k_{44}X_{mn} + k_{45}Y_{mn} + \bar{M}_{xx}^T \frac{\pi}{n \cdot a} \Big|_{n \text{ odd}}\right) = 0, \quad (72)$$

$$\ddot{Y}_{mn} + 2\xi_{mn}\omega_{mn}\dot{Y}_{mn} + \frac{I_1}{I_2}(\ddot{V}_{mn} + 2\xi_{mn}\omega_{mn}\dot{V}_{mn}) + \frac{1}{I_2}\left(k_{51}U_{mn} + k_{52}V_{mn} + k_{53}W_{mn} + k_{54}X_{mn} + k_{55}Y_{mn} + \bar{M}_{yy}^T \frac{\pi}{m \cdot a} \Big|_{m \text{ odd}}\right) = 0, \quad (73)$$

where the generalized random load

$$Q_{mn}(t) = \frac{4}{a \cdot b \cdot I_0} \int_0^a \int_0^b p^r(x, y, t) \sin(\alpha_m x) \sin(\beta_n y) dx dy \quad (74)$$

the coefficients $\gamma_1, \gamma_2, \xi_1$ and ξ_2 are given in Appendix B and

$$\left(\begin{matrix} \left\{ \bar{N}_{xx}^T \right\} \\ \left\{ \bar{N}_{yy}^T \right\} \\ \left\{ \bar{N}_{xy}^T \right\} \end{matrix} \right), \left(\begin{matrix} \left\{ \bar{M}_{xx}^T \right\} \\ \left\{ \bar{M}_{yy}^T \right\} \\ \left\{ \bar{M}_{xy}^T \right\} \end{matrix} \right) = \int_{-h/2}^{h/2} \begin{matrix} (Q_{11} + Q_{12})\alpha(z, T) \\ (Q_{12} + Q_{22})\alpha(z, T) \\ 0 \end{matrix} \cdot \Delta T(z) \cdot (1, z) dz. \quad (75)$$

In order to solve (69)–(73), the random pressure is first simulated in the space-time domain and then the generalized random load in (74) is evaluated numerically. The integration can be carried out in a closed form for some special cases. In this study, uniformly distributed random pressure is considered.

4. Numerical examples and discussion

A moderately thick square FGM plate shown in Figure 1 is considered in this section. The square plate has a length of $a = b = 0.5$ m and a thickness of $h = 0.025$ m. The FGM plate is assumed to be simply supported with movable edges. First nine modes are retained in the serial expansion to estimate the deflection responses. Deflection responses are computed at the center of the plate (i.e., $x = a/2$ and $y = b/2$). The plate is made of the functionally graded material that is a mixture of the material combination of zirconia (ZrO_2) and titanium alloy (Ti-6Al-4V). Temperature-dependent material properties of these constituents are presented in Table 1 and used in (18).

Materials	Property	P_0	P_{-1}	P_1	P_2	P_3
Zirconia	E	244.27×10^9	0	-1.371×10^{-3}	1.214×10^{-6}	-3.681×10^{-10}
	ν	0.2882	0	-1.133×10^{-4}	0	0
	α	12.766×10^{-6}	0	-1.491×10^{-3}	1.006×10^{-5}	-6.778×10^{-11}
	ρ	5700	0	0	0	0
Ti-6Al-4V	E	122.56×10^9	0	-4.586×10^{-4}	0	0
	ν	0.2884	0	1.121×10^{-4}	0	0
	α	7.5788×10^{-6}	0	6.638×10^{-4}	-3.147×10^{-6}	0
	ρ	4429	0	0	0	0

Table 1. Temperature-dependent material properties of ceramic (zirconia) and metal (titanium) [Praveen et al. 1999; Shen 2009; Reddy and Chin 1998].

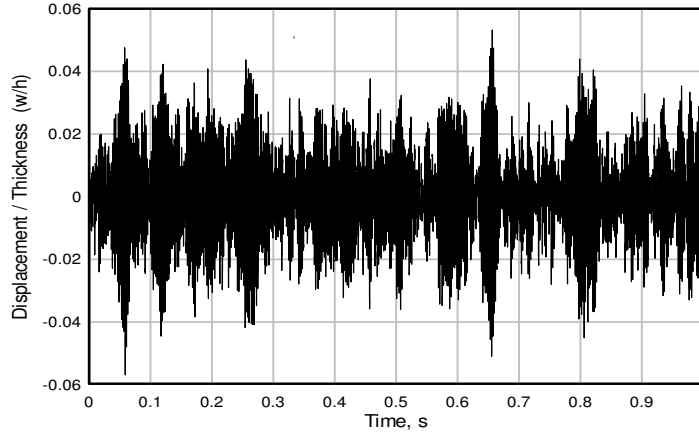


Figure 3. Displacement time histories for uniform random pressure (SPL = 160 dB and $n = 0.7$).

The random pressure acting on the top of the plate (ceramic-rich part) is simulated by using the Monte Carlo simulation technique. Uniformly distributed stationary Gaussian random pressure can be simulated as [Shinozuka and Jan 1972]

$$p^r(t_q) = \text{Re} \left[\sum_{r=0}^{M-1} A_r e^{i\phi_r} e^{i\omega_r t_q} \right], \quad (76)$$

where the ϕ_r are independent random phase angles uniformly distributed between 0 and 2π , the ω_r are the frequencies at which the values of spectral density are selected, $M = 2^m$ is the number of simulated points in time, m is a positive integer, $t_q = q\Delta t$, where Δt is time interval and $q = 0, 1, 2, \dots, M-1$, and

$$A_r = [2S_p(\omega)\Delta\omega]^{1/2}, \quad (77)$$

where S_p is the spectral density corresponding to random pressure and $\Delta\omega$ is the frequency bandwidth. The spectral density of the random pressure that is considered uniformly distributed stationary truncated Gaussian white noise is

$$S_p = \begin{cases} S_0 & \text{for } 0 \leq \omega \leq \omega_u, \\ 0 & \text{otherwise,} \end{cases} \quad (78)$$

where S_0 represents random loading intensities, ω is the frequency and ω_u is the upper cut-off frequency. The random load intensities are expressed as

$$S_0 = \begin{cases} \frac{p_0^2}{\Delta\omega} 10^{\text{SPL}/10} & \text{for } 0 \leq \omega \leq \omega_u, \\ 0 & \text{otherwise,} \end{cases} \quad (79)$$

where p_0 is the reference pressure ($p_0 = 2 \times 10^{-5}$ Pa) and SPL is the sound pressure level expressed in decibels.

In the numerical examples, the random pressure is simulated by using $M = 32768$, $\Delta t = 0.0000305$ s, $\omega_u = 2\pi \times 8192$ rad/s and $\Delta\omega = 2\pi$ rad/s.

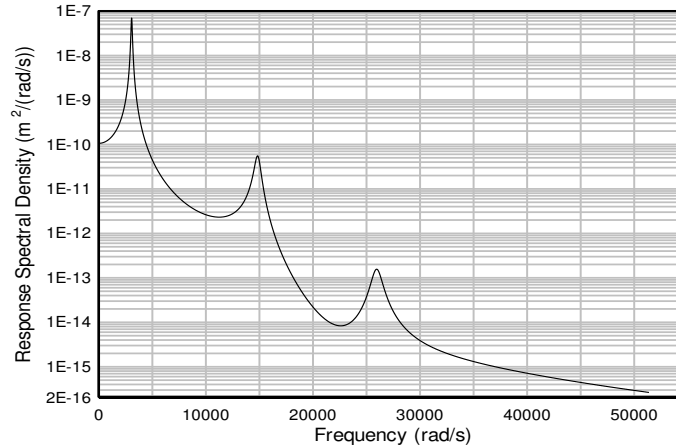


Figure 4. Spectral density of deflection response under random pressure of SPL = 160 dB ($n = 0.7$).

Figure 3 shows the midpoint deflection response history of the FGM plate for SPL = 160 dB without a temperature effect (i.e., at a reference temperature of $T_0 = 300$ K). The random response peak can reach $w_{\max}/h = 0.053$ at $t = 0.65$ s and $w_{\min}/h = -0.056$ at $t = 0.058$ s; and “the average values” of the responses are $\text{RMS}/h = 0.00148$ and $\text{MEAN}/h \cong 0$. It is evident that the plate vibrates about the plate neutral position since the random input pressure has a Gaussian distribution with zero mean.

The spectral density of the deflection response is displayed in Figure 4. This figure is plotted using (49). There are three peaks that correspond to four natural frequencies of $\omega_{11} = 3048$ rad/s, $\omega_{13} = \omega_{31} = 14816$ rad/s and $\omega_{33} = 25911$ rad/s. Even modes do not contribute to the response at the midpoint since the plate is a square. To demonstrate the contribution of different modes to the RMS response, the area under S_{WW} (as in (53)) is plotted in Figure 5 by integrating the curve in Figure 4 in the frequency domain. It is clear that contribution of the higher modes is very small since the area is not notably increased by increased frequencies beyond the fundamental frequency ω_{11} .

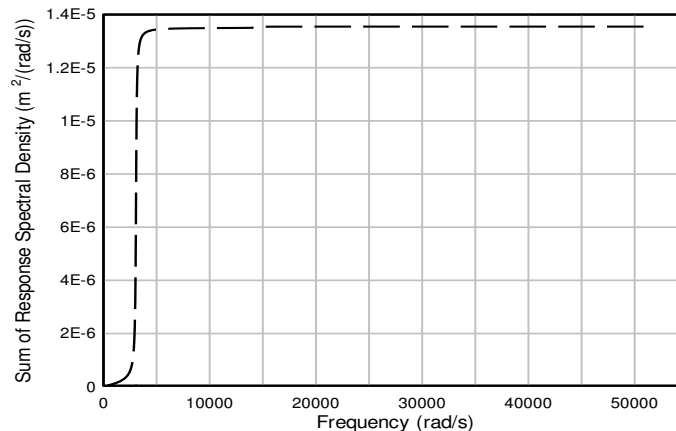


Figure 5. Integration of spectral density function.

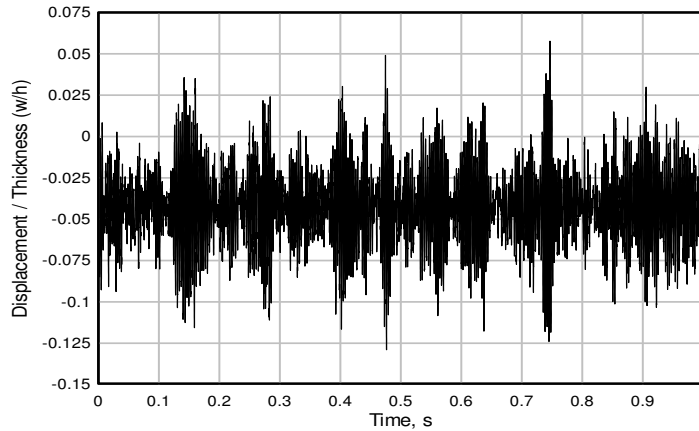


Figure 6. Displacement time history for uniform elevated temperature ($\Delta T = 300$ K) and random pressure (SPL = 160 dB and $n = 0.7$).

The deflection response for random pressure of SPL = 160 dB at the uniformly elevated temperature throughout the plate ($\Delta T = 300$ K) is presented in Figure 6. As can be seen from the figure, temperature rise in the inhomogeneous FGM plate with movable ends causes the plate to bend, and consequently, the mean value of the vibration is no longer zero. The plate first is bent due to elevated temperature to $\text{MEAN}/h = -0.0424$, and then it continues to vibrate about this mean value with $\text{RMS}/h = 0.049$ due to the random pressure.

Similar behavior is seen under the linearly varying temperature through thickness at the same random pressure (SPL = 160 dB) as displayed in Figure 7. In this case, temperature at the top face of the plate is $T_t = 850$ K and temperature at the bottom face of the plate is $T_b = 350$ K, and temperature variation from top to bottom is linear with ambient temperature $T_0 = 300$ K. In this case too, the plate bends due to temperature rise in the inhomogeneous FGM plate to a new position where it continues to vibrate randomly. The response averages are $\text{MEAN}/h = -0.0086$ and $\text{RMS}/h = 0.024$.

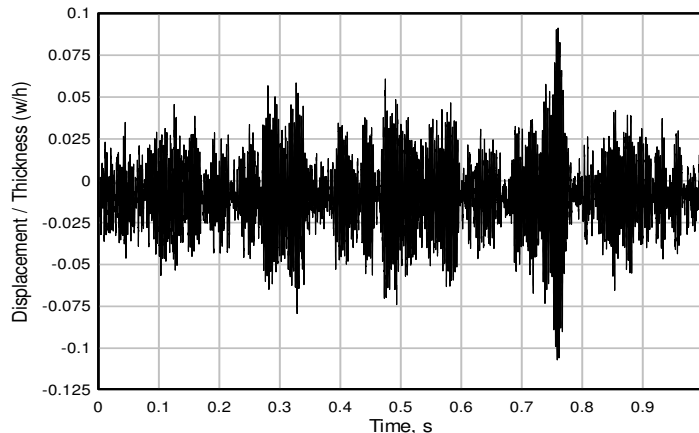


Figure 7. Displacement time history for linear temperature rise ($T_{\text{top}} = 850$ K and $T_b = 350$ K) and uniform random pressure (SPL = 160 dB, $n = 0.7$ and $T_0 = 300$ K).

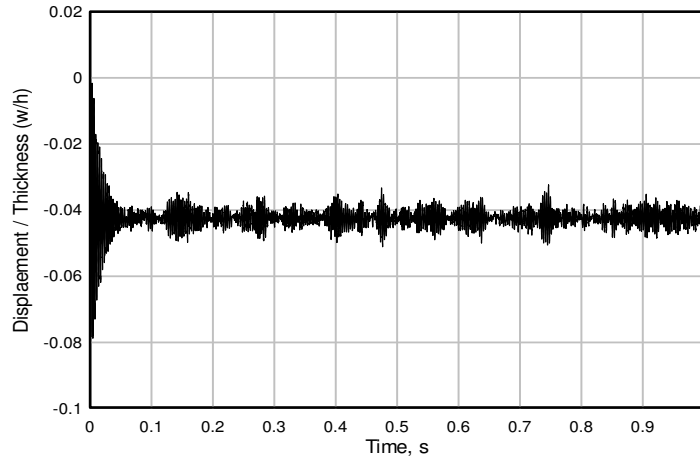


Figure 8. Displacement time history for uniform elevated temperature ($\Delta T = 300$ K) and random pressure (SPL = 140 dB and $n = 0.7$).

The displacement response history of the FGM plate under the random pressure (SPL = 140 dB) at uniformly elevated temperature ($\Delta T = 300$ K) is illustrated in Figure 8. In this case, the temperature rise is the same, but random pressure is lower compared to Figure 6. Therefore, the mean deflection response of the FGM plate is the same, but the amplitudes of the random vibration are much smaller. It turns to be like a static response as time goes. Similar behavior, but to a lesser degree, is observed for linearly varying temperature rise as shown in Figure 9. This can be realized by comparing Figures 7 and 9. It is obvious that the response is dominated by the thermal deflections when the random load density is low.

The deflection average responses of the FGM plate under different random loading at different uniformly elevated temperature are plotted in Figure 10. For without thermal effect, the mean response is almost zero, and the RMS value varies linearly with random sound pressure level as is expected for

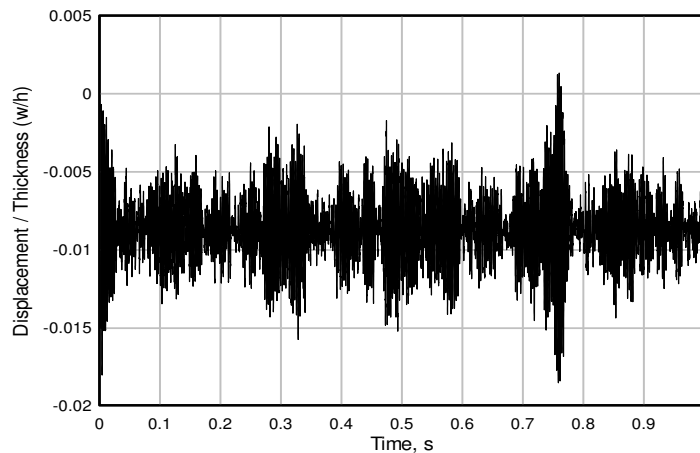


Figure 9. Displacement time history for linear temperature rise ($T_{\text{top}} = 850$ K and $T_b = 350$ K) and uniform random pressure (SPL = 140 dB, $n = 0.7$ and $T_0 = 300$ K).

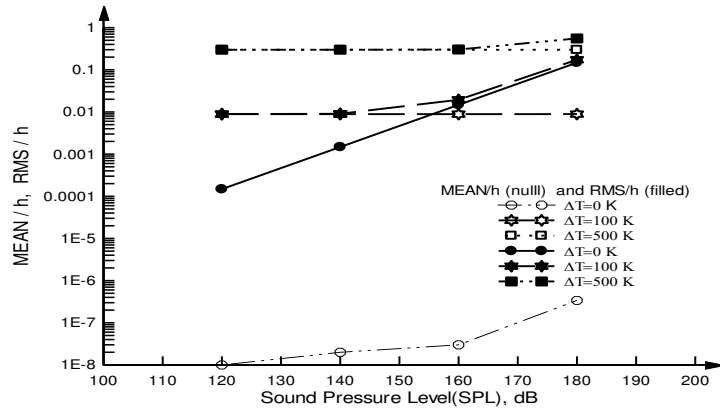


Figure 10. Deflection RMS and MEAN values versus sound pressure levels at different uniformly elevated temperatures ($n = 0.7$).

a linear structure. For other elevated temperature cases, when the SPL is less than 140 dB, thermal deflection dominates the response with the mean. However, random loading response turns out to be predominant after SPL = 140 dB at $\Delta T = 100$ K and after SPL = 160 dB at $\Delta T = 500$ K.

Similar RMS responses are obtained for linearly elevated temperatures as shown in Figure 11. The bottom temperature is kept constant at $T_b = 350$ K, and the top temperature is elevated from the ambient temperature (i.e., $\Delta T_t = T_t - T_0$). The results reveal that the RMS responses increase for all linearly elevated temperatures when the sound pressure level is greater than 140 dB.

The effect of the material distribution parameter n on the RMS/ h response under random pressure without thermal influence is presented in Table 2. Both the Monte Carlo method and spectral density method results are tabulated. It is obvious that the two methods agree quite well. The FGM plate transforms from the ceramic-rich plate to the metal-rich plate with increased material distribution parameter n . Consequently, it yields greater RMS responses.

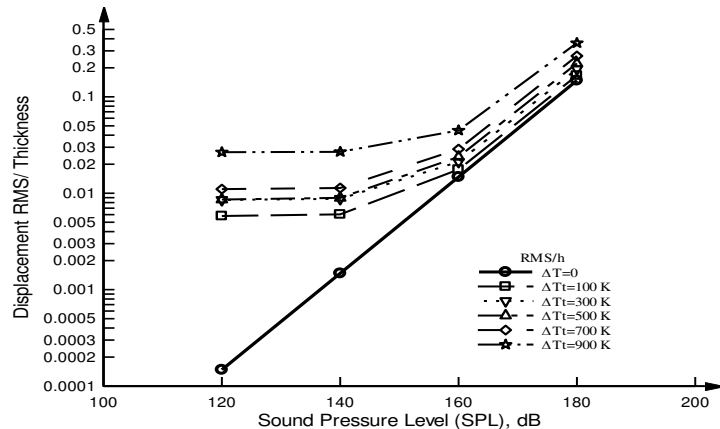


Figure 11. Deflection RMS values versus sound pressure levels at different linearly elevated temperatures ($n = 0.7$).

Method	SPL	$n = 0.1$	$n = 0.5$	$n = 1$	$n = 5$	$n = 10$
Monte Carlo	160 dB	0.0130	0.0143	0.0152	0.0167	0.0172
Spectral density	160 dB	0.0129	0.0143	0.0151	0.0166	0.0172
Monte Carlo	180 dB	0.1302	0.1434	0.1523	0.1675	0.1728
Spectral density	180 dB	0.1296	0.1430	0.1517	0.1669	0.1729

Table 2. The effect of the material distribution parameter n on the RMS/ h response ($\Delta T = 0$).

The effect of the material distribution parameter n on the nondimensional RMS and MEAN responses under random loading in a thermal environment is given in Table 3. Temperature distribution through thickness is assumed to be linear with $T_t = 850$ K and $T_b = 350$ K. The mean responses are due to temperature since MEAN responses are almost the same for SPL = 160 dB and SPL = 180 dB for each n value. The RMS values increase with increased n values as the FGM plate becomes more metal-rich.

The effect of the plate thickness to random response for SPL = 160 dB is presented in Table 4. Isothermal, uniformly elevated temperature and linearly elevated temperature cases are considered. For the isothermal vibration case, MEAN responses are zero, and the RMS responses increase with the length-to-thickness ratio. For vibration in a thermal environment, when the plate is very thick (e.g., $a/h = 5$), the response is mainly MEAN response due to elevated temperature, and fluctuations about the mean response due to random loading is very small. When the FGM plate is moderately thick, fluctuations become relatively important for the linearly elevated temperature case but not important for uniformly elevated temperatures.

Sound pressure		$n = 0.1$	$n = 0.5$	$n = 1$	$n = 5$	$n = 10$
160 dB	RMS/ h	0.0218	0.0215	0.0271	0.0285	0.0306
	MEAN/ h	0.0114	-0.0034	-0.0139	-0.0079	0.0089
180 dB	RMS/ h	0.1868	0.2129	0.2325	0.2739	0.2926
	MEAN/ h	0.0115	-0.0034	-0.0138	-0.0079	0.0089

Table 3. The effect of the material distribution parameter n on the response averages for linearly elevated temperature.

		$a/h = 5$	$a/h = 10$	$a/h = 20$
Isothermal $\Delta T = 0$ K	RMS/ h	0.000132	0.00134	0.0148
	MEAN/ h	0	0	0
Uniform temperature rise $\Delta T = 300$ K	RMS/ h	0.00127	0.00596	0.04893
	MEAN/ h	-0.00126	-0.00571	-0.04238
Linear temperature rise $T_t = 850$ K, $T_b = 350$ K	RMS/ h	0.00036	0.00218	0.02326
	MEAN/ h	-0.00033	-0.00146	-0.00861

Table 4. Random responses of the FGM plates with various length-to-thickness ratios ($n = 0.7$ and $a = 0.5$ m).

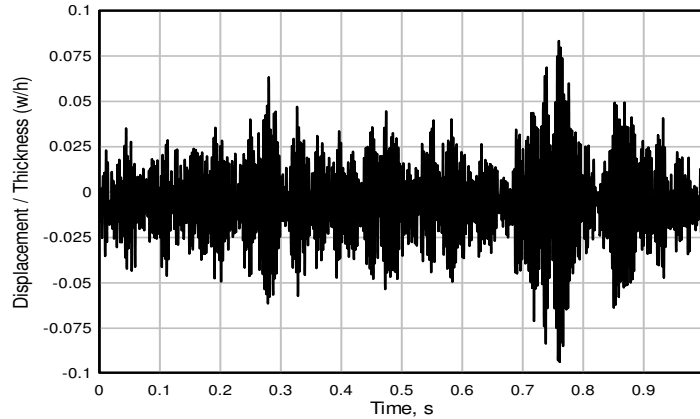


Figure 12. Displacement time history for nonlinear temperature rise ($T_t = 850$ K and $T_b = 350$ K) and random pressure (SPL = 160 dB, $n = 0.7$ and $T_0 = 300$ K).

Random response with nonlinear temperature distribution across the thickness is shown in Figure 12. In this case, temperatures of the top and bottom faces are taken to be the same as in the linear temperature distribution case shown in Figure 6. That is, temperature at the top face of the plate is $T_t = 850$ K and temperature at the bottom face of the plate is $T_b = 350$ K, and temperature variation from top to bottom is nonlinear with ambient temperature $T_0 = 300$ K, $k_b = 6.112$ W/mK and $k_t = 1.775$ W/mK in Figure 12. The response averages are found as $\text{MEAN}/h = -0.0058$ and $\text{RMS}/h = 0.021$. It can be seen that random deflection responses for linear temperature distribution (Figure 7) and nonlinear temperature distribution (Figure 12) across the plate thickness are nearly identical. It is clear that the nonlinear temperature distribution on the random response has no pronounced effect.

5. Conclusion

The transverse vibration of the functionally graded material plates under random excitation is presented. The first-order shear deformation (FSDT) plate theory is used for the equation of motion. The FGM plates are assumed as ceramic-metal mixtures, and their mechanical properties vary exponentially through the thickness. All mechanical properties of the constituents are also considered temperature-dependent. Both the spectral density method (frequency domain) and Monte Carlo method (time domain) are used for investigation. It was found that when the input is uniformly distributed random pressure with zero mean in an isothermal environment, the response is also random with zero mean. Both methods predict the same average values (RMS and MEAN). It was shown that contribution to the random response is mostly coming from the first mode. Therefore, a good estimate can be done by considering the fundamental mode only. Temperature and distribution of temperature also significantly affect the response, particularly the MEAN response. The effect of the material distribution parameter is investigated. When the FGM plate becomes metal-rich ($n > 1$), deflection responses become greater. Influence of the length-to-thickness ratio is also investigated. It was shown that when the FGM plate is very thick, the RMS response to acoustic random pressure is very small. The effect of temperature is found only on the mean responses.

Appendix A

The elements of the stiffness matrix $[K] = [k_{ij}]$ are

$$k_{11} = A_{11}\alpha_m^2 + A_{66}\beta_n^2, \quad (\text{A-1})$$

$$k_{12} = (A_{12} + A_{66})\alpha_m\beta_n, \quad (\text{A-2})$$

$$k_{13} = 0, \quad (\text{A-3})$$

$$k_{14} = B_{11}\alpha_m^2 + nB_{66}\beta_n^2, \quad (\text{A-4})$$

$$k_{15} = (B_{12} + B_{66})\alpha_m\beta_n, \quad (\text{A-5})$$

$$k_{22} = A_{22}\beta_n^2 + A_{66}\alpha_m^2, \quad (\text{A-6})$$

$$k_{23} = 0, \quad (\text{A-7})$$

$$k_{24} = (B_{12} + B_{66})\alpha_m\beta_n, \quad (\text{A-8})$$

$$k_{25} = B_{22}\beta_n^2 + B_{66}\alpha_m^2, \quad (\text{A-9})$$

$$k_{33} = \kappa(A_{55}\alpha_m^2 + A_{44}\beta_n^2), \quad (\text{A-10})$$

$$k_{34} = \kappa A_{55}\alpha_m, \quad (\text{A-11})$$

$$k_{35} = \kappa A_{44}\beta_n, \quad (\text{A-12})$$

$$k_{44} = D_{11}\alpha_m^2 + D_{66}\beta_n^2 + \kappa A_{55}, \quad (\text{A-13})$$

$$k_{45} = (D_{12} + D_{66})\alpha_m\beta_n, \quad (\text{A-14})$$

$$k_{55} = D_{22}\beta_n^2 + D_{66}\alpha_m^2 + \kappa A_{44}. \quad (\text{A-15})$$

The elements of the mass matrix $[M] = [m_{ij}]$ are

$$m_{11} = m_{22} = m_{33} = I_0, \quad (\text{A-16})$$

$$m_{44} = m_{55} = I_2, \quad (\text{A-17})$$

$$m_{14} = m_{25} = I_1. \quad (\text{A-18})$$

Others are zero.

Appendix B

The coefficients γ_1 , γ_2 , ξ_1 and ξ_2 are defined as

$$\gamma_1(k, r, m) = \frac{a}{4\pi} \left\{ \frac{1}{k+r+m} ((-1)^{k+r+m} - 1) - \frac{1}{k+r-m} ((-1)^{k+r-m} - 1) \right. \\ \left. - \frac{1}{k-r+m} ((-1)^{k-r+m} - 1) + \frac{1}{k+r+m} ((-1)^{k+r+m} - 1) \right\}, \quad (\text{B-1})$$

$$\gamma_2(k, r, m) = \frac{a}{4\pi} \left\{ \frac{-1}{k+r+m} ((-1)^{k+r+m} - 1) + \frac{1}{k+r-m} ((-1)^{k+r-m} - 1) \right. \\ \left. - \frac{1}{k-r+m} ((-1)^{k-r+m} - 1) + \frac{1}{k-r-m} ((-1)^{k-r-m} - 1) \right\}, \quad (\text{B-2})$$

$$\xi_1(l, s, n) = \frac{b}{4\pi} \left\{ \frac{1}{l+s+n} ((-1)^{l+s+n} - 1) - \frac{1}{l+s-n} ((-1)^{l+s-n} - 1) - \frac{1}{l-s+n} ((-1)^{l-s+n} - 1) + \frac{1}{l+s+n} ((-1)^{l+s+n} - 1) \right\}, \quad (\text{B-3})$$

$$\xi_2(l, s, n) = \frac{b}{4\pi} \left\{ \frac{-1}{l+s+n} ((-1)^{l+s+n} - 1) + \frac{1}{l+s-n} ((-1)^{l+s-n} - 1) - \frac{1}{l-s+n} ((-1)^{l-s+n} - 1) + \frac{1}{l+s+n} ((-1)^{l+s+n} - 1) \right\}. \quad (\text{B-4})$$

References

- [Alijani et al. 2011] F. Alijani, F. Bakhtiari-Nejad, and M. Amabili, "Nonlinear vibrations of FGM rectangular plates in thermal environments", *Nonlinear Dyn.* **66**:3 (2011), 251–270.
- [Cederbaum et al. 1992] G. Cederbaum, I. Elishakoff, J. Aboudi, and L. Librescu, *Random vibration and reliability of composite structures*, Technomic Publishing Co., Lancaster, PA, 1992.
- [Efraim 2011] E. Efraim, "Accurate formula for determination of natural frequencies of FGM plates basing on frequencies of isotropic plates", *Proc. Eng.* **10**:0 (2011), 242–247.
- [Efraim and Eisenberger 2007] E. Efraim and M. Eisenberger, "Exact vibration analysis of variable thickness thick annular isotropic and FGM plates", *J. Sound Vib.* **299**:4–5 (2007), 720–738.
- [Elishakoff 1999] I. Elishakoff, *Probabilistic theory of structures*, 2nd ed., Dover, New York, 1999.
- [Elishakoff and Gentilini 2005] I. Elishakoff and C. Gentilini, "Three-dimensional flexure of rectangular plates made of functionally graded materials", *J. Appl. Mech. (ASME)* **72**:5 (2005), 788–791.
- [Fakhari et al. 2011] V. Fakhari, A. Ohadi, and P. Yousefian, "Nonlinear free and forced vibration behavior of functionally graded plate with piezoelectric layers in thermal environment", *Compos. Struct.* **93**:9 (2011), 2310–2321.
- [Ghannadpour et al. 2012] S. A. M. Ghannadpour, H. R. Ovesy, and M. Nassirnia, "Buckling analysis of functionally graded plates under thermal loadings using the finite strip method", *Comput. Struct.* **108–109**:0 (2012), 93–99.
- [Hasheminejad and Gheshlaghi 2012] S. M. Hasheminejad and B. Gheshlaghi, "Three-dimensional elastodynamic solution for an arbitrary thick FGM rectangular plate resting on a two parameter viscoelastic foundation", *Compos. Struct.* **94**:9 (2012), 2746–2755.
- [Hosseini and Fazelzadeh 2010] M. Hosseini and S. A. Fazelzadeh, "Aerothermoelastic post-critical and vibration analysis of temperature-dependent functionally graded panels", *J. Therm. Stresses* **33**:12 (2010), 1188–1212.
- [Hosseini-Hashemi et al. 2010] Sh. Hosseini-Hashemi, H. R. D. Taher, H. Akhavan, and M. Omid, "Free vibration of functionally graded rectangular plates using first-order shear deformation plate theory", *Appl. Math. Model.* **34**:5 (2010), 1276–1291.
- [Huang and Shen 2004] X.-L. Huang and H.-S. Shen, "Nonlinear vibration and dynamic response of functionally graded plates in thermal environments", *Int. J. Solids Struct.* **41**:9–10 (2004), 2403–2427.
- [Javaheri and Eslami 2002] R. Javaheri and M. R. Eslami, "Thermal buckling of functionally graded plates", *AIAA J.* **40**:1 (2002), 162–169.
- [Koizumi 1997] M. Koizumi, "FGM activities in Japan", *Compos. B Eng.* **28**:1–2 (1997), 1–4.
- [Lee et al. 2010] Y. Y. Lee, X. Zhao, and J. N. Reddy, "Postbuckling analysis of functionally graded plates subject to compressive and thermal loads", *Comput. Methods Appl. Mech. Eng.* **199**:25–28 (2010), 1645–1653.
- [Lin 1976] Y.-K. Lin, *Probabilistic theory of structural dynamics*, Robert E. Krieger Publishing Co., Huntington, NY, 1976.
- [Mantari and Soares 2012] J. L. Mantari and C. G. Soares, "Bending analysis of thick exponentially graded plates using a new trigonometric higher order shear deformation theory", *Compos. Struct.* **94**:6 (2012), 1991–2000.
- [Maymon 1998] G. Maymon, *Some engineering applications in random vibrations and random structures*, Progress in Astronautics and Aeronautics **178**, American Institute of Aeronautics and Astronautics, Reston, VA, 1998.

- [Mohammadi et al. 2010] M. Mohammadi, A. R. Saidi, and E. Jomehzadeh, “Levy solution for buckling analysis of functionally graded rectangular plates”, *Appl. Compos. Mater.* **17**:2 (2010), 81–93.
- [Nguyen-Xuan et al. 2012] H. Nguyen-Xuan, L. V. Tran, C. H. Thai, and T. Nguyen-Thoi, “Analysis of functionally graded plates by an efficient finite element method with node-based strain smoothing”, *Thin-Walled Struct.* **54** (2012), 1–18.
- [Prakash et al. 2012] T. Prakash, M. K. Singha, and M. Ganapathi, “A finite element study on the large amplitude flexural vibration characteristics of FGM plates under aerodynamic load”, *Int. J. Non-Linear Mech.* **47**:5 (2012), 439–447.
- [Praveen and Reddy 1998] G. N. Praveen and J. N. Reddy, “Nonlinear transient thermoelastic analysis of functionally graded ceramic-metal plates”, *Int. J. Solids Struct.* **35**:33 (1998), 4457–4476.
- [Praveen et al. 1999] G. N. Praveen, C. D. Chin, and J. N. Reddy, “Thermoelastic analysis of functionally graded ceramic-metal cylinder”, *J. Eng. Mech. (ASCE)* **125**:11 (1999), 1259–1267.
- [Reddy 2000] J. N. Reddy, “Analysis of functionally graded plates”, *Int. J. Numer. Methods Eng.* **47**:1–3 (2000), 663–684.
- [Reddy 2004] J. N. Reddy, *Mechanics of laminated composite plates and shells: theory and analysis*, 2nd ed., CRC Press, Boca Raton, FL, 2004.
- [Reddy and Chin 1998] J. N. Reddy and C. D. Chin, “Thermomechanical analysis of functionally graded cylinders and plates”, *J. Therm. Stresses* **21**:6 (1998), 593–626.
- [Shen 2009] H.-S. Shen, *Functionally graded materials: nonlinear analysis of plates and shells*, CRC Press, Boca Raton, FL, 2009.
- [Shen and Wang 2012] H.-S. Shen and Z.-X. Wang, “Assessment of Voigt and Mori–Tanaka models for vibration analysis of functionally graded plates”, *Compos. Struct.* **94**:7 (2012), 2197–2208.
- [Shinozuka and Jan 1972] M. Shinozuka and C.-M. Jan, “Digital simulation of random processes and its applications”, *J. Sound Vib.* **25**:1 (1972), 111–128.
- [Thai and Choi 2012] H.-T. Thai and D.-H. Choi, “A refined shear deformation theory for free vibration of functionally graded plates on elastic foundation”, *Compos. B Eng.* **43**:5 (2012), 2335–2347.
- [Yang and Gao 2013] Q. Yang and C.-F. Gao, “Dynamic stress analysis of a functionally graded material plate with a circular hole”, *Meccanica (Milano)* **48**:1 (2013), 91–101.
- [Yang and Shen 2002] J. Yang and H.-S. Shen, “Vibration characteristics and transient response of shear-deformable functionally graded plates in thermal environments”, *J. Sound Vib.* **255**:3 (2002), 579–602.
- [Yang and Shen 2003] J. Yang and H.-S. Shen, “Nonlinear bending analysis of shear deformable functionally graded plates subjected to thermo-mechanical loads under various boundary conditions”, *Compos. B Eng.* **34**:2 (2003), 103–115.
- [Zhang et al. 2012] W. Zhang, Y. Hao, X. Guo, and L. Chen, “Complicated nonlinear responses of a simply supported FGM rectangular plate under combined parametric and external excitations”, *Meccanica (Milano)* **47**:4 (2012), 985–1014.
- [Zhao et al. 2009] X. Zhao, Y. Y. Lee, and K. M. Liew, “Mechanical and thermal buckling analysis of functionally graded plates”, *Compos. Struct.* **90**:2 (2009), 161–171.

Received 25 Nov 2013. Revised 19 Mar 2014. Accepted 25 Mar 2014.

VEDAT DOGAN: doganve@itu.edu.tr

Faculty of Aeronautical and Astronautical Engineering, Istanbul Technical University, Maslak, 34469 Istanbul, Turkey

MECHANICAL BEHAVIOR OF BRICK MASONRY PANELS UNDER UNIAXIAL COMPRESSION

HACER BILIR ÖZHAN AND ISMAIL HAKKI CAGATAY

Structural design in masonry requires clear understanding of the behavior of the composite unit-mortar material under various loading conditions. The mechanical characteristics of brick masonry are influenced by the individual properties of the bricks and the mortar. The results of an experimental study focused on the properties of brick masonry using different combinations of bricks and mortars are presented in this paper. The strength and the elastic modulus of brick masonry under uniform concentric vertical loads have been investigated for strong mortar (M:1:3 cement-sand) and weak mortar (M:1:6 cement-sand) arrangements. The failure mechanisms of the infill walls with horizontal coring bricks have also been examined.

1. Introduction

Masonry walls are widely used in many types of buildings due to their low cost and good sound and heat insulation properties, as well as the availability of local material and skilled labor. Mathematical modeling of structures with masonry walls requires understanding of the material properties and the interaction of the masonry and its constituents. Masonry is typically nonelastic, nonhomogeneous and anisotropic material and is composed of two materials, stiffer bricks and relatively softer mortar. These two have quite different mechanical properties. However, under lateral loads, masonry does not behave elastically even in the range of small deformations. Masonry is very weak in tension since the bond between the brick and the mortar is frail. Therefore, the main expectation from masonry is its resistance against vertical (compressive) loading.

During compression of masonry panels constructed with stronger and stiffer bricks, mortar of the bed joint has a tendency to expand laterally more than the bricks because of lesser stiffness [Atkinson and Noland 1983]. However, mortar is confined laterally at the brick-mortar interface by the bricks because of the bond between them. Therefore, shear stresses at the brick-mortar interface result in an internal state of stress which consists of triaxial compression in mortar and bilateral tension coupled with axial compression in bricks [McNary and Abrams 1985]. This state of stress initiates vertical splitting cracks in bricks that lead to the failure of the panels [Drysdale et al. 1994].

Grenley [1969] studied the effect of various mortars on the flexural and compressive strength of masonry and on the tensile bond strength of crossed brick assembly. His test results showed that, in general, flexural and tensile bond strengths increased with the strength of brick and the strength of mortar. The masonry compressive strength also showed a similar trend. The correlation between bond adhesion and compressive strength of masonry seems to suggest the importance of brick-mortar bond on masonry compressive strength. However, the increase in bond strength is also accompanied by an

Keywords: brick, brick masonry, mortar, masonry compressive strength, modulus of elasticity.

increase in mortar compressive strength. Hence, the relative influence of the mortar-brick bond and mortar compressive strength on the masonry compressive strength is not clear. The compressive strength of masonry depends on several factors and the thickness of the mortar bed joint is one of the significant factors influencing masonry strength. Houston and Grimm [1972] showed that the compressive strength of brick masonry decreases with increase in mortar bed joint thickness for constant height of the brick. Venkatarama Reddy et al. [2009] investigated the influence of bed joint thickness and elastic properties of the soil-cement blocks, and the mortar on the strength and behavior of soil-cement block masonry prisms. The major conclusions of their work are:

- (1) Masonry compressive strength is sensitive to the ratio of modulus of block to that of the mortar (E_b/E_m) and masonry compressive strength decreases as the mortar joint thickness is increased for the case where the ratio of block to mortar modulus is more than 1.
- (2) The lateral tensile stresses developed in the masonry unit are sensitive to the E_b/E_m ratio and the Poisson's ratio of mortar and the masonry unit.
- (3) Lateral stresses developed in the masonry unit are more sensitive to the Poisson's ratio of the mortar than the Poisson's ratio of the masonry unit.

Since masonry is an assemblage of bricks and mortar, it is generally believed that the strength and stiffness of masonry would lie somewhere between that of bricks and mortar. When one component of masonry, i.e., either bricks or mortar, is substantially weaker and softer, the other is stronger as suggested by Dayaratnam [1987] and Sarangapani et al. [2002]. Based on an experimental study by Sarangapani et al. [2002], the soft bricks' modulus of elasticity (500 MPa) was responsible for the development of triaxial compression in bricks and axial compression with lateral tension in mortar points of masonry prism. Sarangapani et al. [2005] conducted a series of tests on masonry prisms constructed with very soft bricks (modulus of elasticity \sim 500 MPa) and a combination of different mortar grades. It was observed that for the soft brick-stiff mortar masonry, the compressive strength of masonry increases with the increase in bond strength. Using experimental data, Houston and Grimm [1972], Paulay and Priestley [1992], and Binda et al. [1988] suggested several analytical relations for estimation of strength and deformation characteristics of masonry, which depend upon the compressive and tensile strengths of bricks and mortar along with several other factors.

Several experimental and theoretical studies were also carried out on axially loaded masonry walls. Negro and Verzeletti [1996] conducted a series of tests on 1 to 1 scale reinforced concrete buildings with and without infill walls. They determined an increase of 1.5 times more load carrying capacity of infill walls over walls without any filling. Alshebani and Sinha [1999] tested brick wall panels under periodic axial loading. Different types of loadings vertical and parallel to the joints were applied until failure occurred. They concluded that the joint separation as well as the fractures in the bricks and in the joints was due to the applied vertical loading. Gumaste et al. [2007] investigated the mechanical properties such as the strength and the elasticity modulus of the walls having different brick-mortar combinations under axial loading.

The compressive strength and the elastic modulus of brick and mortar are the major factors, which influence the properties of brick masonry wall. Elasticity modulus of masonry wall, which affects the wall rigidity, is the dominant factor influencing the behavior of masonry wall on the frame systems. The behavior of brick masonry also depends on the other factors such as interfacial bond strength between

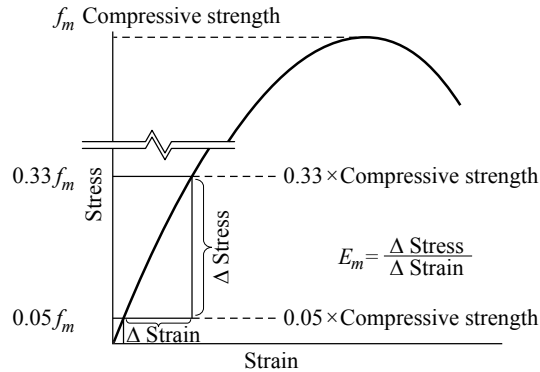


Figure 1. Stress-strain relationship of the infill walls based on the prism test.

brick and mortar, moisture in the brick at the time of laying, thickness of mortar joints, arrangement of bricks, workmanship. Modulus of elasticity changes with the direction (horizontal, vertical and diagonal) because of non-homogeneity of the wall. Elasticity modulus of masonry wall is also determined by the compressive strength of the material, the material height, the compressive strength of the mortar and the layer of the mortar line. The computation of modulus of elasticity for infill walls is given by

$$E_m = \frac{\sigma_{0.33} - \sigma_{0.05}}{\epsilon_{0.33} - \epsilon_{0.05}}, \quad (1)$$

where $\epsilon_{0.33}$ is the strain corresponding to the stress ($\sigma_{0.33}$), which is the compressive prism strength of 33% of masonry, and $\epsilon_{0.05}$ is the strain corresponding to the stress ($\sigma_{0.05}$), which is the compressive prism strength of 5% of masonry. A representation of this equation, following the American Concrete Institute [ACI 1999], is shown in Figure 1.

The elasticity modulus estimated in this study was compared and verified with the moduli available in the literature as presented in Table 1.

The aim of this study is to investigate the uniaxial monotonic compressive stress-strain behavior and other characteristics of bricks, (horizontal coring bricks), two types of mortar and unreinforced masonry panels (brick infill panel). In the comprehensive experimental study, tests were performed on 6 types of mortar cube specimens (with two different strength values as weak and strong), two different grades and 6 specimens of masonry panels (combination of one brick and two mortar types). Based on the experimental results and the observations, stress strain relationship curves were developed for mortars,

Source	Equation
[FEMA 1998]	$E = 550 f_m$
[Paulay and Priestley 1992]	$E = 700 f_m$
Canadian Standards Association [CSA 2004]	$E = 850 f_m$
American Concrete Institute [ACI 1999]	Equation (1), Figure 1
Turkish Earthquake Code [TEC 2007]	Average 1000 MPa

Table 1. Elasticity moduli from the literature.

horizontal coring bricks panels. Finally, as explained in the following section, elasticity moduli obtained from the experimental results were compared to the values reported in the literature.

2. Experimental program and discussions

In the present experimental study, several tests were carried out in order to evaluate the uniaxial compressive stress-strain relationship of masonry panels constructed with different combinations of mortar grades. Different types of mortar and bricks were utilized in the study. Masonry panels were subjected to monotonically incremental strain controlled axial loading. The load was applied vertically by a 550 kN load and ± 10 mm displacement capacity hydraulic actuator in Hi-Tech Magnus loading frame (see Figure 2). Also, mortar cubes were tested in a 2,500 kN ELE Press testing machine under stress controlled loading. The specimens were built on 25 mm thick steel plates and cured under damp condition for 28 days and covered with wet jute sacks to maintain damp condition. The experimental study included total of 6 specimens of masonry panels with two different grades mortar.

2.1. Mortar testing. Masonry panels were tested with two different grades of mortar (cement/sand by volume) namely M:1:6 cement-sand mortar (weak), M:1:3 cement-sand mortar (strong). Since the mechanical properties of the mortar does influence the infill panel strength, mortar cubes of 150 mm size were tested after 28 days of casting to obtain their compressive stress-strain relationship. Determinations of compressive strength of mortar cubes, as suggested by Turkish standards [TS 24 1985], are given in Table 2.

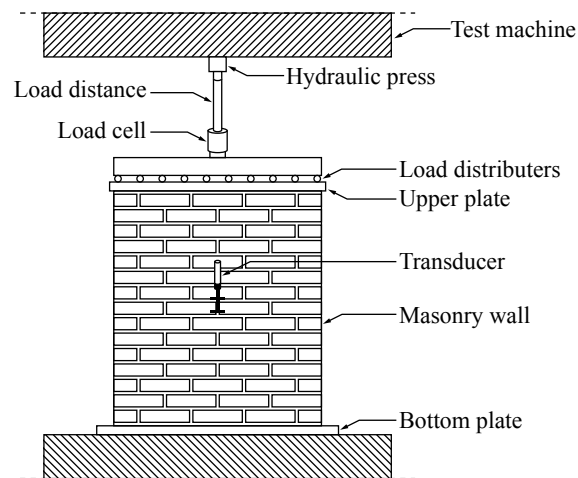


Figure 2. Test set-up and instrumentation.

mortar	compressive strength (MPa)	modulus of elasticity (MPa)	specimen dimensions (mm)
M:1:3	22.53	112.64	150 × 150 × 150
M:1:6	8.89	79.95	150 × 150 × 150

Table 2. Mechanical properties of mortars.



Figure 3. Appearance cracking of weak mortar cubes after loading (Failure modes of mortar cubes).



Figure 4. Appearance of failure modes of strong mortar cubes after the loading.

The appearances of fracturing of mortar cubes, after loading, for weak and strong samples are depicted in Figures 3 and 4, respectively.

The test results for the stress strain relationship are plotted in Figure 5. The dots in Figure 5 represent the test results. The best fitting curves obtained from statistical analyses are represented by the solid

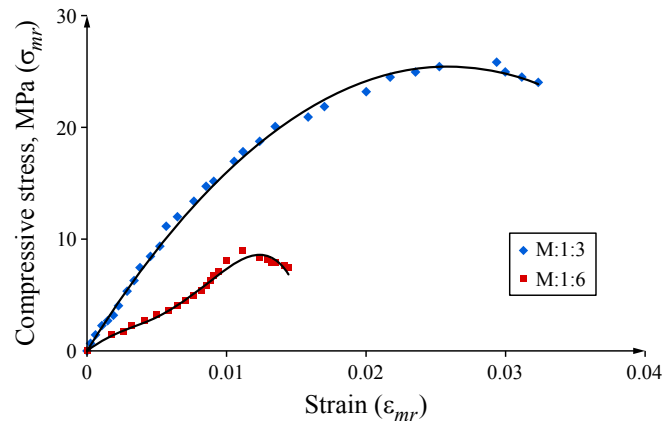


Figure 5. Comparison of compressive stress-strain curves for strong mortar cubes with weak mortar cubes.

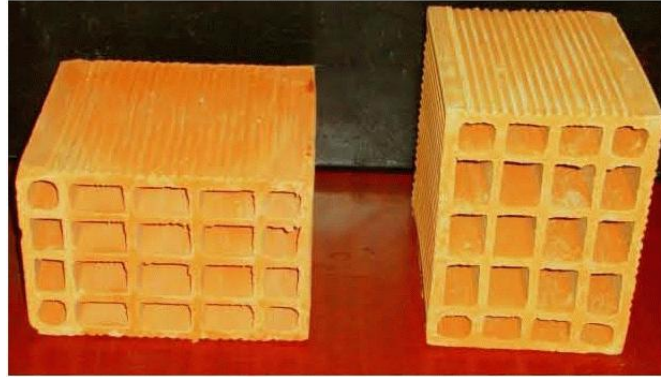


Figure 6. Horizontal coring brick.

lines. Table 2 lists the mechanical properties for each type as determined.

2.2. Infill wall testing. Horizontal coring bricks shown in Figure 6 were used in constructing masonry panels. Their average dimension (length \times width \times height) is $190 \times 190 \times 135$ mm. Besides, bricks' average compressive strength was determined to be 5.2 MPa, through uniaxial compressive strength tests. Horizontal coring brick is used in experimental study because it is one of the widely used types in building masonry panels in the region.

The test set-up employed in the study is given in Figure 2. The load cell and the transducers were calibrated before they were used in the tests. The digital readings of uniaxial monotonic compressive load and corresponding vertical displacements were recorded through electronic data acquisition system during testing of each specimen.

The main focus of this study was to investigate the behavior of the brick infill wall, under vertical concentric uniform load, as well as to estimate the modulus of elasticity. The results are graphically illustrated in Figures 7 and 8.

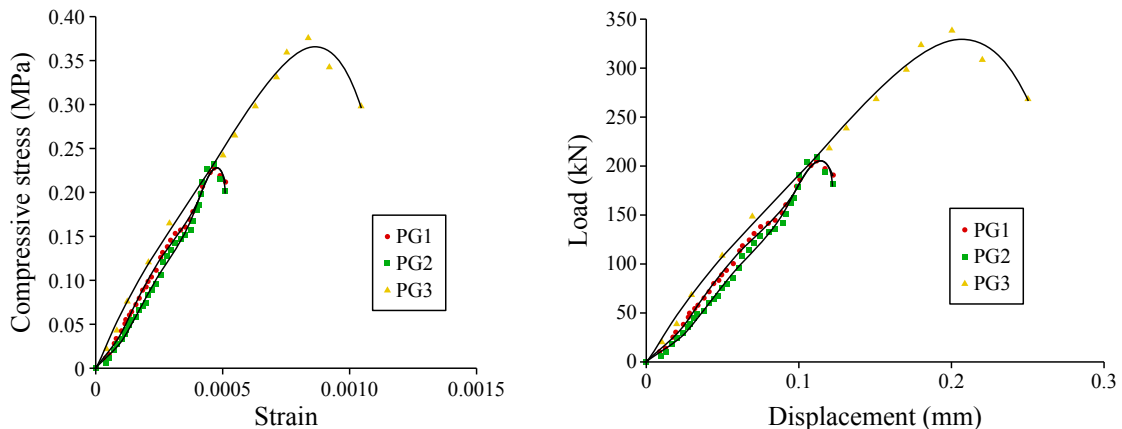


Figure 7. Compressive stress-strain curves (left) and load displacement curve (right) for brick masonry panel with M:1:3 (strong) mortar.

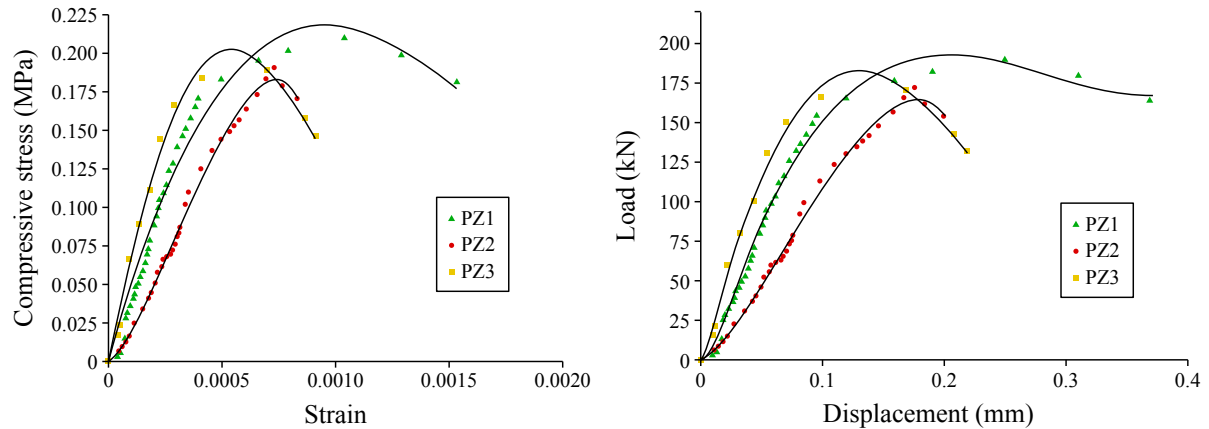


Figure 8. Compressive stress-strain curves (left) and load displacement curve (right) for brick masonry panel with M:1:6 (weak) mortar.

The results show that there are no substantial differences between PG1, PG2 and PG3 panels. It was observed that while PG1 and PG2 samples endured similar loading capacities, PG3 attained higher loading levels and failed after corresponding greater displacement values. The differences in cracking styles among these samples which were made up of similar strong mortars were believed to be because of the fracturing mechanisms involved (Figure 9). The M:1:3 cement-sand mortar panels generally showed better strength which was greater than the M:1:6 cement-sand mortar panels. When the mortar became considerably stronger as in the case of M:1:3, the improvement in strength of brick masonry panel was clearly achieved. The strength of masonry values ranged from 0.18 MPa to 0.38 MPa. Once again the best fitting curves obtained from statistical analyses are plotted in Figures 7 and 8.

Various failure patterns were observed in the test conducted on brick masonry walls. The first sample was a $1\text{ m} \times 1\text{ m}$ panel (PG1) made up of horizontal coring bricks. The mortar rate employed was 1:3. As a result, in parallel with the load applied, symmetrical cracks on the center and on the corners of the panel were observed. These cracks, for all the panels tested, are shown in Figure 9. In the case of masonry walls, mortar in the vertical joint can cause splitting failure in the brick below, since the stress in the mortar is much higher because of its greater stiffness, the masonry wall is likely to split vertically in the middle of the thickness. The cracks initiated at the loading level of approximately 10 t on the PG1, PG2 and PG3 infill wall panels made up of strong mortar. The ultimate fracturing occurred around 20 t to 30 t. Similarly initial fracturing in PZ1, PZ2 and PZ3 infill wall panels began in the mid sections in the form of tiny cracks at 6 to 6.5 tons loading levels. As a result of this mechanism, which is thought to be due to the lower mortar strengths in comparison to the other panels, bending cracks on the face of the panels (around the mid sections) as shown in Figure 9 were observed. Test results showed that, in general, flexural and tensile bond strengths increased with the strength of brick and the strength of mortar. That's why, the masonry compressive strength also showed a similar trend.

It was observed that the flexural cracks started to appear in a direction perpendicular to the infill wall panel axis at a loading level of about 50% of the maximum load on the tensile side of the specimens. The existing cracks propagated and new cracks were observed along the tensile side of the panel specimens with the increase of loading level. Beyond the maximum load, major cracks appeared on the tensile side

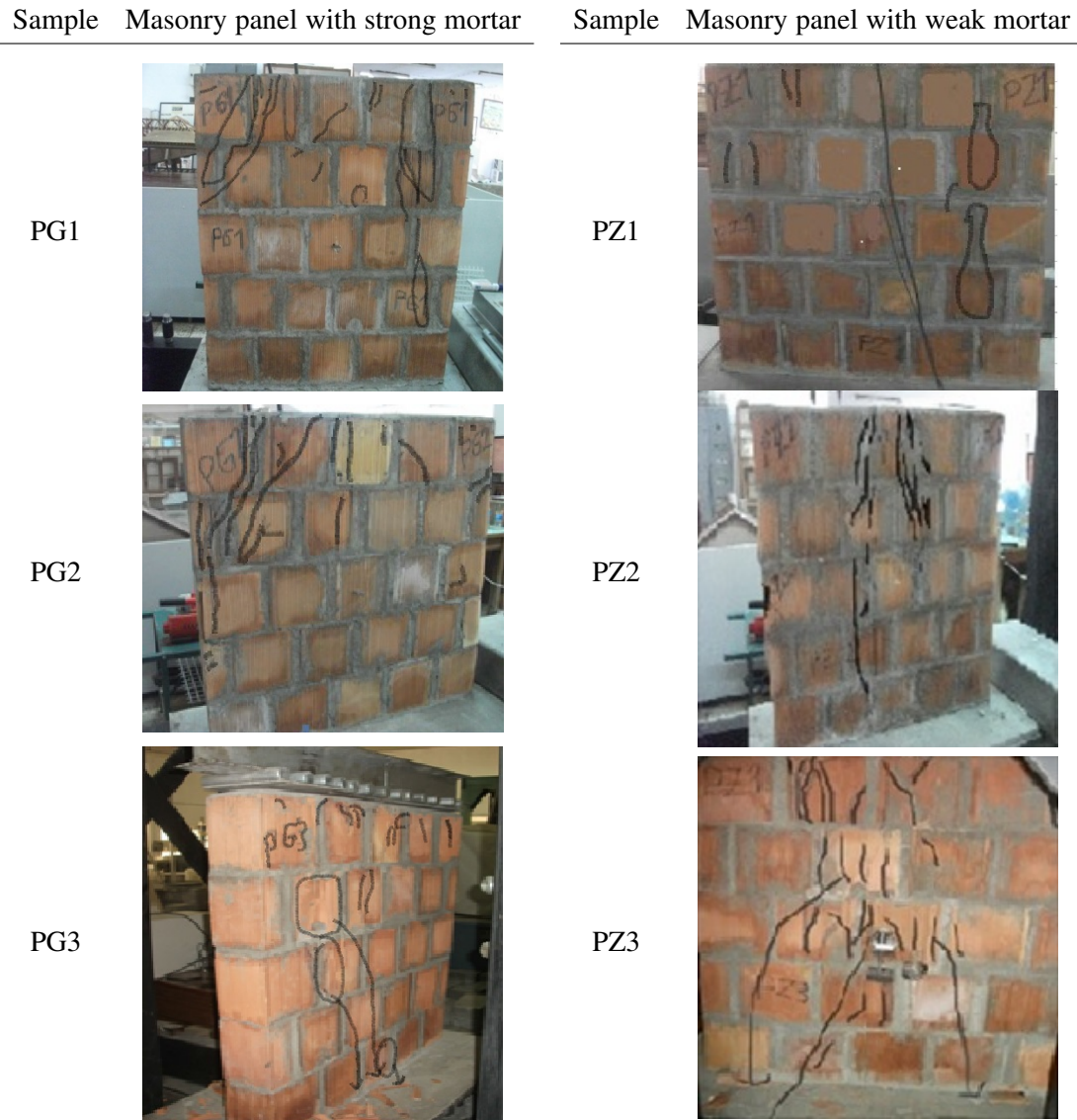


Figure 9. Cracks on the brick masonry panel with M:1.3 (strong) and M:1:6 (weak) mortars after loading.

and the masonry infill wall crushed on the compression side at or close to mid-height of the masonry infill wall panel. Also, significant drop was measured in the loading resistance. Failure occurred in the most heavily compressed region for all the masonry infill wall panels. Cracking mechanisms depicted in Figure 9 are not quite inconsistent. They are assumed to be due to varying loading durations, which aimed to better observe the cracking behaviors, and due to the combined effects of several other factors such as non-homogeneity of the panels.

Table 3 tabulates the values of elastic moduli of all panels with M:1:6 and M:1:3 mortars. From the comparison of the values obtained for panels using horizontal coring bricks, it was observed that the

Methods	Panels: PG1	PG2	PG3	PZ1	PZ2	PZ3
Experiment Result	490	499.52	453.33	202.05	190.76	268.24
TEC	1000	1000	1000	1000	1000	1000
Fema	126	128.21	207.78	115.77	115.77	104
Paulay and Priestly	160	163.18	264.44	147.33	133.53	132
ACI	490	499.52	453.33	202.05	190.76	268.24
CSA	194	198.14	321.11	179	162.14	161

Table 3. Modulus of elasticity, E (Mpa) results of all panels. For the abbreviations TEC, ACI and CSA, see Table 1.

elastic moduli of PG1, PG2 and PG3 panels (with M:1:3) were in a very close range. The moduli of elasticity of PZ1, PZ2 and PZ3 panels are much lower than the others, PGs.

In order to see the effect of mortar type on the infill wall strength, three wall panels, having the same dimensions and properties, for each type were prepared and tested. The tested panels did have compatible results within each category. Strong infill panels, in parallel to the increase in mortar strength, attained higher loading and deformation values. Whereas the weaker ones, with decrease in mortar strength, could achieve lower loading and deformation values. Although the mortar strength is not the single parameter governing the panel strength, its influence cannot be ignored. The results obtained showed perfect correlation with similar studies reported in the literature by Grenley [1969], Dayaratnam [1987], Sarangapani et al. [2002], Gumaste et al. [2007] and Venkatarama Reddy et al. [2009].

The moduli of elasticity obtained, as shown in Table 3, were exactly same as the value proposed by the American Concrete Institute, whereas the other standard values from the literature were below the experimental results obtained.

3. Conclusions

In this research, tests were performed on 6 types of mortar cube specimens (with two different strength values as weak and strong), two different grades mortar and 6 specimens of masonry panels (combination of one brick and two mortar types). Based on the experimental results, modulus of elasticity of masonry was found to vary between 190 MPa and 500 MPa. This variation, as expected, clearly shows that the mechanical behavior of masonry infill panels depends on its constituents, mainly mortar type. Besides, the compressive strength of masonry was observed to be increasing with the compressive strength of the bricks and the mortar. Specimens with 1:6 cement-sand mortar failed due to the loss of the bond between the brick and the mortar. The results show that there are no substantial differences between PG1, PG2 and PG3 panels. The moduli of elasticity of PZ1, PZ2 and PZ3 panels are much lower than the others, PGs. The M:1:3 cement-sand mortar panels generally showed better strength which was greater than the M:1:6 cement-sand mortar panels. Samples showed failure due to splitting of the bricks. The first crack formation occurred to PGs when the loading level reached 10 tons during the tests. Further experimental verification may be required for the extension of these results for different kind of bricks and mortar of different grades. It was observed that the flexural cracks started to appear in a direction perpendicular to the infill wall panel axis at a loading level of about 50% of the maximum load on the tensile side of the

specimens. The existing cracks propagated and new cracks were observed along the tensile side of the panel specimens with the increase of loading level. Beyond the maximum load, major cracks appeared on the tensile side and the masonry infill wall crushed on the compression side at or close to mid-height of the masonry infill wall panel. Stress-strain curves of masonry constructed with bricks and mortar of comparable strengths and stiffness was observed to lie below the stress-strain curves of both bricks and mortar, which is not in accordance with the generally accepted compressive behaviour of masonry. Therefore, more experimental study is required with different combinations of brick types and mortar grades to develop a generalized model for compressive behavior and elastic moduli of masonry.

4. Notation

The following symbols are used in this paper:

PG1	Infill wall panels 1 made up of strong mortar (1:3)
PG2	Infill wall panels 2 made up of strong mortar (1:3)
PG3	Infill wall panels 3 made up of strong mortar (1:3)
PZ1	Infill wall panels 1 made up of weak mortar (1:6)
PZ2	Infill wall panels 2 made up of weak mortar (1:6)
PZ3	Infill wall panels 3 made up of weak mortar (1:6)
σ	Compressive stress
ϵ	Strain
σ_{mr}	Compressive stress for strong mortar cubes
ϵ_{mr}	The strain for strong mortar cubes
f_m	Compressive prism strength of masonry
E_m	modulus of elasticity of masonry in compression

5. Acknowledgements

Support was provided by Çukurova University project MMF2007D11. We also wish to thank the anonymous reviewers who contributed to the improvement of this manuscript.

References

- [ACI 1999] "Building code requirements for masonry structures", Report ACI 530-95/ASCE 5-95, ASCE, Washington, DC, 1999.
- [Alshebani and Sinha 1999] M. M. Alshebani and S. N. Sinha, "Stress-strain characteristics of brick masonry under uniaxial cyclic loading", *J. Struct. Eng. (ASCE)* **125**:6 (1999), 600–604.
- [Atkinson and Noland 1983] R. H. Atkinson and J. L. Noland, "A proposed failure theory for brick masonry in compression", pp. 5.1–5.5 in *Proceedings of the 3rd Canadian Masonry Symposium* (Edmonton, Alberta, 1983), edited by J. Longworth and J. Warwaruk, University of Alberta, Dept. of Civil Engineering, Edmonton, Alberta, 1983.
- [Binda et al. 1988] L. Binda, A. Fontana, and G. Frigerio, "Mechanical behaviour of brick masonries derived from unit and mortar characteristics", pp. 205–216 in *Brick and block masonry* (Dublin, 1988), vol. 1, edited by J. W. de Courcy, Elsevier, London, 1988.
- [CSA 2004] "Design of masonry structures", CSA Standard S304, Canadian Standards Association, Toronto, ON, 2004, Available at <http://shop.csa.ca/en/canada/structures/s3041-04-r2010/inv/27006002004>.
- [Dayaratnam 1987] P. Dayaratnam, *Brick and reinforced brick structures*, Oxford and IBH, New Delhi, 1987.

- [Drysdale et al. 1994] R. Drysdale, A. Hamid, and L. Baker, *Masonry structures: behavior and design*, Prentice-Hall, 1994.
- [FEMA 1998] “Evaluation of earthquake damaged concrete and masonry wall buildings: basic procedures manual”, Report 306, Federal Emergency Management Agency, Washington, DC, 1998, Available at <http://www.fema.gov/media-library/assets/documents/3068?id=1651>.
- [Grenley 1969] D. G. Grenley, “Study of the effect of certain modified mortars on compressive and flexural strength of masonry”, pp. 28–33 in *Designing, engineering, and constructing with masonry products: proceedings of the International Conference on Masonry Structural Systems* (Austin, TX, 1967), edited by F. B. Johnson, Gulf, Houston, TX, 1969.
- [Gumaste et al. 2007] K. S. Gumaste, K. S. Nanjunda Rao, B. V. Venkatarama Reddy, and K. S. Jagadish, “Strength and elasticity of brick masonry prisms and wallettes under compression”, *Mater. Struct.* **40**:2 (2007), 241–253.
- [Houston and Grimm 1972] J. Y. Houston and C. T. Grimm, “Effect of brick height on masonry compressive strength”, *J. Mater.* **7** (1972), 388–397.
- [McNary and Abrams 1985] W. S. McNary and D. P. Abrams, “Mechanics of masonry in compression”, *J. Struct. Eng. (ASCE)* **111**:4 (1985), 857–870.
- [Negro and Verzeletti 1996] P. Negro and G. Verzeletti, “Effect of infills on the global behaviour of R/C frames: energy considerations from pseudodynamic tests”, *Earthq. Eng. Struct. Dyn.* **25**:8 (1996), 753–773.
- [Paulay and Priestley 1992] T. Paulay and M. J. N. Priestley, *Seismic design of reinforced concrete and masonry buildings*, Wiley, New York, 1992.
- [Sarangapani et al. 2002] G. Sarangapani, B. V. Venkatarama Reddy, and K. S. Jagadish, “Structural characteristics of bricks, mortar and masonry”, *J. Struct. Eng. (India)* **29**:2 (2002), 101–107.
- [Sarangapani et al. 2005] G. Sarangapani, B. V. Venkatarama Reddy, and K. S. Jagadish, “Brick-mortar bond and masonry compressive strength”, *J. Mater. Civ. Eng. (ASCE)* **17**:2 (2005), 229–237.
- [TEC 2007] “Specifications for buildings to be built in seismic zones”, Official Gazette No. 26454, Ministry of Public Works and Settlement, Government of Republic of Turkey, March 6, 2007, Available at <http://www.koeri.boun.edu.tr/depremmuh/eski/DBYBHY2007-English-Chapters1,2.pdf>.
- [TS 24 1985] TS 24, Turkish standard for physical and mechanical testing method of cement, TSE, 1985.
- [Venkatarama Reddy et al. 2009] B. V. Venkatarama Reddy, L. Richardson, and K. S. Nanjunda Rao, “Influence of joint thickness and mortar-block elastic properties on the strength and stresses developed in soil-cement block masonry”, *J. Mater. Civ. Eng. (ASCE)* **21**:10 (2009), 535–542.

Received 2 Dec 2013. Revised 30 Jan 2014. Accepted 25 Mar 2014.

HACER BILIR ÖZHAN: hacer.ozhan@bou.edu.tr

Assistant Professor, Department of Civil Engineering, Bursa Orhangazi University, 16350 Bursa, Turkey

ISMAIL HAKKI CAGATAY: hcagatay@cu.edu.tr

Professor, Department of Civil Engineering, Çukurova University, 01330 Adana, Turkey

COLLAPSE MECHANISMS OF METALLIC SANDWICH STRUCTURES WITH ALUMINUM FOAM-FILLED CORRUGATED CORES

BIN HAN, LEI L. YAN, BO YU, QIAN C. ZHANG, CHANG Q. CHEN AND TIAN J. LU

The physical mechanisms underlying the beneficial effect of filling aluminum foams into the interstices of corrugated plates made of stainless steel were explored with finite element (FE) simulations. Relative to unfilled corrugated plates of equal mass, this effect was assessed on the basis of elevated peak stress and enhanced energy absorption under quasistatic out-of-plane compression. Upon validating the FE predictions against existing measurements, the influence of key geometrical and material parameters on the compressive response of foam-filled corrugated plates was investigated. Different from the traditional buckling modes of empty corrugations, four new buckling modes were identified for foam-filled corrugations. Based upon these deformation modes of post-buckling, collapse mechanism maps were constructed. Due to the additional resistance provided by foam filling against buckling of the corrugated plate and the strengthening of foam insertions due to complex stressing, both the load bearing capacity and energy absorption of foam-filled sandwiches were greatly enhanced.

1. Introduction

Although not the best structural material, metallic and polymer foams with stochastic cellular topologies have been widely exploited for energy absorption, heat dissipation, vibration damping and other functional applications. In recent years, there is also a growing interest in exploiting the stochastic foams as a filling material to enhance simultaneously the load-bearing and energy absorption capabilities of traditional lightweight structures, such as hollow tubes and sandwich constructions having flow-through, periodic lattice truss cores [Vaziri et al. 2006; Mamalis et al. 2008; Kazemahvazi and Zenkert 2009; Kazemahvazi et al. 2009; Nia and Sadeghi 2010; Ostos et al. 2012; Zhang et al. 2013; Yan et al. 2013]. From the viewpoint of energy absorption, in the field of civil engineering (structural mechanics in particular), structures that deform plastically under static or dynamic compression have been characterized into two main types [Calladine and English 1984; Tam and Calladine 1991]. A type I structure (radially loaded arches and rings, say) exhibits a plateau-like stress versus strain curve and is able to absorb large amount of energy at a constant stress level, thus a preferable candidate for energy absorption. In contrast, the stress of a type II structure (axially loaded columns, for example) drops sharply after the peak value is reached, thus less attractive for energy absorption applications because large forces are transferred while limited amount of energy is absorbed. Under quasistatic out-of-plane compression, it has been established that inserting close-celled aluminum foams into the interstices of a metallic corrugate-cored sandwich panel increases significantly both its peak stress and energy absorption [Yan et al. 2013]. Further, with foam insertion, the initially type II energy absorbing structure (i.e., empty corrugated cores)

Keywords: foam-filled corrugated core, finite element method, buckling, collapse mechanism.

was transformed into a type I energy absorbing structure, enabling high crushing strength and high energy absorption per unit mass.

1.1. Previous research on foam-filled sandwich constructions. Before discussing the effect of aluminum foam filling upon the mechanical properties of corrugated plates, consider first the case of combining foam with various types of pin-reinforcement for sandwich constructions. The effect of titanium and carbon fiber pin-reinforcements upon the out-of-plane compressive strength of polymethacrylimide foam-cored sandwich panels was measured both quasistatically and dynamically [Cartié and Fleck 2003]. It was found that the compressive strength was governed by elastic buckling of the pins, with the foam core behaving as an elastic Winkler foundation in supporting the pins. As a result, the pin-reinforced core had a strength and energy absorption capacity in excess of the combined individual contributions from the foam and unsupported pins. Subsequently, Marasco et al. [2006] measured the out-of-plane properties of two different Z-pinned sandwich panels, both filled with Rohacell foam, under quasistatic tension, shear, or compression. Compared with equivalent honeycomb cores, the foam supported Z-pin cores exhibited higher specific stiffness but lower strength. Similar experimental measurements for Z-pinned composite sandwich panels were carried out by Nanayakkara et al. [2011]. The collapse of X-core sandwich panels consisting of a pin reinforced polymer foam core and carbon fiber face sheets were assessed experimentally under three-point bending [Rice et al. 2006]. Compared with other sandwich cores such as aluminum honeycombs and aluminum foams, it was found that such an X-core led to higher bending stiffness and strength. Liu et al. [2008] developed a comprehensive analytical model to characterize the collapse behavior of pin-reinforced foam sandwich beams under 3-point bending and verified the model predictions against finite element (FE) simulation results. It was demonstrated that sandwich beams with pin-reinforced polymer foam cores were structurally more efficient than foam-cored sandwich beams without pin reinforcements.

Consider next the influence of foam filling upon the mechanical performance of sandwich panels having other core types such as corrugated plates, honeycombs, egg boxes, and 3D lattice trusses. The performance of a hierarchical all-composite corrugated sandwich core filled with PMI-foam (Rohacell) was investigated analytically and experimentally [Kazemahvazi and Zenkert 2009; Kazemahvazi et al. 2009]. Dependent upon the geometrical dimensions and material properties of the sandwich, a multitude of failure modes were identified. It was found that the weight specific strength of a well-designed hierarchical structure could be 7 times higher than that of its monolithic counterpart. The enhancement in strength was attributed mainly to the increased buckling resistance of the hierarchical core members due to foam support, especially for core configurations with low overall density. As the core density was increased, the monolithic core members became stockier and more resistant to buckling and thus the benefits of the hierarchical structure were gradually lost.

Nia and Sadeghi [2010] investigated experimentally the effects of foam filling on the compressive response of hexagonal cell aluminum honeycombs under axial compression and found that the mean crushing strength and energy absorption were enhanced up to 300%. Subsequently, Mahmoudabadi and Sadighi [2011] developed a theoretical model to determine the mean crushing strength of foam-filled honeycombs under both quasistatic and dynamic compression, whilst Burlayenko and Sadowski [2010] predicted the effective elastic properties of such foam-filled honeycombs using FE analysis.

Based upon FE simulations, Vaziri et al. [2006] assessed the mechanical properties of metallic sandwich plates having corrugated cores and square honeycomb cores, both filled with polymer foam (Divinycell). Whilst the foam-filled cores showed greater out-of-plane shear strength, they were not comparable to the equivalent unfilled cores in terms of compression strength; further, under quasistatic punch loads and impulsive loads, the foam-filled cores only exhibited comparable structural performance in resisting deformation to the unfilled ones with equal mass. Through hybridization of glass and carbon fibers as well as foam filling, Zhang et al. [2013] attempted to improve the bending strength and energy absorption of corrugated sandwich composite structures. Due to the better support of the web by the filling foam, the peak load was increased, delaying debonding of the core and face sheets, and thus core failure. However, the improvement in crashworthiness was not significant as the foam used was relatively weak (low density).

Yoo et al. [2010] tested foam-filled composite egg-box sandwich panels under compression and found that this construction showed good energy absorption capacity with stable collapse response. Further, the filling with low density foams led to the best energy absorption performance of the sandwich. An integrated orthogrid stiffened syntactic foam core was investigated with both low velocity impact tests and compression after impact (CAI) tests [Li and Muthyala 2008]. The integrated core exhibited enhanced impact energy absorption and positive composite action with higher CAI strength.

Recently, with the goal of combining the desirable attributes of stochastic foams and lattice truss structures, Ostos et al. [2012] inserted polyurethane foams with submillimeter pores into the centimeter-scale interstices of low-density polymer lattices and assessed the concept in terms of quasistatic compressive response. It was demonstrated that the filling of even a weak foam could double the crushing strength of the lattice. Based upon X-ray computed tomography and FE analysis, the elevation was attributed to the lateral support of the strut members against buckling provided by the surrounding foam.

Existing studies regarding the effects of foam filling upon the mechanical performance of sandwich constructions focused mainly on polymer foams. Further, the unfilled sandwiches considered were constructed mainly with nonmetallic materials such as polymer or fiber-reinforced composites. One notable exception was the work of Yan et al. [2013] who inserted close-celled aluminum foams into the interstices of corrugated sandwich panels made of stainless steel and assessed the performance of the sandwich under quasistatic compression. It was demonstrated that, relative to empty corrugated sandwiches, foam filling could increase significantly not only the crushing strength but also the specific energy absorption. It was further shown that the core web was considerably stabilized by the filling foam against lateral deflection. In particular, the elasto-plastic buckling wavelength was significantly reduced and the transition from axial deformation to bending of the core web was much delayed, both contributing to enhanced strength and energy adsorption. As a result, the post-yielding response of the foam-filled sandwich was altered in such a way that crushing occurred at a nearly constant stress, consistent with the finding of Ostos et al. [2012] for polymer lattice structures filled with polymer foams.

1.2. Scope of present study. Built upon the mainly experimental work of Yan et al. [2013], the present investigation aimed to model numerically the quasistatic out-of-plane compressive response of metallic corrugated sandwich panels filled with close-celled aluminum foams, and then use the numerical models to explore the underlying physical mechanisms and construct the collapse mechanism maps. After specifying the problem in Section 2, FE models for both empty and foam-filled corrugated plates were

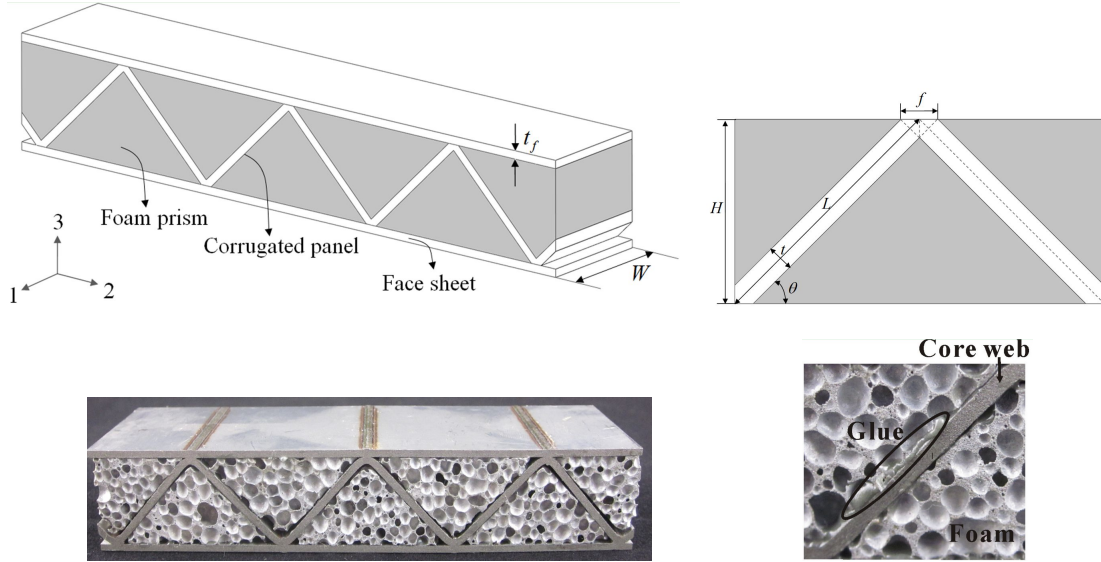


Figure 1. Schematic representation of foam-filled corrugated sandwich plate (top left), unit cell (top right), typical as-fabricated sandwich (lower left), and interface between foam and core web showing good bonding condition (lower right).

constructed in Section 3, and the validity of FE model predictions was checked against experimental measurements. In Section 4, the effects of key geometrical and material parameters were systematically investigated and the physical mechanisms underlying the strengthening effect of foam filling explored. Further, based upon the different deformation modes of post-buckling identified, collapse mechanism maps were constructed. Finally, in Section 5, the strength and energy absorption capabilities of the foam-filled corrugated plates were compared with competing lightweight structures.

2. Specification of foam-filled sandwich plates

The foam-filled corrugated sandwich plate and the corresponding unit cell were shown schematically in Figure 1 (top left and right, respectively). The sandwich structure was characterized by inclination angle θ , core height H , face sheet thickness t_f , width W , strut (core web) thickness t , length L , and foam relative density $\bar{\rho}_f$ (nondimensional) or density ρ_f (dimensional). For convenience, let the density ratio $\bar{\rho}$ be defined as the ratio of the average density ρ_c of the foam-filled corrugated core to the density ρ_s of the strut material as

$$\bar{\rho} \equiv \rho_c / \rho_s = \lambda + (1 - \lambda) \rho_f / \rho_s, \quad (1)$$

where λ denoted the volume fraction of the core occupied by the solid struts. To calculate λ , it was assumed that an overlap region was formed at the joint of two inclined struts, as illustrated in Figure 1 (top right). Accordingly, the height and width of the half unit cell were $H = L \sin \theta$ and $B = L \cos \theta$, whilst the width of the overlap region was $f = t / \sin \theta$. The overlap area may thence be expressed as

$$A_{\text{overlap}} = \frac{t^2}{2 \sin 2\theta}.$$

With the area occupied by the overlap accounted for, one arrived at

$$\lambda = \frac{tL - A_{\text{overlap}}}{HB} = \frac{t/L}{\sin 2\theta} \left(2 - \frac{t/L}{\sin 2\theta} \right). \quad (2)$$

Previously, by considering the area occupied by each strut separately (i.e., ignoring the overlap of Figure 1, top right), Vaziri et al. [2006] obtained an alternative expression as

$$\lambda = \frac{t/L}{t/L + \frac{1}{2} \sin 2\theta}. \quad (3)$$

For illustration, consider the case of $\theta = 45^\circ$ and $\rho_f = 648 \text{ kg/m}^3$. The two predictions were nearly identical for small slenderness ($t/L < 0.05$), but diverged at larger values ($t/L > 0.05$). Further, (2) gave predictions closer to those measured experimentally (mass contribution of epoxy glue ignored; see discussion below). Henceforth, (2) together with (1) were employed in the present study to calculate ρ_c and $\bar{\rho}$.

The fabrication procedures for all-metallic corrugate-cored sandwich plates filled with aluminum foams were straightforward. Corrugated plates were firstly fabricated via a folding operation. Empty (unfilled) corrugated sandwich plates were then assembled by laser welding the face sheets to the folded plates. Subsequently, triangular foam prisms cut by electrodischarge machining (EDM) from close-celled aluminum foam sheet were inserted into the interstices of the empty sandwich and fixed using epoxy glue. As impaired bonding condition between the foam and the face sheets as well as the folded plates may reduce the mechanical performance of the foam-filled sandwiches, the interfaces were treated carefully to minimize the clearance before epoxy glue was applied to fill the gaps.

In the present study, both the face sheets and the corrugated plates were made of 304 stainless steel with density $\rho_s = 7900 \text{ kg/m}^3$. The aluminum foam with closed cells was fabricated via the foaming route, similar to the commercial Alporas foam that had been extensively studied. Aluminum foams with two different relative densities were used, called here as foam I and foam II. Foam I had a relatively high density of $\rho_f = 648 \text{ kg/m}^3$ (porosity 0.76) whilst foam II had a relatively low density of $\rho_f = 324 \text{ kg/m}^3$ (porosity 0.88).

Three kinds of empty sandwich plates having different strut thicknesses ($t = 0.41 \text{ mm}$, 0.82 mm and 1.42 mm), with the remaining morphological parameters fixed at $\theta = 45^\circ$, $H = 17 \text{ mm}$, $t_f = 1.42 \text{ mm}$ and $W = 20 \text{ mm}$, were fabricated. Correspondingly, foam-filled sandwiches using both foam I and foam II were fabricated. A typical foam-filled sandwich plate was shown in Figure 1 (bottom left). The interface between the foam and the core web was highlighted in Figure 1 (bottom right), indicating that good bonding condition had been achieved. Both the empty and foam-filled sandwich plates were tested under out-of-plane (direction-3 in Figure 1, top left) compression, with constant displacement loading rate of 10^{-4} s^{-1} (corresponding to a loading speed of 0.12 mm/min) at room temperature. The measured results were used later to compare with analytical predictions for the compressive strength of foam-filled sandwiches and to validate FE simulations. More details of the experiments were referred to Yan et al. [2013], who also provided preliminary FE simulation results.

3. Finite element modeling

3.1. Constitutive model and material specifications. The parent material (as-brazed 304 stainless steel) of the core webs and the face sheets was modeled as an isotropic and homogeneous elastic-plastic solid of elastic modulus $E_s = 210$ GPa, Poisson ratio $\nu = 0.3$, yielding stress $\sigma_Y = 210$ MPa, and linear hardening with tangent modulus $E_t \equiv d\sigma/d\epsilon \approx 2.1$ GPa. The classical theory of flow plasticity based on the von Mises yield surface and isotropic hardening was applied, whilst the quasistatic tensile stress versus strain curve of 304 stainless steel was taken directly from [Côté et al. 2006]. The steel was assumed sufficiently ductile to sustain large strains without fracture, as confirmed by experiments.

The isotropic phenomenological constitutive model of Deshpande and Fleck [2000] for metallic foams was employed to model the aluminum foam insertions. With isotropic hardening assumed, the yield surface of the foam was defined as

$$\hat{\sigma} - Y = 0 \quad (4)$$

where Y represented the size of the yield ellipse, and $\hat{\sigma}$ was the equivalent stress given by

$$\hat{\sigma}^2 \equiv \frac{1}{1 + (\beta/3)^2} [\sigma_e^2 + \beta^2 \sigma_m^2], \quad (5)$$

$$Y = \sigma_e \sqrt{1 + \left(\frac{\beta}{3}\right)^2}. \quad (6)$$

Here, $\sigma_e = \sqrt{3s_{ij}s_{ij}/2}$ was the von Mises equivalent stress, $\sigma_m \equiv \sigma_{kk}/3$ was the mean stress, s_{ij} was the deviatoric stress, whilst β was a material parameter representing the ratio of deviatoric strength to hydrostatic strength. The normalization factor on the right hand side of (5) ensured that $\hat{\sigma}$ was equal to the stress in a uniaxial tension or compression test. With the normality of plastic flow assumed, the ‘‘plastic Poisson’s ratio’’ $\nu_p = -\dot{\epsilon}_{22}^p/\dot{\epsilon}_{11}^p$ for uniaxial compression in direction 1 was given by

$$\nu_p = \frac{1/2 - (\beta/3)^2}{1 + (\beta/3)^2}, \quad (7)$$

from which

$$\beta = \frac{3}{\sqrt{2}} \sqrt{\frac{1 - 2\nu_p}{1 + \nu_p}}. \quad (8)$$

Figure 2 presented the experimentally measured uniaxial compressive stress versus strain curves of foam I (porosity 0.76) and foam II (porosity 0.88). For foam I, the plastic Poisson ratio ν_p was measured to be 0.21, thus $\beta = 1.47$. Other parameters were also measured for foam I, as: $E_f = 2.61$ GPa, $\nu_f = 0.3$, and $\sigma_{\text{plateau}} \approx 14.5$ MPa. For foam II, $\nu_p \approx 0$ (and hence $\beta \approx 2.12$), $E_f = 157$ MPa, $\nu_f = 0.3$, and $\sigma_{\text{plateau}} \approx 3.0$ MPa. Note that, due to alloying, foam I exhibited somewhat brittleness as a result of successive fracturing of cell membranes. This led to the wiggling of the stress versus strain curve once initial yielding was initiated, yet a long plateau regime typical for aluminum foams was still present (Figure 2). For the purpose of FE simulation with the commercial code Abaqus, the stress versus strain curve of foam I was smoothed as illustrated in Figure 2.

For both foam I and foam II, the average cell size was approximately 2.5 mm, allowing at least seven cells along each leading dimension of the foam-filled sandwich core. Consequently, it was considered

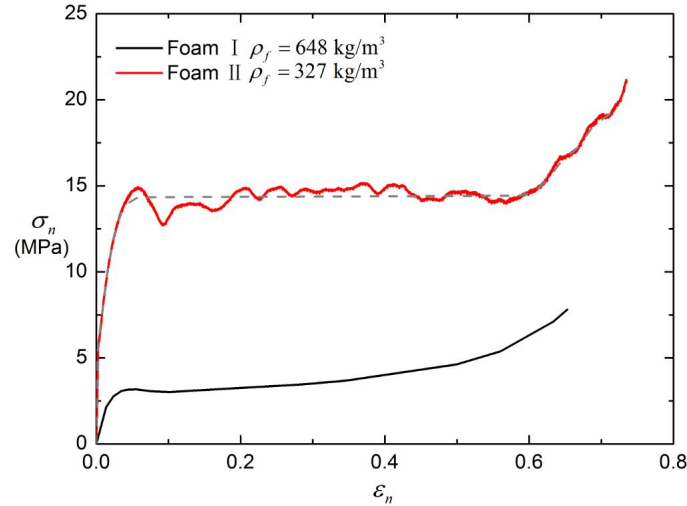


Figure 2. Compressive stress versus strain curve of close-celled aluminum foams measured at strain rate of 10^{-4} s^{-1} .

reasonable to use the phenomenological constitutive model to describe the macroscopic mechanical properties of the filling foam.

3.2. Finite element model. Experimentally it was observed that, at large nominal compressive strains (direction 3; see Figure 1, top right), partial extrusion of the foam insertions occurred along direction-1 and the foam-filled sandwich plate exhibited slight transverse buckling along the same direction. Consequently, three-dimensional (3D) FE models were developed using ABAQUS/Explicit (NLGEOM=YES in ABAQUS notation), with eight-node linear brick elements having reduced integration (C3D8R) adopted. Whilst the element size was set at about $H/50$ for the whole model, it was about $t/6$ for the core web along the thickness direction. It was established that the accuracy of the calculations was not improved appreciably with additional mesh refinements.

Geometrical imperfections were inevitable in corrugate-cored sandwich structures. However, for the present foam-filled sandwich plates, it was found that good agreement between experimentally measured uniaxial compressive stress versus strain curves and those predicted using FE simulations was achieved without considering any initial geometrical imperfections (Figure 3). Therefore the influence of geometrical imperfections was neglected in the present study.

As previously mentioned, to fabricate the sandwich plates, a thin film of epoxy glue was used to bond the foam prisms to the core webs and face sheets. To investigate the influence of interfacial bonding between stainless steel and aluminum foam on peak load and energy absorption, Yan et al. [2013] carried out FE simulations for foam-filled sandwich panel having both perfectly bonded and unbonded interfaces. It was demonstrated that the simulated results with perfect bonding matched better with experimental measurements, suggesting that the use of epoxy glue provided good bonding between aluminum foam and stainless steel (see Figure 1, bottom right). Although debonding was indeed observed when large plastic deformation occurred, all subsequent FE simulations were based on perfect bonded interfaces as the present mechanism analysis aimed to focus on the early stage of deformation (compressive strain not

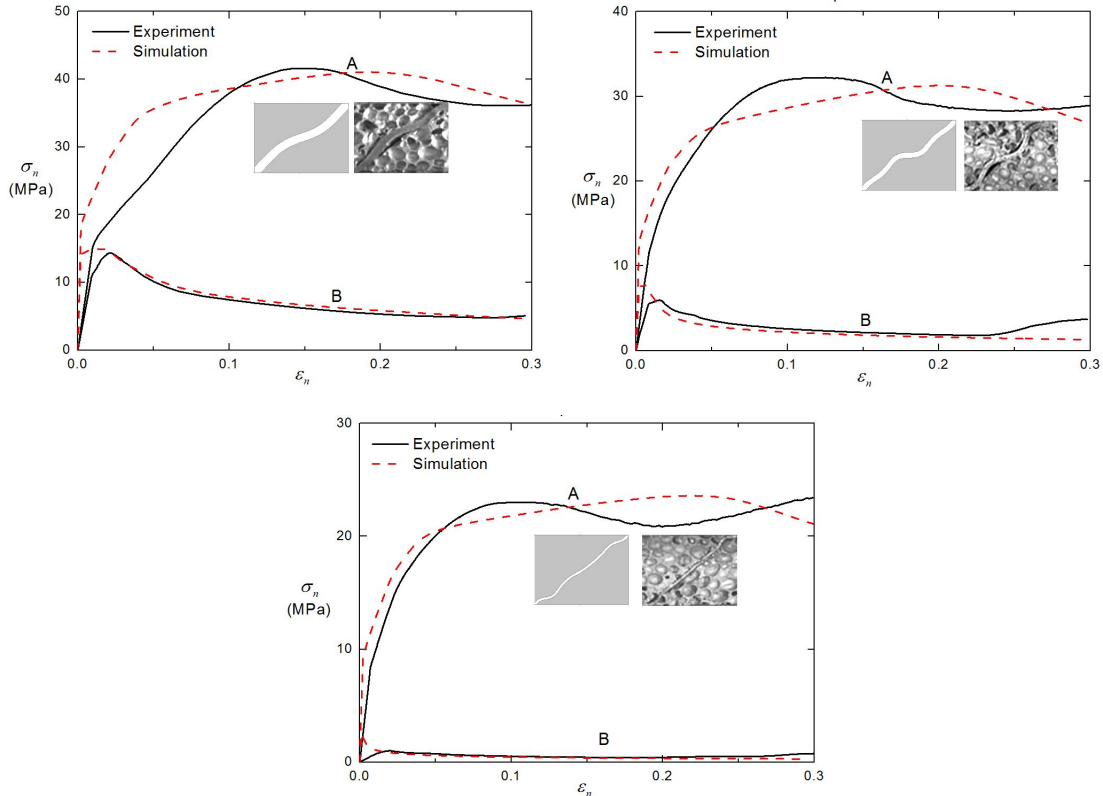


Figure 3. Comparison of FE simulated nominal compressive stress versus nominal compressive strain curves with those measured: specimen 1 ($t/L = 0.059$) (top left); specimen 2 ($t/L = 0.034$) (top right); specimen 3 ($t/L = 0.017$) (bottom). Both inserted photo and FE simulation of deformation mode correspond to $\epsilon_n = 0.30$. Curve A denoted compressive response of foam-filled core, whilst curve B denoted the corresponding empty core, with inclination angle fixed at $\theta = 45^\circ$ and foam I used as insertions.

exceeding 0.30). In the FE model, the perfectly bonded interfaces between foam prisms and struts (as well as face sheets) were modeled using the Tie option provided in ABAQUS.

To simplify the calculations, only half of the unit cell was employed as the representative volume element (RVE), with symmetric boundary conditions applied on the two edge-planes parallel to direction-3, as shown in Figure 4 (left). Both the top and bottom face sheets were set as rigid surfaces. The bottom face was fixed while the top face was displaced in direction-3 only, with a constant loading rate of 1.0 s^{-1} . The loading rate was sufficiently low to ensure that the simulated crushing response was quasistatic. The absence of significant oscillations in the resulting load versus deflection curves and the small kinetic energy acquired by the sandwich core (less than 5% of the strain energy) confirmed the validity of the approach, as suggested in the ABAQUS documentation [DSSC 2007]. Further, the lack of symmetry about the centroid of either the empty or foam-filled core was sufficient to cause a preferential buckling direction of the sandwich. Finally, as shown in Figure 4 (right), additional calculations with more unit

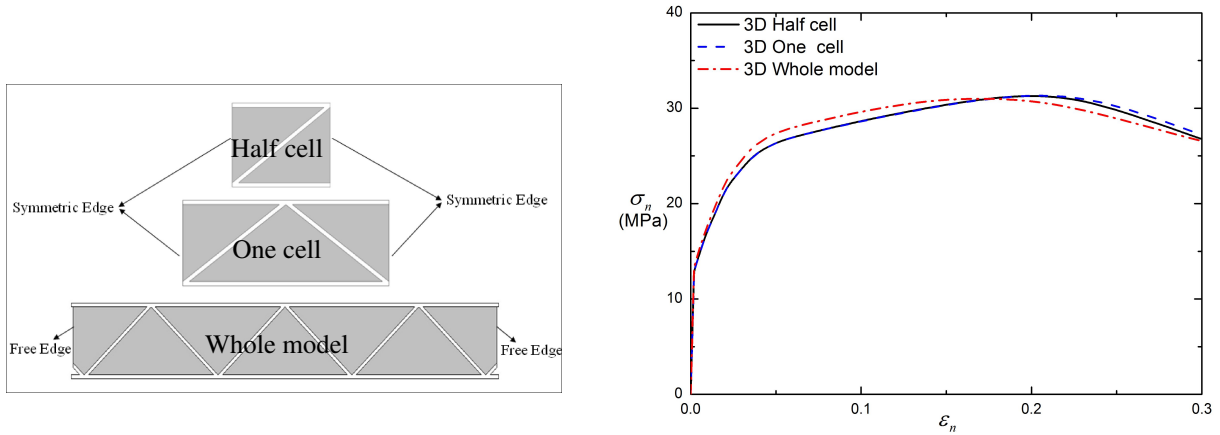


Figure 4. FE model (left): half cell and one cell with symmetric edges, as well as whole model with free edges (just like the specimen shown in Figure 1, bottom left). On right: influence of cell number upon simulated compressive response of a foam-filled corrugated sandwich with $t/L = 0.0341$, $W/H = 1$, $\theta = 45^\circ$, and foam I as the fillers.

t/L	foam I-filled core		Empty corrugated core		
	Test (MPa)	FE (MPa)	Test (MPa)	FE (MPa)	Theory [†] (MPa)
0.017	23.02	23.60	1.04	3.56	3.69
0.034	32.20	31.26	5.94	8.02	7.37
0.059	41.61	41.07	14.38	14.94	13.85

Table 1. Comparison of FE predictions with test results of compressive strength for both empty and foam I-filled cores with $\theta = 45^\circ$ and varying core web slenderness ratios. [†]Analytical prediction for buckling of empty corrugated core was outlined in the Appendix.

cells were performed, giving nearly identical results as those obtained by using the RVE model. Thus, in all subsequent FE calculations, the half cell model with symmetric edges was employed as the RVE.

3.3. Validation against experimental measurement. Experimental measurements under quasistatic out-of-plane compression were carried out following Yan et al. [2013]. Table 1 compared the FE simulation results with experimental measurements for the compressive strength (peak compressive stress) of both empty and foam I-filled corrugated cores, with the inclination angle fixed at $\theta = 45^\circ$ and the strut slenderness ratio t/L varied as 0.059, 0.034 and 0.017 (i.e., specimen 1, specimen 2 and specimen 3 in Figure 3). The corresponding stress versus strain curves were presented in Figure 3, together with the FE simulated and experimentally measured deformation modes of the foam-filled core at $\epsilon_n = 0.30$.

Existing studies [Côté et al. 2006; Yan et al. 2013] suggested that the collapse of empty corrugated plates under out-of-plane compression was governed by Euler buckling for thin plates and global plastic

buckling for thick plates. In contrast, the foam-filled corrugated plates deformed by forming more plastic hinges and exhibited no obvious softening after the peak stress was reached (Figure 3), increasing significantly its specific strength and energy absorption, as previously mentioned by Yan et al. [2013].

For the peak compressive stress, the results of Table 1 demonstrated that, overall, good agreement was achieved between FE simulation and measurement. In particular, the errors of the peak stress between FE simulation and measurement for foam-filled corrugated cores were only 1.3% ~ 2.9%. There was also good agreement between FE simulated and experimentally measured stress versus strain curves (Figure 3). Further, the deformation and collapsing modes of the foam-filled cores were accurately captured by the FE simulation. The results shown above served to confirm the fidelity of the FE simulations for the foam-filled corrugated cores. As geometrical imperfections were neglected in the present FE modeling, the results of Table 1 and Figure 3 also indicated that the compressive properties of foam-filled corrugated cores were insensitive to the presence of geometrical imperfections.

For the empty corrugated cores, however, the discrepancy between simulation and measurement increased as the core web thickness was reduced; see Table 1. This was understandable, as the compressive properties of empty corrugated cores were sensitive to the presence of geometrical imperfections in particular when the core web was relatively thin. As previously mentioned, the present FE simulations ignored the effects of geometrical imperfections whilst, in reality, such imperfections were inevitable during the fabrication of the corrugated core.

Under the assumption that the core webs were slender, its out-of-plane compressive strength may be analytically predicted, as demonstrated in the Appendix. For the present empty corrugated cores considered, the analytically predicted compressive strength was listed in Table 1. Whilst the analytical prediction overestimated the experimentally measured compressive strength, it agreed quite well with that calculated numerically. This was attributed to the fact that both the theory and FE simulation ignored the effects of geometrical imperfections.

Finally, it should be mentioned that the present FE simulations were carried out up to the nominal compressive strain of 0.30, beyond which the discrepancy between the simulation and the experiment notably increased. This was because that, at large strains, the large rotation of the plastic hinges caused foam/strut interfacial debonding and the foam insertions began to be squeezed out (along direction-1) of the interstices of the corrugated core.

4. Results and discussion

In this section, using the experimentally validated FE methodology, we carried out a systematic study over a wide range of corrugation configurations, characterized by $0.005 \leq t/L \leq 0.3$, $35^\circ \leq \theta \leq 65^\circ$, and $W/H = 1$. For each configuration, three different kinds of sandwich panels having foam I-filled, foam II-filled, and empty corrugated cores were considered. The aim was to explore in detail the physical mechanisms underlying the strengthening effect of foam insertions and construct the collapse mechanisms map for the foam-filled cores.

4.1. Strengthening effects of foam insertions.

4.1.1. Crushing response and strengthening mechanisms. Details concerning the FE calculated compressive response of a typical foam-filled corrugated core (specimen 2), with inclination angle $\theta = 45^\circ$,

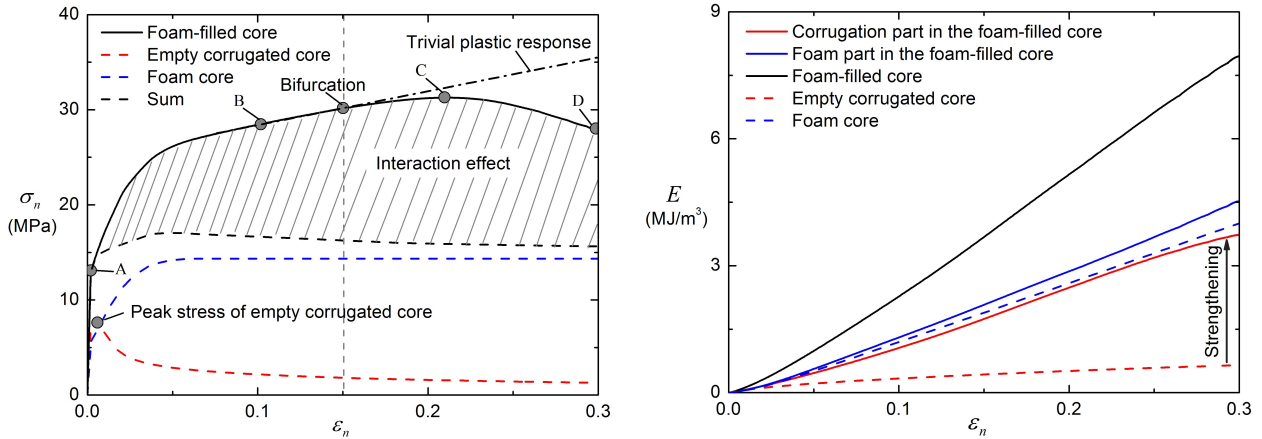


Figure 5. Finite element simulation results: nominal compressive stress versus nominal compressive strain curves (left) and energy absorbed by foam-filled core and its constituents plotted as functions of nominal compressive strain (right), with $\theta = 45^\circ$, $t/L = 0.034$ and foam I insertions.

slenderness ratio $t/L = 0.034$ and foam I insertions, were presented in Figure 5, which had all the common features of foam-filled cores under quasistatic out-of-plane compression.

Figure 5 (left) presented the nominal compressive stress (σ_n) versus nominal compressive strain (ϵ_n) curve up to $\epsilon_n = 0.30$. The red and blue dash lines represented separately the crushing responses of the empty core and foam I, the black dash line was the sum of the two, whilst the black solid line denoted the response of the foam-filled core as a whole. The interaction effect (represented by the shaded area in Figure 5, left) between the filling foam and the core web was strong, not only enhancing significantly the peak stress but also reduced considerably core softening once the peak stress was reached.

It is seen from Figure 5 (left) that the nominal compressive stress of the foam-filled core increased linearly with increasing strain till the first inflection point A ($\epsilon_n \approx 0.0012$), which signified core yielding. Subsequently, the curve entered a nonlinear region, due to material nonlinearity of both the strut material and foam I. In particular, the core behaved in a stable manner once the stress plateau of the foam insertions was reached, exhibiting nearly linear plastic hardening over a large range of ϵ_n as a result of the plastic hardening of 304 stainless steel. As the strain was further increased to $\epsilon_n \approx 0.15$, bifurcation was observed at the intersection between the lines of extended trivial plastic response and the actual response. Note from Figure 5 (left) that after the nonlinearity of the stress versus strain curve due to material nonlinearity, there was a linear segment (within the range of compressive strain 0.07–0.15) of the curve before strut buckling occurred. This linear response and its extension (dashed line in Figure 5, left) was defined here as the trivial plastic response, just as the elastic trivial response shown in Figure 7 of [Wilbert et al. 2011]. At the bifurcation point marked on the curve, the strut started to buckle and hence the actual stress strain curve deviated from such trivial response as shown in Figure 5 (left). Subsequently, the tangent modulus started to drop and the nonlinearity at kinematic levels showed up as plastic bending was initiated in the struts. With further compression, the extended bending deformation led to strut collapse at which point

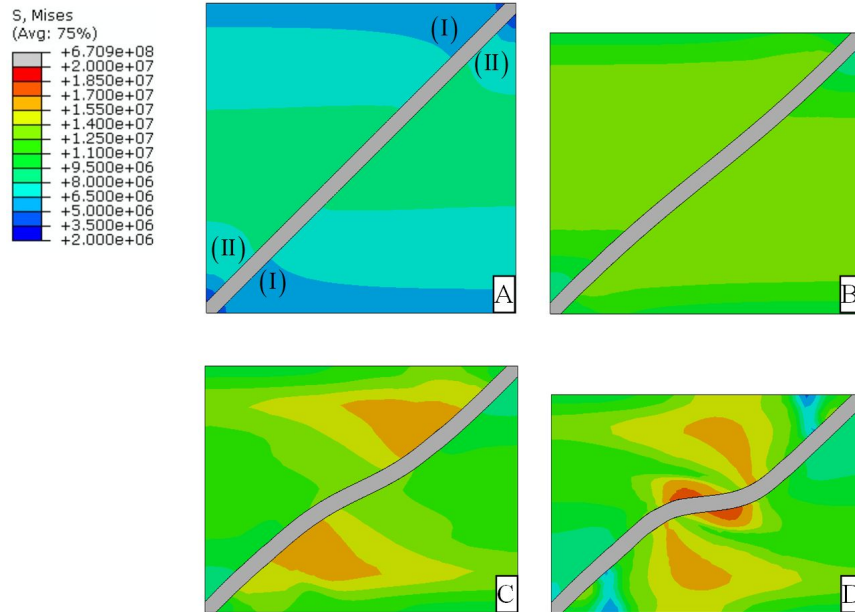


Figure 6. Contours of von Mises stress in foam insertions at specific strains corresponding to the four specified points of Figure 5 (left).

the peak stress of the core was reached. In comparison with the empty core, the peak stress corresponding to point C of Figure 5 (left) was considerably delayed due mainly to foam/strut interaction.

To explore further the strengthening effect of foam insertions, Figure 4 (right) presented the internal energy (plastic dissipative energy and strain energy) for each constituting element of the foam-filled core; corresponding results for the empty core and the foam itself were also presented. The internal energy, defined here as the energy absorbed by each constituting element, was calculated by integrating stress with respect to strain (up to overall nominal compressive strain of 0.3), which were extracted from the post-processing of ABAQUS. The kinematic energy was neglected as the loading rate was sufficiently low. From Figure 5 (right) it was clear that the strengthening was mainly attributed to the dramatic enhancement of the strut, as its internal energy per unit volume was greatly enhanced relative to that in the empty core. Simultaneously, the energy per unit volume of the foam insertions was also increased, although not as dramatic.

For the foam insertions, Figure 6 presented a set of contours of the von Mises equivalent stress in the central cross-section ($x_1 = W/2$; Figure 1, top left) of the RVE for selected compressive strains as marked in Figure 5 (top left). During the early stage of compression (contour A), the main regimes of the equivalent stress originated from the core center, and expanded gradually to the top and bottom faces with increasing compression. At $\epsilon_n = 0.10$ (contour B), the distribution of the equivalent stress was nearly layer-wise homogeneous, averaging to about 14.5 MPa, which equaled approximately the plateau stress of foam I (Figure 2). This implied that the foam deformation was dominated by the compressive stress along the loading direction (direction-3), resulting in almost the same response as that of uniaxially compressed foam I (Figure 2). However, under out-of-plane compression, the stress

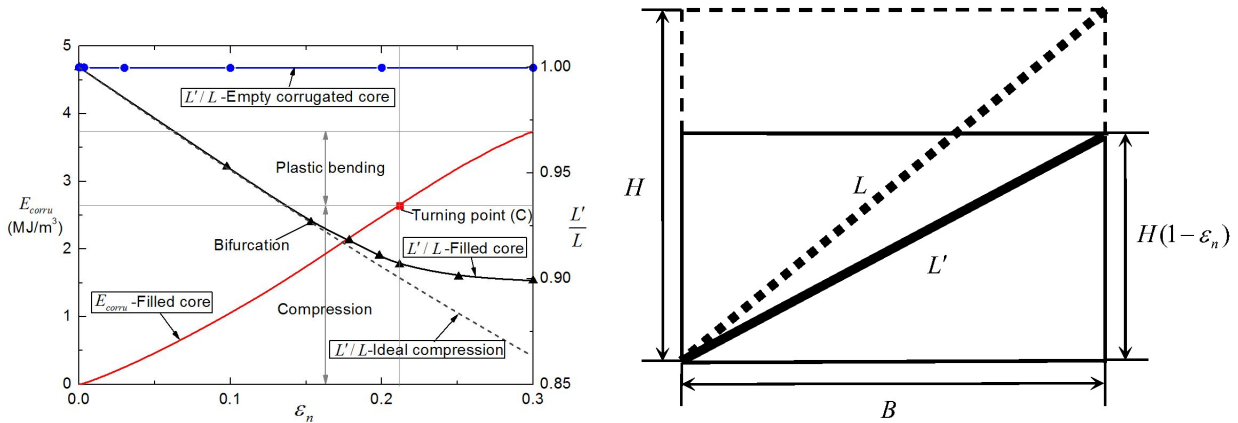


Figure 7. Left: energy absorbed by corrugated plate and length reduction of its middle line plotted as functions of nominal compressive strain, with $\theta = 45^\circ$, $t/L = 0.034$, and foam I insertions. Red square point defined as the “turning point” referred to the peak stress of foam-filled corrugated plates. Right: Sketch of an inclined strut experiencing only axial compression: dotted and solid bold lines denoted separately initial and deformed middle lines of the strut.

state in the foam insertion was asymmetric around the two ends of the corrugated plate, as shown in contours A and B. Let the foam region adjacent to the face sheet be defined as region I and the others be defined as region II, as shown in contour A of Figure 6. Initially, the stressing and foam densification in region II was more intense than that in region I. As the compressive strain was increased, region I was gradually enlarged, as shown in contour B. That the stress in region I was greater than that in region II caused a rotational moment on the corrugated plate, inducing odd-symmetrical bending (see discussion later concerning Figure 20). As a result of the bending deformation, severe stress localization occurred, inducing complicated combination of compression, tension, and shear as well as localized densification in the foam surrounding the bent corrugated plate, as illustrated in contours C and D. Correspondingly, the amount of energy absorbed by the foam insertion noticeably increased.

Note that the deformation of the corrugated plate shown in contour D of Figure 6 was somewhat different from that in Figure 3 (top right) at the same strain level of $\epsilon_n = 0.30$. This was expected, as for the present 3D sandwich configurations with finite width W (Figure 1), the constraints provided by the foam insertions on the corrugated plates were not homogeneous along the direction-1, relatively weak closer the free boundaries of the sandwich. Unless otherwise stated, the deformation and collapse modes discussed latter were all referred to the central cross-section of the RVE.

Consider again specimen 2. Let E_{corr_u} denote the energy absorption of the corrugated plate in the foam-filled core per unit volume and L'/L denote the normalized length change of the middle line (the reference line) of the corrugated plate, representing the deformed state of the latter. Figure 7 (left) plotted separately E_{corr_u} and L'/L as functions of the compressive strain ϵ_n . By assuming that the strut experienced only axial compressive deformation (i.e., length change due to bending excluded) as shown in Figure 7 (right), the normalized length of the middle line of the strut after deformation may be

expressed as

$$\frac{L'}{L} = \sqrt{\frac{H^2(1 - \epsilon_n)^2 + B^2}{L^2}} = \sqrt{\sin^2 \theta (1 - \epsilon_n)^2 + \cos^2 \theta}. \quad (9)$$

For comparison, the prediction from the above equation was also plotted (dashed line) in Figure 7. The actual length change of the corrugated plate coincided with that calculated with Equation (9) until the bifurcation point was reached (see also Figure 5 (left)). This implied that, before bifurcation occurred, the corrugated plate experienced only axial compression along its middle axial line. However, after the bifurcation, the corrugated plate lost stability and collapsed, with its deformation gradually shifting from axial compression to bending. Correspondingly, the rate at which its length decreased slowed down (Figure 7, left). After the turning point corresponding to the peak stress of the foam-filled core (point C in Figure 7, left), the length of the corrugated plate was almost unchanged, indicating that its deformation was now dominated by bending. In comparison, the length of the corrugated plate in an empty (unfilled) sandwich remained unchanged, as bending rather than axial compression dominated its deformation under out-of-plane compression.

Before the turning point was reached, the energy absorbed by the corrugated plate, E_{corr} , was dominated by axial compression, exhibiting a slightly accelerated growth as the nominal compressive strain ϵ_n was increased (Figure 7). Beyond the turning point, the energy absorption was mainly attributed to plate bending, with decelerated growth. In other words, for foam-filled cores, whilst the deformation of the corrugated plate was dominated by axial compression during the pre-buckling stage (before the peak stress was reached), bending deformation played the dominant role in the post-buckling regime. Further, with aluminum foam insertions, not only was the buckling of the corrugated plate greatly delayed, leading to significantly enhanced peak stress of foam-filled cores, but also much less obvious softening in the post-buckling regime. Similar results were recently observed experimentally in polymer lattice structures filled with polyurethane foams [Ostos et al. 2012].

4.1.2. Effect of inclination angle. Figure 8 presented the predicted overall compressive responses of both foam-filled and empty corrugated cores for selected inclination angles of θ and fixed core web slenderness ratio of $t/L = 0.02$. In general, as θ was increased, both the strength and energy absorption of the sandwich core increased. Further, the stress versus strain curves (up to $\epsilon_n = 0.30$) of the foam-filled cores with smaller inclination angles were smoother. For small inclination angles especially when $\theta \leq 35^\circ$, the contribution by the core web to load bearing was relatively small in comparison with that by the foam insertions; therefore, the foam insertions dominated the load bearing, leading to smoother compressive curves of the sandwich cores (Figure 8). Irrespective of the inclination angle, the critical strain at which the core web collapsed (plastically buckled; corresponding to the peak stress of Figure 8) was remarkably delayed with foam filling, particularly so if the foam relative density was large (e.g., foam I). In comparison, in the absence of foam filling, the core web easily collapsed with a tiny critical strain (ranging from 0.002 to 0.004; Figure 8, bottom).

With the core web slenderness ratio fixed at $t/L = 0.02$, the results of Figure 8 suggested that the compressive properties of corrugated cores filled with either foam I or foam II were considerably superior to those of empty cores. Further, the filling of a denser foam (i.e., foam I) led to larger specific strength and energy absorption per mass, almost twice those obtained with foam II insertions.

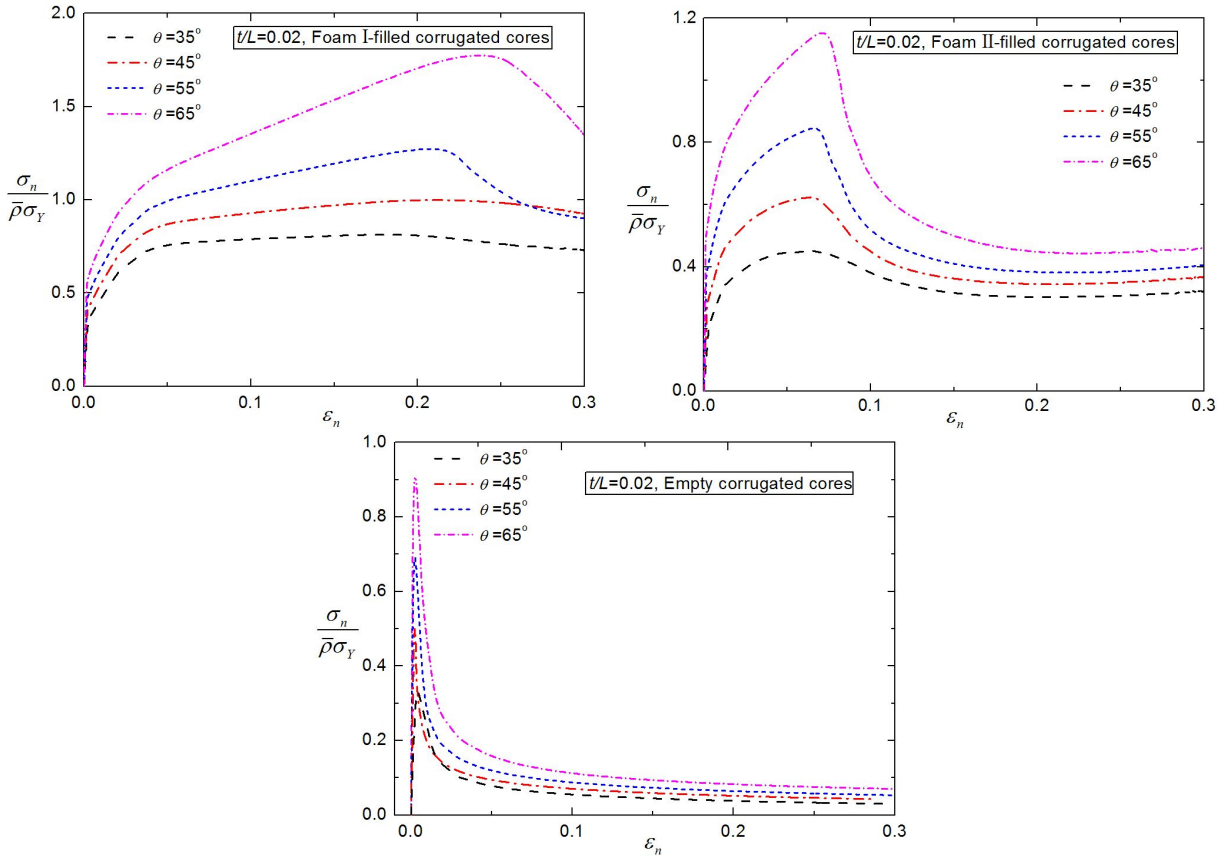


Figure 8. Normalized nominal compressive stress versus nominal compressive strain curves for selected inclination angles: foam I-filled cores (top left); foam II-filled cores (top right); empty cores (bottom). Core web slenderness ratio fixed at $t/L = 0.02$.

To explore further the strengthening mechanisms of foam insertions, the effects of inclination angle on energy absorption per unit mass (up to $\epsilon_n = 0.30$) were presented in Figure 9 (top left) for both empty and foam-filled cores, in Figure 9 (top right) for corrugated plates only, and in Figure 9 (bottom) for foam insertions only. As reference, the corresponding results for foam I and foam II were also plotted in Figure 9 (bottom). With foam filling, not only was the energy absorption capability of the core webs significantly enhanced, but also was the energy absorption capability of the foam itself enhanced (due to complex stressing); see Figure 9 (top right and bottom). Moreover, as θ was increased, whilst the amount of energy absorbed by the core webs in the foam-filled core increased appreciably, that absorbed by the foam insertions remained more or less unchanged.

Figure 10 plotted separately the normalized length reduction and maximum lateral deflection of the core web (up to $\epsilon_n = 0.30$) as functions of the inclination angle for both foam-filled and empty corrugated cores having fixed core web slenderness ratio of $t/L = 0.02$. Again, for empty cores, the length of the core web remained almost unchanged ($\delta/L = 0$; $\delta \equiv L - L'$ denoted the length reduction) as θ was varied, with deformation dominated by plate bending. For foam-filled cores, whilst increasing θ led to

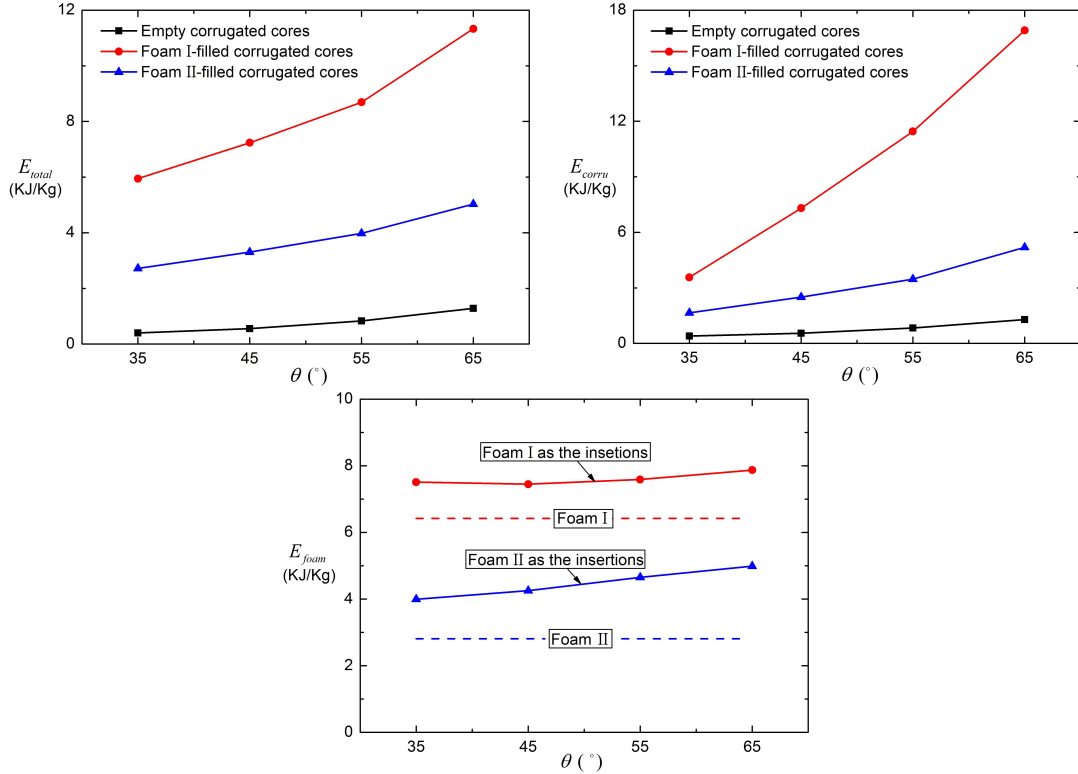


Figure 9. Effect of inclination angle on energy absorption per unit mass (up to nominal compressive strain of 0.30) for empty and foam-filled cores (top left), corrugated plates only in empty and foam-filled cores (top right) and foam insertions only in foam-filled cores (bottom), with corresponding results for foam I and foam II under out-of-plane compression also plotted as reference. Core web slenderness ratio fixed at $t/L = 0.02$.

increasing axial compression (length reduction) of the core web, the length reduction was more severe in the presence of denser foams. Although the maximum lateral deflection of the core web also increased with increasing θ , the variation trend was opposite to that of its length reduction: for a fixed inclination angle, the core web in an empty core exhibited the largest deflection whilst that in foam I-filled core had the least deflection; see Figure 10 (right).

4.1.3. Effect of core web slenderness ratio. Let σ_p denote the peak compressive stress and E denote the energy absorption per unit volume of the RVE up to $\epsilon_n = 0.30$. For both foam-filled and empty corrugated cores, Figure 11 (left) plotted the specific strength, $\sigma_p/(\bar{\rho}\sigma_Y)$, as a function of slenderness ratio t/L , with the inclination angle fixed at $\theta = 45^\circ$. Corresponding results for specific energy absorption, $E/(0.3\bar{\rho}\sigma_Y)$, were presented in Figure 11 (right). Although not shown here, similar results for other inclination angles were also obtained.

With increasing t/L , both the specific strength and specific energy absorption increased, and the increase was more significant at large t/L values with or without foam filling. For empty cores, except for the stable compression regime corresponding to sufficiently large values of t/L , the specific strength

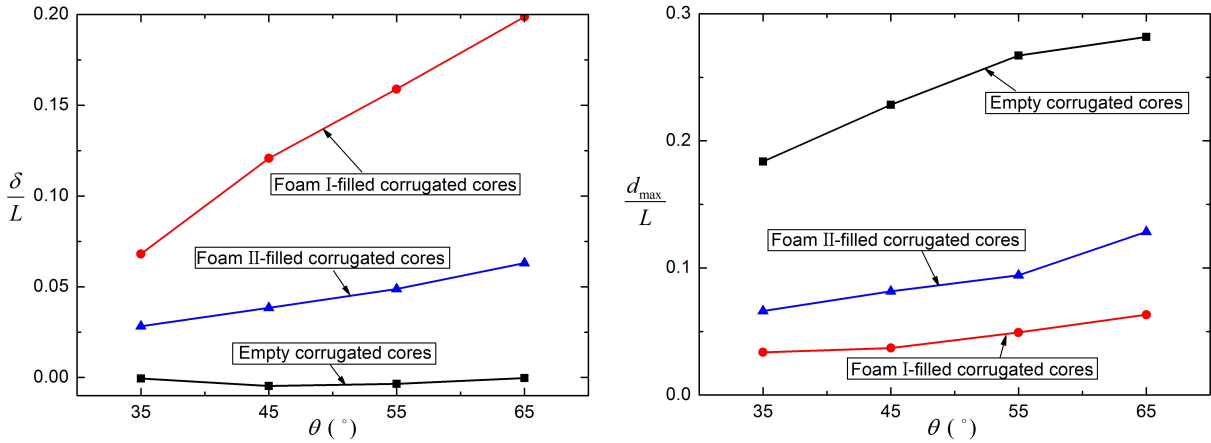


Figure 10. Normalized length reduction (left) and normalized maximum lateral deflection (right) of core web (up to nominal compressive strain of 0.30) plotted as functions of inclination angle for both foam-filled and empty corrugated cores. Core web slenderness ratio fixed at $t/L = 0.02$.

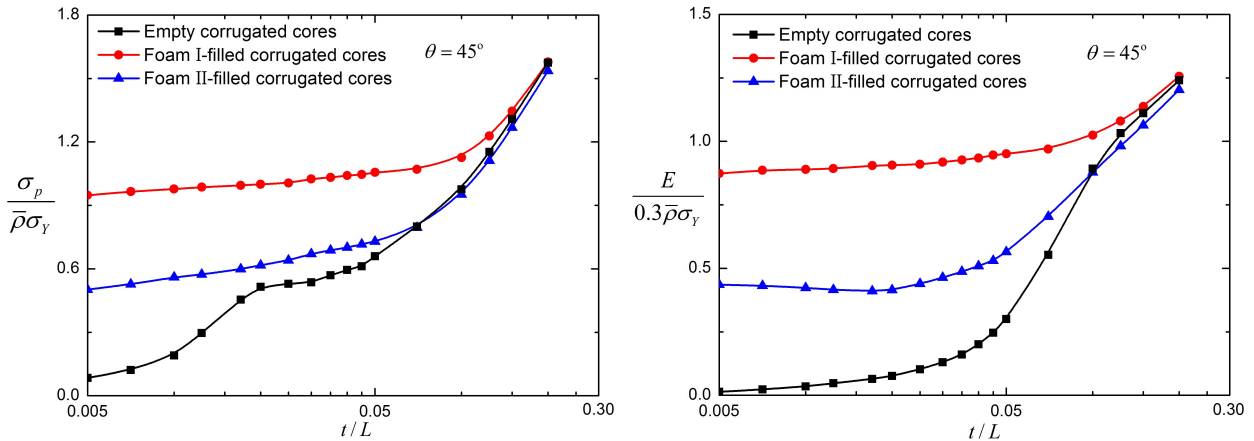


Figure 11. Specific strength (left) and specific energy absorption (right) plotted as functions of core web slenderness ratio t/L for both foam-filled and empty cores, with fixed inclination angle of $\theta = 45^\circ$.

curve may be divided into two distinct regimes corresponding to elastic Euler buckling and plastic buckling of the core web, respectively, the former considerably more steeper than the latter (Figure 11, left). In contrast, with foam filling, the core web collapsed only with plastic buckling, although the types of plastic buckling may be different (see the next section) and hence the specific strength curve was much smoother than that of the empty core.

In terms of compressive strength and energy absorption, the superiority of foam-filled cores over empty ones was the greatest when the core web slenderness ratio was relatively small ($t/L \leq 0.02$). As previously mentioned, within this regime, the collapse mode of the empty core was dominantly elastic

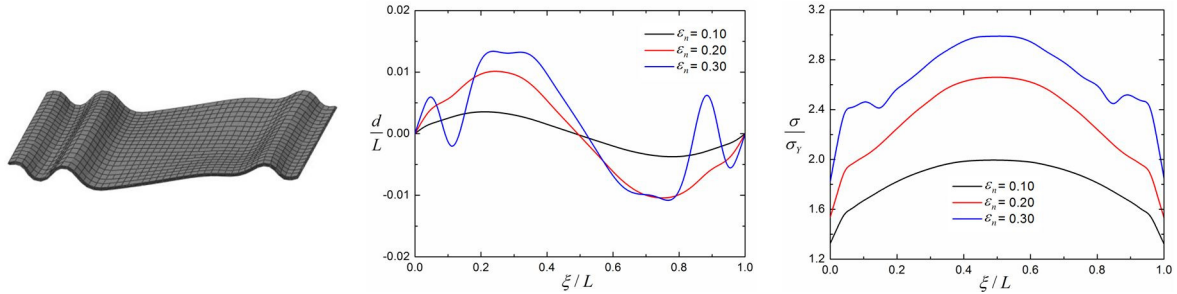


Figure 12. Sides local-buckling: $t/L = 0.007$, $\theta = 45^\circ$, foam I-filled corrugated core.

Euler buckling. In sharp contrast, at large values of $t/L (> 0.1)$, stable compression with plastic hardening occurred in both empty and foam-filled cores, and the strengthening effect of foam filling gradually vanished (Figure 11).

The results of Figure 11 revealed that the beneficial effect of foam filling on specific energy absorption was more obvious than that on specific strength. The foam fillers not only greatly delayed core web buckling and elevated the compressive strength, but also improved significantly the flow stress of post-buckling [Ostos et al. 2012].

4.2. Collapse modes and collapse mechanism maps. Under quasistatic out-of-plane compression, extensive FE simulations were carried out to explore how the collapse mode of an empty corrugated core would vary when its interstices were filled with aluminum foams. For a given core type (filled or unfilled), the dependence of its collapse mode on inclination angle θ and core web slenderness ratio t/L was also determined. As the deformation state at peak load was not obvious especially for foam I-filled cores, the selected collapse modes presented in Figures 12–16 all corresponded to $\epsilon_n = 0.30$ in the post-buckling regime. For comparison, the two typical collapse modes shown in Figures 17–18 for the empty core were also calculated at $\epsilon_n = 0.30$.

For simplicity, the middle axial line of the core web located at the central cross section of the RVE was selected as the analysis object. In Figures 12–18, together with the collapse modes given in the left-most parts, the evolution of deformation and von Mises stress along such middle line for each mode were separately plotted in the middle and right-most parts for selected nominal strain levels. In these figures, ξ/L denoted the relative location of an arbitrary point along the middle line of the core web, whilst d/L and σ/σ_y represented the normalized lateral deflection and normalized equivalent stress of the corresponding point, respectively.

It should be pointed out that the present study did not cover thin-walled ($t/L < 0.005$) and thick-walled ($t/L > 0.3$) corrugated plates, as the buckling of thin plates was highly imperfection sensitive whilst the use of thick plates was limited for weight-sensitive applications. Further, within the regime of $t/L < 0.005$, the collapse was governed by plasticity-moderated elastic buckling and it was problematic to obtain accurate FE results, analogous to thin-walled tubes [Pingle et al. 2011].

4.2.1. Collapse modes of foam-filled corrugated core. Under quasistatic out-of-plane compression, as the values of t/L and θ were systematically varied, a total of five distinct collapse modes, denoted separately as A, B, C, D and E, were identified for the foam-filled corrugated cores, as shown in Figures 12–16.

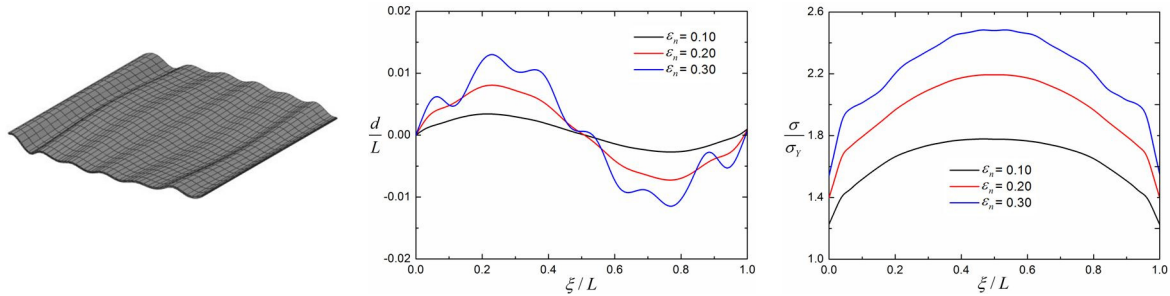


Figure 13. Plastic wrinkling: $t/L = 0.006$, $\theta = 35^\circ$, foam I-filled corrugated core.

For each collapse mode, its regime of dominance was marked on the collapse mechanism map, which was plotted in Figure 19 on a chart of t/L and θ . The characteristics of each mode were discussed below.

Mode A: sides local-buckling. Such buckling mode may occur only in foam I-filled corrugated cores having small values of t/L and inclination angle larger than 35° (Figure 19, top left). As shown in Figure 12, localized plastic hinges emerged only near the ends of the corrugated plate and did not expand to the middle region. Since t/L was small, the lateral support provided by the relatively dense foam I (versus foam II) to the corrugated plate was large, preventing its bending deformation in the middle region. In contrast, towards the ends of the plate, the constraint was not strong enough, causing localized buckling as well as fluctuation of the von Mises equivalent stress in this region (Figure 12, right). This particular buckling mode may be attributed to the heterogeneous distribution of foam constraints on the deformation (deflection) and buckling of the corrugated plate.

Mode B: plastic wrinkling. The mode of “plastic wrinkling” could occur in corrugated plates having small values of t/L (less than 0.015) and filled with either foam I with small inclination angles (less than 45° ; see Figure 19, top left) or foam II (Figure 19, top right). This collapse mode appeared with small buckle waves along with global odd-symmetrical bending, similar to a dual-frequency buckling mode, as illustrated in Figure 13 (left). Interestingly, due to the early formation of global bending, wrinkling with small buckle wave length appeared along with one complete sine-wave shape at large strain (Figure 13, middle), which was quite different from the traditional wrinkling [Hadi 2001]. The equivalent stress exhibited only slight fluctuations (Figure 13, right) due to the relatively small lateral deflections (Figure 13, middle) of the corrugated plate associated with wrinkling.

Mode C: middle local-buckling. As shown in Figure 19 (top: left and right), at intermediate values of t/L the corrugated plates in a foam-filled core may collapse with the mode of “middle local-buckling”. Different from “sides local-buckling”, a pair of localized plastic hinges formed only in the middle portion of the plate (Figure 14, left). Before the collapse occurred, the corrugated plate (its middle region in particular) behaved approximately as a straight line, with nearly identical equivalent stress in this region. As the strain was increased, a couple of localized plastic hinges were developed close to the middle region where much bending occurred while the remaining parts of the plate rotated around these hinges as rigid rods (Figure 14, middle). Simultaneously, such local-buckling induced abrupt fluctuation of the equivalent stress in the middle region (Figure 14, right). During post-buckling, the equivalent stress in the

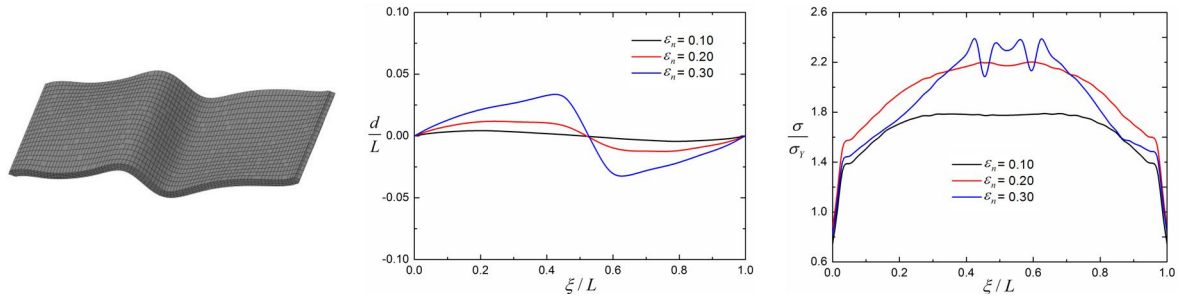


Figure 14. Middle local-buckling: $t/L = 0.02$, $\theta = 65^\circ$, foam I-filled corrugated core.

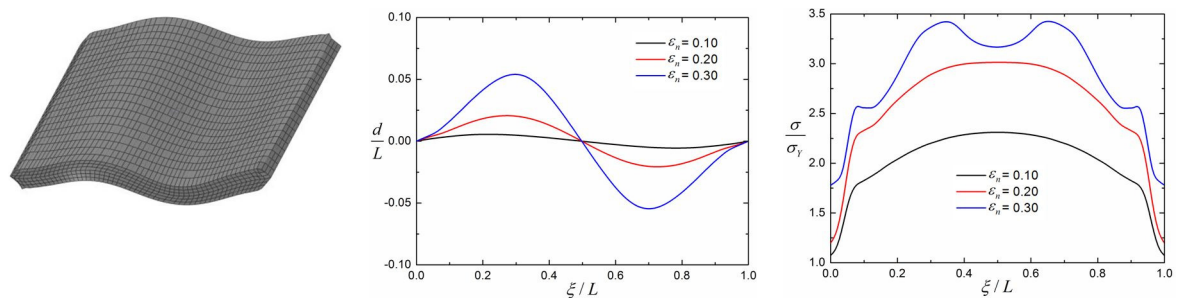


Figure 15. Plastic odd-buckling: $t/L = 0.06$, $\theta = 55^\circ$, foam I-filled corrugated core.

parts of the corrugated plate without plastic hinges even decreased due to relaxation of the compressive stresses (Figure 14, right).

Mode D: plastic odd-buckling. As the values of t/L became larger than those corresponding to mode C (Figure 19, top: left and right), different from the collapse mode of “plastic wrinkling”, a kind of global plastic buckling mode appeared as a single-frequency wave in an odd-symmetrical way; see Figure 15 (left). Whilst the corrugated plate only exhibited a slight bending trend before the collapse, its lateral deflection increased rapidly once buckling occurred; see Figure 15 (middle). Correspondingly, during post-buckling, the fluctuation of the equivalent stress occupied the main region of the plate; see Figure 15 (right). To avoid confusion with the plastic buckling of empty corrugated plates (see immediately below), the plastic buckling mode as characterized above was defined here as *plastic odd-buckling*.

Note that the above four types of collapse mode for foam-filled corrugated plates all occurred at compressive strains significantly larger than those associated with empty ones, consistent with the results presented in the previous section.

Mode E: stable compression. As the value of t/L became sufficiently large, the stubby thick-walled corrugated plates in a foam-filled core did not collapse but rather deform in “stable compression” with continuously plastic hardening (Figure 16, left). Despite of the slight bending due to the strong constraint of the clamped ends, the equivalent stress in the main middle region of the corrugated plate was almost identical throughout the compression process (Figure 16, right). This collapse mode also occurred in the empty cores, as shown in Figure 19 (bottom).

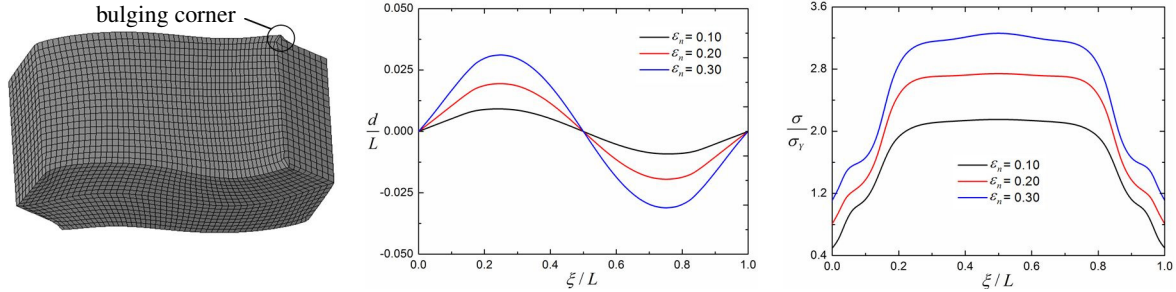


Figure 16. Stable compression: $t/L = 0.20$, $\theta = 45^\circ$, foam I-filled corrugated core.

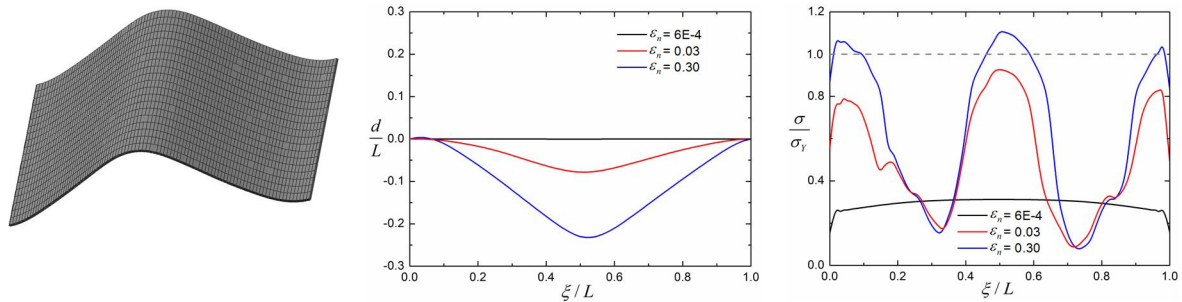


Figure 17. Euler buckling: $t/L = 0.01$, $\theta = 45^\circ$, empty corrugated core.

For the foam-filled cores, four different types of buckling mode had now been identified, including three localized buckling (sides local-buckling, plastic wrinkling and middle local-buckling) and one global buckling (plastic odd-buckling). These collapse modes as illustrated in the left-most parts of Figures 12–15 represented the typical examples marked in Figure 19 where the dominance regime of another collapse mode, stable compression (Figure 16), was also given. Interestingly, the results of Figures 12–16 suggested that the collapse modes of foam-filled cores all exhibited an *odd-symmetry* feature. In contrast, the empty cores collapsed in either elastic or plastic buckling had the common feature of global *even symmetry*, as discussed below.

4.2.2. Collapse modes of empty corrugated core. In addition to stable compression, the present FE simulations revealed that an empty corrugated core could also collapse in two other modes (F and G), defined here as *Euler buckling* and *plastic even buckling*.

Mode F: Euler buckling. For empty cores with small values of t/L (less than 0.018), elastic Euler buckling occurred at small strain levels. As shown in Figure 17, the corrugated plate collapsed with three elastic hinges: one in the middle and the other two near the ends caused by the rotating of the plate. This collapse mode was quite different from that of foam-filled cores, as the constraint provided by filling foam against plate rotation was absent. Moreover, during post-buckling, the elastic hinges became gradually plastic as the strain was increased (Figure 17, right).

Mode G: plastic even-buckling. Different from the mode of plastic odd-buckling in foam-filled cores, an empty core with sufficiently large values of t/L (larger than 0.018) collapsed with plastic buckling in an “even-symmetry” way; see Figure 18 (left). Similar to Euler buckling, three hinges emerged, all

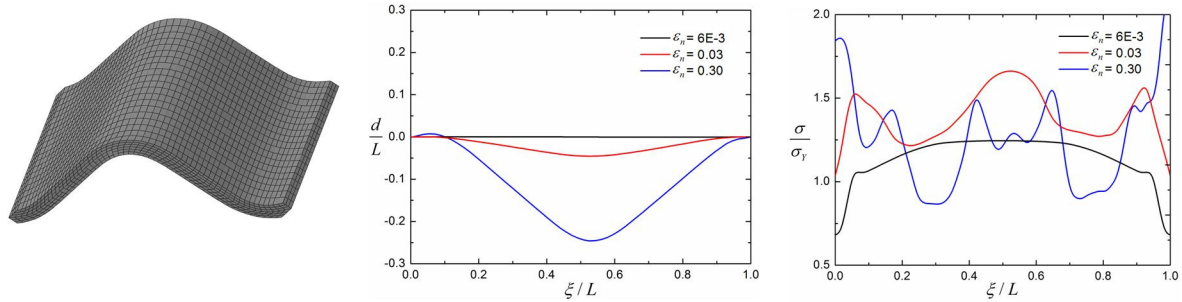


Figure 18. Plastic even-buckling: $t/L = 0.05$, $\theta = 55^\circ$, empty corrugated core.

associated with the equivalent stress exceeding the yield level (Figure 18, right). Unlike the foam-filled cores, within the stage of post-buckling at large compressive strains, the equivalent stress near the two ends of the corrugated plate was larger than that in the center, whether the empty core collapsed with elastic buckling or plastic even-buckling.

It was of interest to notice that, for a thick-walled corrugated plate under large compressive strain, small yet visible corner bulging occurred, as illustrated in Figure 16 (left). The bulging was caused by the material located inside the core (along direction-1) being squeezed out, analogous to the case of a thick-walled short tube under internal or external pressure [Zhu et al. 2013]. Whilst the bulging corner occurred in either foam-filled or empty corrugated cores, the extent of bulging was more serious for the former due to the additional squeezing of the filling foam.

It was seen from Figure 19 (top: left and right) that whilst the collapse modes of corrugated plates filled with either foam I or foam II were more or less similar (yet totally different from the traditional Euler buckling and plastic buckling of empty plates), the regime of dominance of each mode (apart from stable compression) varied considerably as foam I was replaced by foam II. In particular, with foam II insertions, the mode of “sides local-buckling” was absent; see Figure 19 (top right). Further, the regimes of collapse modes for empty cores were nearly independent of the inclination angle θ whereas those of the foam-filled cores were quite sensitive to θ .

4.2.3. Collapse mechanisms. The deformation and collapse of a foam-filled corrugated core may be attributed to the synergetic effects of several factors, including: constraints of foam insertions; nonuniformity of foam constraints; influence of core web slenderness ratio t/L and inclination angle θ . Although different collapse modes were identified for foam-filled cores, the global tendency of the deformation was similar, all exhibiting an odd-symmetry feature. Qualitatively, this may be interpreted as follows. Analogous to the analysis of Yoo et al. [2010] for foam-filled egg-boxes, the difference in densification strain on the two sides of the corrugated plate led to unbalanced forces on either side of the plate, as illustrated in Figure 20 (top left). Only near the center of the plate were the stresses from the foam on either side of the plate expected to be equal. Hence, in contrast to the even-symmetrical bending of empty corrugated plates, there was tendency for the foam insertions to generate a rotational moment, inducing odd-symmetrical (or antisymmetrical) buckling of the plate as shown in Figure 20 (right).

4.3. Strength maps. For both empty and foam-filled corrugated cores, contours of their relative strength σ_p/σ_Y as well as relative density $\bar{\rho}$ were plotted in Figure 21 on a chart with axes of t/L and θ . The

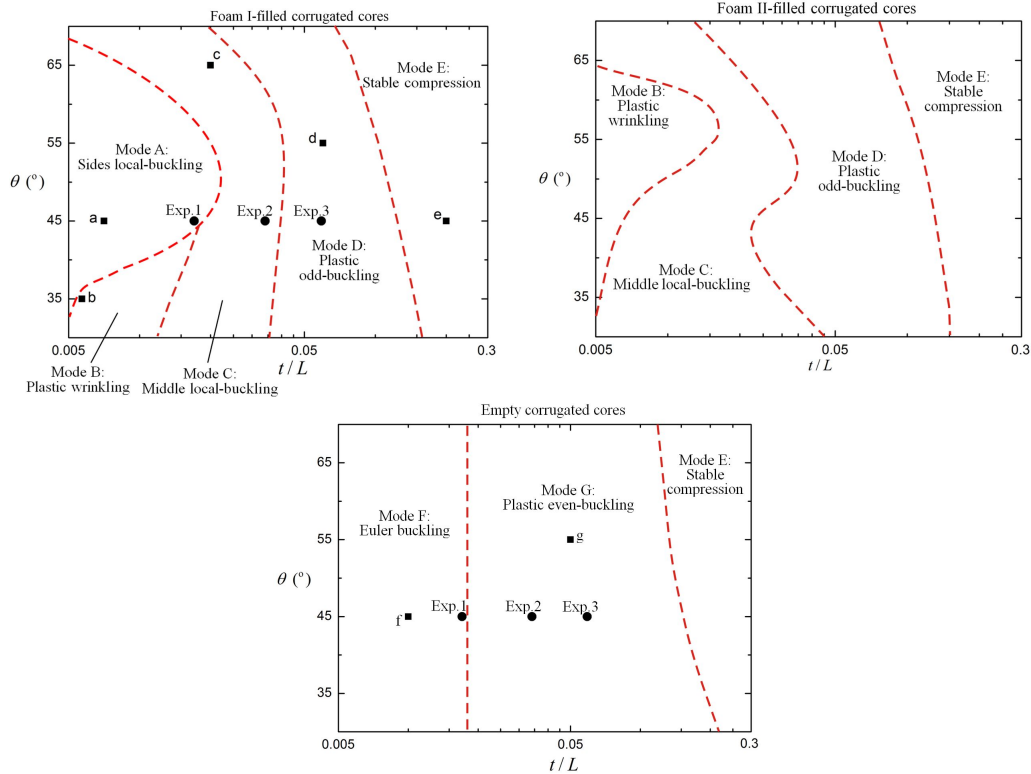


Figure 19. Collapse mechanism map for corrugated plates filled with: foam I (top left); foam II (top right); no foam (bottom). Red dashed lines separated neighboring deformation modes. Experimental data were marked as solid circles at top left and bottom, whilst typical geometries for different deformation modes were marked as solid squares. Boundary between elastic and plastic buckling for empty corrugated plates was constructed using (A.4).

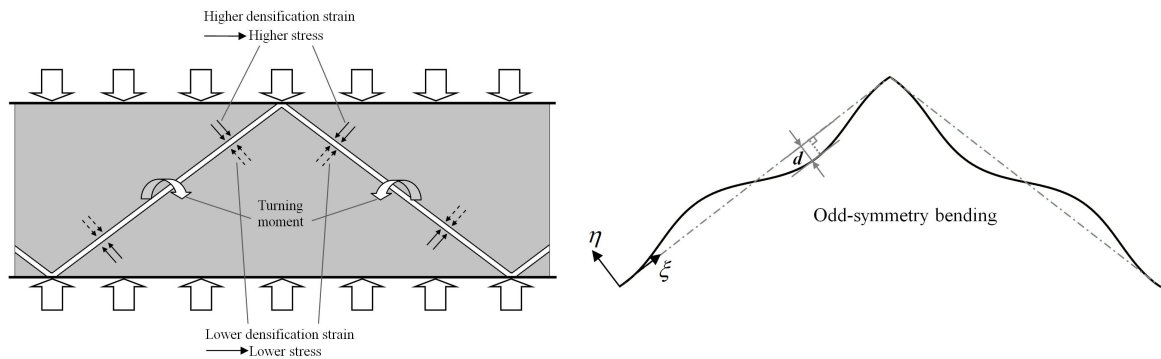


Figure 20. Schematic of global bending deformation of foam-filled corrugated plates under out-of-plane compression. Left: emergence of turning (bending) moment on corrugated plate; right: corresponding global bending deformation of corrugated plate (middle line).

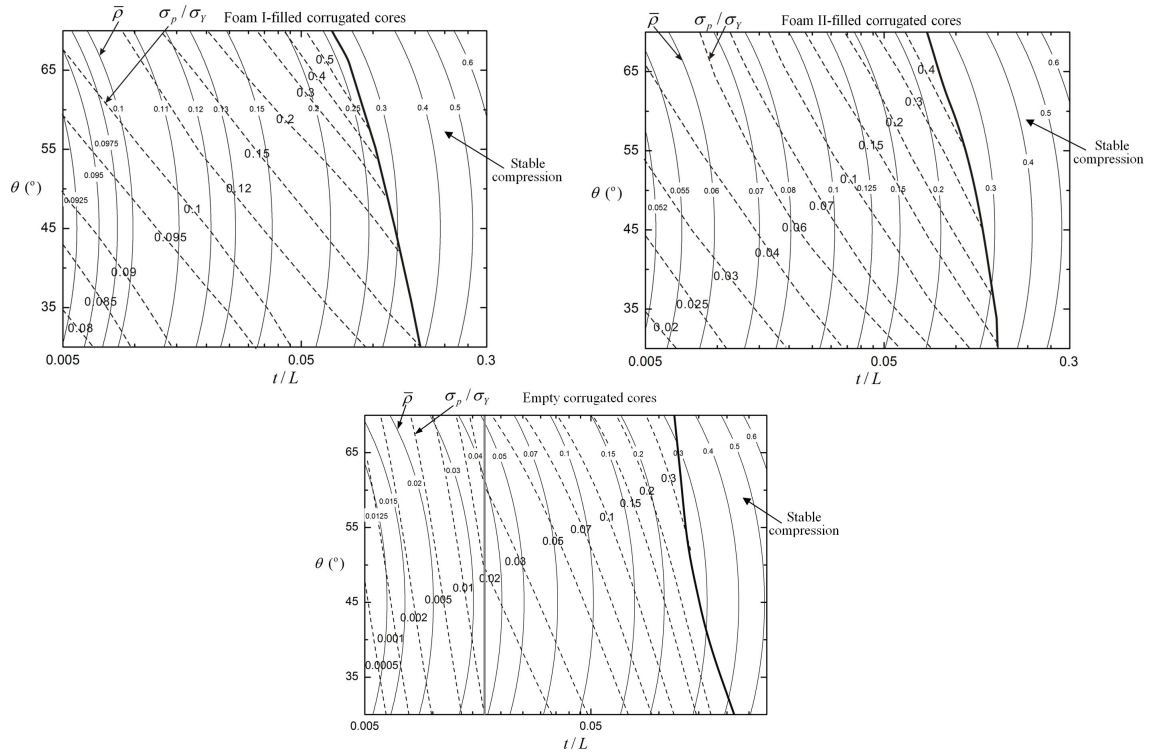


Figure 21. Normalized peak stress (σ_p/σ_Y) and relative density ($\bar{\rho}$) plotted as functions of core web slenderness ratio (t/L) and inclination angle (θ) for corrugated sandwich plates having: foam I-filled core (top left); foam II-filled core (top right); empty core (bottom). Thick solid lines separated the “stable compression” regime from the plastic buckling modes. Solid contours denoted $\bar{\rho}$ and dashed lines denoted σ_p/σ_Y .

thick inclined line on the chart separated the “stable compression” regime which exhibited no peak stress from the buckling regime where the peak stress was clearly defined.

Consider a trajectory of fixed $\bar{\rho}$ for the foam-filled cores. The relative strength σ_p/σ_Y increased monotonously with increasing θ , rather than increasing t/L . Consequently, there existed no clear optimal path of core geometry that gave rise to the peak stress for any given value of $\bar{\rho}$ that maximized the peak stress. This indicated that θ played a more important role than t/L in the compressive response of foam-filled cores. It followed that, for out-of-plane compression, it would be better to design a foam-filled corrugated core with large inclination angle, with θ close to 90 degree being the best choice. In reality, however, it was difficult to fabricate corrugated cores without using platforms when θ was larger than say 70 degree. Further, in addition to out-of-plane compression, the performance of foam-filled cores having large inclination angles subjected to other loading types such as three-point bending and shear needs to be considered.

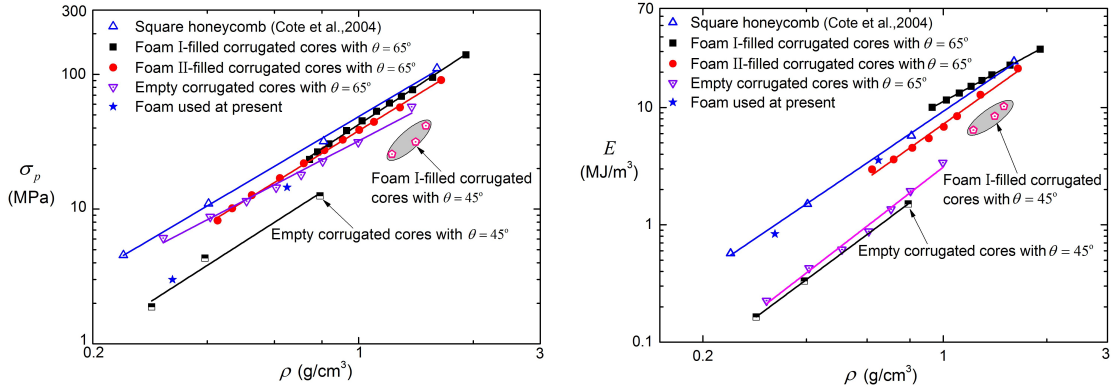


Figure 22. Left: Performance of competing sandwich core topologies under quasistatic compression: peak stress (compressive strength) versus core density; right: energy absorption per unit volume (up to $\epsilon_n = 0.30$) versus core density. Except for the results of square honeycombs from [Côté et al. 2004], all the other data was from the present study.

5. Comparison with competing core topologies

Under out-of-plane compression, the energy absorption capacity of a sandwich core was traditionally defined as the integration of stress with respect to strain from 0 up to 0.50. However, as the present study of different sandwich cores was limited to the nominal compressive strain of $\epsilon_n = 0.30$, for consistency the energy absorption per unit volume was defined as

$$E = \int_0^{0.30} \sigma_n d\epsilon_n. \quad (10)$$

Figure 22 compared separately the compressive strength (peak stress) and energy absorption of foam-filled corrugated cores with several competing core topologies for lightweight sandwich constructions, including close-celled metallic foams, square honeycombs and empty corrugated cores. Both experimental data and FE simulation results were used for the comparison. For foam-filled cores, data for both foam I and foam II insertions were presented. Further, for both empty and foam-filled cores, results for $\theta = 45^\circ$ as well as $\theta = 65^\circ$ were included.

It was seen from Figure 22 (left) that the compressive strength of foam I-filled core with $\theta = 65^\circ$ was almost comparable with that of square honeycombs [Côté et al. 2004], and considerably superior to either metal foams (used in the present study) or empty corrugated cores. Further, for a fixed core density, foam I-filled core with $\theta = 65^\circ$ performed much better than that with $\theta = 45^\circ$, consistent with previous results concerning the effect of inclination angle.

In addition to compressive strength, the energy absorption of foam I-filled sandwich core with $\theta = 65^\circ$ also exceeded that of square honeycombs; see Figure 22 (right). Square honeycombs rapidly softened due to buckling once the peak stress was reached, whilst the softening of foam-filled corrugated cores ($\theta = 65^\circ$) after the peak was less pronounced. In addition, the post-buckling performance was also considerably strengthened by the filling foam relative to the unfilled cores.

6. Conclusions

Detailed physical mechanisms underlying the significant beneficial effects of filling aluminum foams into the interstices of corrugated plates made of 304 stainless steel were exploited by using the finite element method. With the focus placed upon quasistatic out-of-plane compression, the beneficial effects were assessed on the basis of elevated peak stress and energy absorption relative to unfilled corrugated plates of equal mass. The main findings were summarized as follows:

- (1) Good agreement between FE simulated and experimentally measured stress versus strain curves was achieved. The deformation and collapse modes of both the empty and foam-filled corrugated plates were also accurately captured by the FE simulations.
- (2) The post-yielding strength and energy absorption of foam-filled corrugated plates were significantly enhanced relative to empty ones, both exceeding the combined contributions from the corrugated plates and the foam alone, and the advantages increased as the foam became denser.
- (3) The coupling effects of a corrugated plate and the surrounding foam resulted in much delayed and stabilized buckling of the former. With foam support, the corrugated plate experienced noticeable length reduction as axial compression was dominant before the plate collapsed. As the plate began to bend, the foam insertions were strengthened, changing the initial state of uniaxial compressive stressing to the state of complex stressing involving compression, tension and shear. In comparison, in the absence of foam filling, the corrugated plate was dominated by bending deformation (with little length change) and easily collapsed, with a tiny critical strain ranging from 0.002 to 0.004.
- (4) The beneficial effects of foam filling to both the strength and energy absorption was the greatest if the slenderness ratio $t/L \leq 0.02$, when the empty corrugated plates collapsed by elastic Euler buckling. For sufficiently large values of t/L , stable compression with plastic hardening of both the empty and foam-filled corrugated plates occurred so that the strengthening effect of foam filling was gradually lost.
- (5) The inclination angle θ also played an important role in dictating the compressive response of both the empty and foam-filled corrugated plates. For the foam-filled corrugated plates, the specific strength and energy absorption depended primarily upon the inclination angle, with a weak dependence upon the core web slenderness.
- (6) Different from the traditional buckling modes of unfilled plates, a variety of different collapse modes were identified for foam-filled plates, including sides local-buckling, plastic wrinkling, middle local-buckling and plastic odd-buckling. Correspondingly, collapse mechanism maps were constructed.

Besides the out-of-plane compressive response, similar beneficial effects had been established when the foam-filled sandwich plates were subjected to three-point bending and simple shear. The varying role of foam insertion with increasing compression velocity had also been explored. These experimental and theoretical results will be reported in separate studies. In summary, the foam-filled corrugated topology is attractive from the perspectives of strength and energy absorption, holding great potential for heavy-duty structural applications.

Appendix: Analytical formulae for buckling of empty corrugated panels

For empty corrugated panels subjected to uniform out-of-plane compression, plane strain assumption was appropriate. Therefore, $(1 - v^2)$ was introduced to the Young's modulus E_s of the core web material whilst its yielding stress became $2\sigma_Y/\sqrt{3}$. For core webs having small slenderness ratios, an equilibrium analysis indicated the out-of-plane compressive strength may be expressed as

$$\sigma_{p\text{-empty}} = \sigma_c \tan \theta(t/L) \quad (\text{A.1})$$

where σ_c was the maximum axial compressive stress of the core web. For elasto-plastic hardening materials (i.e., stainless steel as considered in the present study), according to the Euler buckling and Shanley plastic bifurcation stresses [Shanley 1947; Côté et al. 2006], σ_c may be obtained as

$$\sigma_c = \begin{cases} \frac{\pi^2 E_s}{12(1-v^2)} \left(\frac{t}{\mu L}\right)^2 & \text{if } \frac{t}{L} < \mu \sqrt{\frac{8\sqrt{3}(1-v^2)\sigma_Y}{\pi^2 E_s}}, \\ \frac{\pi^2 E_t}{12} \left(\frac{t}{\mu L}\right)^2 & \text{otherwise,} \end{cases} \quad (\text{A.2})$$

where the coefficient μ was introduced to correct the effective length of the core web under different end constraints. For the core webs considered here, it was reasonable to take the ends of the core web as built-in constrained, giving $\mu = 0.5$. For elastic perfectly plastic materials, the Equation (A.2) may be simplified to

$$\sigma_c = \begin{cases} \frac{\pi^2 E_s}{12(1-v^2)} \left(\frac{t}{\mu L}\right)^2 & \text{if } \frac{t}{L} < \mu \sqrt{\frac{8\sqrt{3}(1-v^2)\sigma_Y}{\pi^2 E_s}}, \\ \frac{2\sigma_Y}{\sqrt{3}} & \text{otherwise.} \end{cases} \quad (\text{A.3})$$

It followed from Equation (A.2) or (A.3) that the critical slenderness ratio corresponding to the transition from elastic buckling to plastic buckling (or yielding) was

$$\left.\frac{t}{L}\right|_{\text{critical}} = \mu \sqrt{\frac{8\sqrt{3}\sigma_Y(1-v^2)}{\pi^2 E_s}}. \quad (\text{A.4})$$

Acknowledgment

This work was supported by the National Basic Research Program of China (2011CB610305), the National Natural Science Foundation of China (11021202, 11072188 and 11102152), and the National 111 Project of China (B06024).

References

- [Burlayenko and Sadowski 2010] V. N. Burlayenko and T. Sadowski, "Effective elastic properties of foam-filled honeycomb cores of sandwich panels", *Compos. Struct.* **92**:12 (2010), 2890–2900.
- [Calladine and English 1984] C. R. Calladine and R. W. English, "Strain-rate and inertia effects in the collapse of two types of energy-absorbing structure", *Int. J. Mech. Sci.* **26**:11–12 (1984), 689–701.

- [Cartié and Fleck 2003] D. D. Cartié and N. A. Fleck, “The effect of pin reinforcement upon the through-thickness compressive strength of foam-cored sandwich panels: porous materials”, *Compos. Sci. Technol.* **63**:16 (2003), 2401–2409.
- [Côté et al. 2004] F. Côté, V. S. Deshpande, N. A. Fleck, and A. G. Evans, “The out-of-plane compressive behavior of metallic honeycombs”, *Mater. Sci. Eng. A* **380**:1–2 (2004), 272–280.
- [Côté et al. 2006] F. Côté, V. S. Deshpande, N. A. Fleck, and A. G. Evans, “The compressive and shear responses of corrugated and diamond lattice materials”, *Int. J. Solids Struct.* **43**:20 (2006), 6220–6242.
- [Deshpande and Fleck 2000] V. S. Deshpande and N. A. Fleck, “Isotropic constitutive models for metallic foams”, *J. Mech. Phys. Solids* **48**:6–7 (2000), 1253–1283.
- [DSSC 2007] DSSC, *ABAQUS/explicit user’s manual version 6.7*, Providence, Rhode Island, USA, 2007.
- [Hadi 2001] B. K. Hadi, “Wrinkling of sandwich column: comparison between finite element analysis and analytical solutions”, *Compos. Struct.* **53**:4 (2001), 477–482.
- [Kazemahvazi and Zenkert 2009] S. Kazemahvazi and D. Zenkert, “Corrugated all-composite sandwich structures, 1: Modeling”, *Compos. Sci. Technol.* **69**:7–8 (2009), 913–919.
- [Kazemahvazi et al. 2009] S. Kazemahvazi, D. Tanner, and D. Zenkert, “Corrugated all-composite sandwich structures. Part 2: Failure mechanisms and experimental programme”, *Compos. Sci. Technol.* **69**:7–8 (2009), 920–925.
- [Li and Muthyala 2008] G. Li and V. D. Muthyala, “Impact characterization of sandwich structures with an integrated orthogrid stiffened syntactic foam core”, *Compos. Sci. Technol.* **68**:9 (2008), 2078–2084.
- [Liu et al. 2008] T. Liu, Z. C. Deng, and T. J. Lu, “Analytical modeling and finite element simulation of the plastic collapse of sandwich beams with pin-reinforced foam cores”, *Int. J. Solids Struct.* **45**:18–19 (2008), 5127–5151.
- [Mahmoudabadi and Sadighi 2011] M. Z. Mahmoudabadi and M. Sadighi, “A study on the static and dynamic loading of the foam filled metal hexagonal honeycomb — theoretical and experimental”, *Mater. Sci. Eng. A* **530**:0 (2011), 333–343.
- [Mamalis et al. 2008] A. G. Mamalis, D. E. Manolacos, M. B. Ioannidis, K. N. Spentzas, and S. Koutroubakis, “Static axial collapse of foam-filled steel thin-walled rectangular tubes: experimental and numerical simulation”, *Int. J. Crashworthiness* **13**:2 (2008), 117–126.
- [Marasco et al. 2006] A. I. Marasco, D. D. R. Cartié, I. K. Partridge, and A. Rezai, “Mechanical properties balance in novel Z-pinned sandwich panels: out-of-plane properties”, *Compos. A Appl. Sci. Manuf.* **37**:2 (2006), 295–302. CompTest 2004.
- [Nanayakkara et al. 2011] A. Nanayakkara, S. Feih, and A. P. Mouritz, “Experimental analysis of the through-thickness compression properties of z-pinned sandwich composites”, *Compos. A Appl. Sci. Manuf.* **42**:11 (2011), 1673–1680.
- [Nia and Sadeghi 2010] A. A. Nia and M. Z. Sadeghi, “The effects of foam filling on compressive response of hexagonal cell aluminum honeycombs under axial loading-experimental study”, *Mater. Design* **31**:3 (2010), 1216–1230.
- [Ostos et al. 2012] J. B. Ostos, R. G. Rinaldi, C. I. Hammetter, G. D. Stucky, F. W. Zok, and A. J. Jacobsen, “Deformation stabilization of lattice structures via foam addition”, *Acta Mater.* **60**:19 (2012), 6476–6485.
- [Pingle et al. 2011] S. M. Pingle, N. A. Fleck, V. S. Deshpande, and H. N. G. Wadley, “Collapse mechanism maps for a hollow pyramidal lattice”, *Proc. R. Soc. Lond. A* **467**:2128 (2011), 985–1011.
- [Rice et al. 2006] M. C. Rice, C. A. Fleischer, and M. Zupan, “Study on the collapse of pin-reinforced foam sandwich panel cores”, *Exp. Mech.* **46**:2 (2006), 197–204.
- [Shanley 1947] F. R. Shanley, “Inelastic column theory”, *J. Aeronaut. Sci.* **14**:5 (1947), 261–268.
- [Tam and Calladine 1991] L. L. Tam and C. R. Calladine, “Inertia and strain-rate effects in a simple plate-structure under impact loading”, *Int. J. Impact Eng.* **11**:3 (1991), 349–377.
- [Vaziri et al. 2006] A. Vaziri, Z. Xue, and J. W. Hutchinson, “Metal sandwich plates with polymer foam-filled cores”, *J. Mech. Mater. Struct.* **1**:1 (2006), 97–127.
- [Wilbert et al. 2011] A. Wilbert, W.-Y. Jang, S. Kyriakides, and J. F. Floccari, “Buckling and progressive crushing of laterally loaded honeycomb”, *Int. J. Solids Struct.* **48**:5 (2011), 803–816.
- [Yan et al. 2013] L. L. Yan, B. Yu, B. Han, C. Q. Chen, Q. C. Zhang, and T. J. Lu, “Compressive strength and energy absorption of sandwich panels with aluminum foam-filled corrugated cores”, *Compos. Sci. Technol.* **86**:0 (2013), 142–148.
- [Yoo et al. 2010] S. H. Yoo, S. H. Chang, and M. P. F. Sutcliffe, “Compressive characteristics of foam-filled composite egg-box sandwich panels as energy absorbing structures”, *Compos. A Appl. Sci. Manuf.* **41**:3 (2010), 427–434.

[Zhang et al. 2013] J. Zhang, P. Supernak, S. Mueller-Alander, and C. H. Wang, "Improving the bending strength and energy absorption of corrugated sandwich composite structure", *Mater. Design* **52:0** (2013), 767–773.

[Zhu et al. 2013] Y. Zhu, X. Y. Luo, H. M. Wang, R. W. Ogden, and C. Berry, "Three-dimensional non-linear buckling of thick-walled elastic tubes under pressure", *Int. J. Non-Linear Mech.* **48:0** (2013), 1–14.

Received 10 Dec 2013. Revised 28 Mar 2014. Accepted 30 Apr 2014.

BIN HAN: hanbinghost@gmail.com

State Key Laboratory for Strength and Vibration of Mechanical Structures, School of Aerospace, Xi'an Jiaotong University, Xi'an, 710049, China

LEI L. YAN: rayyll@stu.xjtu.edu.cn

State Key Laboratory for Strength and Vibration of Mechanical Structures, School of Aerospace, Xi'an Jiaotong University, Xi'an, 710049, China

BO YU: jo_elnino1987@163.com

State Key Laboratory for Strength and Vibration of Mechanical Structures, School of Aerospace, Xi'an Jiaotong University, Xi'an, 710049, China

QIAN C. ZHANG: zqc111999@mail.xjtu.edu.cn

State Key Laboratory for Strength and Vibration of Mechanical Structures, School of Aerospace, Xi'an Jiaotong University, Xi'an, 710049, China

CHANG Q. CHEN: chencq@tsinghua.edu.cn

Department of Engineering Mechanics, CNMM & AML, Tsinghua University, Beijing, 100084, China

TIAN J. LU: tjlu@mail.xjtu.edu.cn

State Key Laboratory for Strength and Vibration of Mechanical Structures, School of Aerospace, Xi'an Jiaotong University, Xi'an, 710049, China

REPRESENTATIVE VOLUME ELEMENT IN 2D FOR DISKS AND IN 3D FOR BALLS

NATALIA RYLKO

Effective properties of random composites are discussed in the framework of the representative volume element (RVE) theory proposed by Mityushev (2006). This theory is extended to 2D fiber composites with sections perpendicular to fibers of different radii and to 3D composites with spherical inclusions. RVE theory is applied to the mixture problem frequently met in technological processes. This problem consists in a mechanical stir process of few components to get a homogeneous material in macroscale. In particular, the AlSi9/SiC composites obtained by thermomechanical deformation are investigated.

1. Introduction

The effective properties of composites and porous media can be determined by measurement of macroscopic properties of test specimens. Analogous to the measurement, computational methods are used in theoretical investigations of the specimens, which represent the entire material. If inclusions or pores are distributed statistically homogeneously in the bulk material, the effective properties are described by constant tensors [Adler et al. 2012; Gross and Seelig 2011]. The macroscopic tensors do not depend on the size, shape of the chosen specimen or on boundary conditions [Bakhvalov and Panasenko 1989; Jikov et al. 1994]. These tensors can be determined via solution of the periodic problem when the periodicity cell represents the material under consideration. This concerns not only strictly periodic media but also statistically homogeneous media when a cell represents the macroscopic properties of the random media [Golden and Papanicolaou 1983; Jikov et al. 1994; Telega 2004]. Such media constitute a subclass of heterogeneous fields discussed in [Torquato 2002; Mityushev 1999; Mityushev and Rylko 2013] and functionally gradient materials [Jaworska et al. 2006; Rozmus et al. 2009; Gross and Seelig 2011].

Statistically homogeneous media, defined in [Golden and Papanicolaou 1983; Jikov et al. 1994; Telega 2004], can be represented by a cell, which is called the representative volume element (RVE). The homogenization theory justifies existence of the macroscopic tensors for such media. The computational problem consists in numerical and symbolic calculations of the effective tensors when the RVE is given, i.e., the microstructure is deterministically or statistically described. However, only the existence of the RVE follows from the homogenization theory. Therefore, methods to construct RVEs can be considered as the first step to determine the effective properties of composites and porous media.

Statistical methods to construct RVEs have been described in detail in [Benveniste 1987; Gusev 1997; Huet 1990; Kanit et al. 2003; Milton 2002; Ostoja-Starzewski 2008; 2011; Segurado and LLorca 2006; Torquato 2002] and works cited therein. The statistical methods are based on the overall testing process. For instance, for dispersed two-phase composites with equal inclusions, the number of particles contained

MSC2010: 74Q15.

Keywords: representative volume element, effective conductivity, nonoverlapping disks, random inclusions.

in a sample is increased and the effective constants are computed, usually by purely numerical methods [Zohdi and Wriggers 2008]. The process of increasing is stopped when the fluctuations of the effective constants become sufficiently small. The number of particles 64 per cell frequently arises in the literature [ibid.] as a sufficiently large number for the nonoverlapping uniform distribution of inclusions. Analytical and numerical results [Czapla et al. 2012a; 2012b] rigorously confirm this fact.

Purely numerical methods [Zohdi and Wriggers 2008] are restricted to special distributions of inclusions. The properties of constituents are also given numerically. These lacks were overcome in [Mityushev 2006] (hereafter referred to as [M2006]) where a rigorous and constructive theory of the RVE for plane composites with identical circular inclusions was described. The RVE theory for identical disks in that paper is based on the representation of the effective conductivity tensor [Berlyand and Mityushev 2001; Mityushev 2001] in the form of a double series depending on the concentration of inclusions and on “basic elements” which depend only on the locations of the inclusions. These basic elements are written in terms of the Eisenstein series. Coefficients in the double series depend on the physical properties of constituents. Two composites were defined as equivalent if they have the same basic elements. Therefore, the set of the composites with circular identical inclusions was divided into equivalence classes determined only by the geometrical structure of the composite. In each equivalence class, a composite having the minimal size cell is chosen. Following [M2006], this cell is called the representative cell of equivalent composite materials. A constructive algorithm to determine the representative cell for any distribution of inclusions using only pure geometrical parameters was described in [M2006]. Examples presented therein yield fast transformations from cells to the representative cell of small size. This can be used in optimal computations of the macroscopic properties by applications of numerical and analytical methods.

In this paper we discuss the mixture problem, which can be outlined as follows. Take many balls, put them in a vessel and stir. Hence, we have the original and final locations of balls in the vessel. There are various methods of stirring [Kurtyka and Rylko 2013]. The mixture problem consists in determining the time (velocity, energy, etc.) necessary to reach the required mixture. Here, we arrive at the questions of how to measure the macroscopic thermal and mechanical properties of the mixture. It can be done by expensive experiments. The RVE theory yields an effective and simple method, developed in Section 4, to resolve the mixture problem. This method essentially extends the approach of the paper [Kurtyka and Rylko 2013] based on the M -sum.

In the present paper, we extend the RVE theory of [M2006] to 2D polydisperse composites and to 3D monodisperse composites with spherical inclusions. The obtained theoretical results are applied to the porous alumina material (α -Al₂O₃) discussed in [Nowak et al. 2013] and to the mixture problem frequently met in technological processes. It is shown how to construct the RVE size following the theory of [M2006]. Advantages of using this theory are the fast reconstruction method of the RVE and applications to the mixture problem. It is worth noting that the reconstruction of the RVE in [M2006] was based on equations where unknowns were centers of inclusions. However, it is not clear how to investigate polydisperse composites by use of such equations. Our method is based on investigation of the M -sums for various fragments of the large cell. Such a modification is reduced to investigation of one fixed cell instead of the whole class, which reduces computations.

The paper is organized as follows. The 2D RVE theory for disks is developed in Section 2. The 3D RVE theory is described in Section 3 for the nonoverlapping uniformly distributed identical spherical

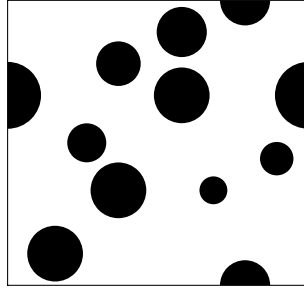


Figure 1. 2D RVE in the torus topology, a section of the 3D RVE parallel to the x_3 -axis.

inclusions. Section 4 is devoted to applications of the RVE theory. Concluding remarks and relations to the RVE theory are presented in Section 5.

2. 2D RVE theory

Following [M2006], we extend the RVE theory to 2D composites with circular inclusions of different radii. Consider a 2D two-component composite made from a collection of nonoverlapping disks embedded in a matrix of a different nature (see Figure 1). It is assumed that the distribution \mathcal{R} of the radii of the disks r_k is given and it does not depend on the locations of the disks. The centers of the disks satisfy a distribution \mathcal{A} corresponding to a nonoverlapping-disks distribution on the plane. The distribution \mathcal{A} formally does not depend on the distribution \mathcal{R} of radii, but the choice of the distribution \mathcal{A} is restricted by \mathcal{R} . This situation can be demonstrated by the following observation: for identical disks of radius r , the distance between any two centers must exceed $2r$.

It is assumed that the distribution \mathcal{A} generates a random homogeneous field [Golden and Papanicolaou 1983; Jikov et al. 1994; Telega 2004] for which the macroscopic properties are correctly defined. One of the most important distributions \mathcal{A} is the nonoverlapping uniform distribution \mathcal{U} , which corresponds to the perfect mixture of inclusions. The distribution \mathcal{U} can be realized by the sequence location method or by random walks described in [Czapla et al. 2012a]. Other distributions are described in the book [Torquato 2002] in terms of the correlation functions. In the present paper, we do not discuss the question of the statistical generation of the theoretical distributions, and assume that realizations of \mathcal{A} are given in the form of pairs (\mathbf{a}_k, r_k) , where $\mathbf{a}_k = (x_k, y_k)$ denotes the center and r_k the radius of the k -th inclusion. Further, it will be convenient to identify \mathbf{a}_k with the complex number $a_k = x_k + iy_k$.

According to the homogenization theory [Golden and Papanicolaou 1983; Jikov et al. 1994; Telega 2004] there exists a periodicity cell with a finite number of inclusions representing the composite. First, we describe parameters of this cell. Consider a lattice \mathcal{Q} on the complex plane \mathbb{C} which is defined by two fundamental translation vectors ω_1 and ω_2 . Without loss of generality we assume that $\omega_1 > 0$ and $\text{Im } \omega_2 > 0$, where Im stands for the imaginary part. Introduce the zeroth cell

$$Q_0 := \left\{ z \in \mathbb{C} : z = t_1\omega_1 + t_2\omega_2, -\frac{1}{2} < t_{1,2} < \frac{1}{2} \right\}.$$

The lattice \mathcal{Q} is generated by the cells $Q_m := \{z \in \mathbb{C} : z - m_1\omega_1 - m_2\omega_2 \in Q_0\}$, where $m = m_1 + im_2$ is a complex number with m_1 and m_2 integers.

Let \mathcal{C}_N denote the set of the elements (a_k, r_k) , $k = 1, 2, \dots, N$, where the radii r_k satisfy the distribution \mathcal{R} and the centers a_k correspond to nonoverlapping uniformly distributed disks in the cell Q_0 . Let $\mathcal{C}_{N+1} = \mathcal{C}_N \cup \{(a_{N+1}, r_{N+1})\}$. Introduce the set $\mathcal{C} = \bigcup_{N=N_0}^{\infty} \mathcal{C}_N$ with sufficiently large N_0 . The number N_0 gives the size of the minimal representative set \mathcal{C}_{N_0} . The set \mathcal{C} consists of all the configurations of mutually disjoint disks uniformly distributed on the plane whose radii satisfy the distribution \mathcal{R} . It is worth noting that \mathcal{C} describes random locations of disks on the plane. In practical measurements, we observe finite fragments of \mathcal{C} . If these fragments represent the considered material, it is possible to statistically recover the distributions \mathcal{R} and \mathcal{A} .

The radii distribution \mathcal{R} can be easily constructed since it describes a 1D random variable. The 2D distribution \mathcal{A} is theoretically described by correlation functions [Torquato 2002]. But we do not follow that reference, and consider \mathcal{A} as a set of the given center coordinates a_k (measured and statistically presented). In particular, the 2D concentration of inclusions ϕ_2 can be measured. Theoretically, the 2D concentration ϕ_2 can be considered as the mean value

$$\phi_2 = \frac{1}{|Q|} \sum_{k=1}^N \pi r_k^2, \quad (2-1)$$

where $|Q|$ stands for the area of the domain Q .

According to the theory [M2006], we have to compare two different representative elements of \mathcal{A} . Consider a large fundamental region Q' constructed from the fundamental translation vectors ω'_1 and ω'_2 . Let Q' contain N' nonoverlapping circular disks D'_k of radius r'_k with centers $a'_k \in Q'$ ($k = 1, 2, \dots, N'$) representing the distributions \mathcal{R} and \mathcal{A} . Let $\widehat{\Lambda}'$ be the effective tensor of the composite represented by the region Q' with inclusions D'_k . Let the cell Q' correspond to another small cell Q which contains inclusions $D_k = \{z \in \mathbb{C} : |z - a_k| < r_k\}$ ($k = 1, \dots, N$) also representing the distributions \mathcal{R} and \mathcal{A} , such that the effective tensor $\widehat{\Lambda}$ is close to $\widehat{\Lambda}'$. Closeness is defined by the concentration accuracy $O(\phi_2^{L+1})$ for the difference $\Delta\widehat{\Lambda} = \widehat{\Lambda} - \widehat{\Lambda}'$, with prescribed L . According to [M2006], the cell Q is a representative cell for the region Q' with the accuracy $O(\phi_2^{L+1})$ if

$$\Delta\widehat{\Lambda} = O(\phi_2^{L+1}). \quad (2-2)$$

Let a representative cell Q have the minimal possible area from all the representative cells equivalent to Q' . This cell is called the RVE. The existence of the RVE is evident since in the worst case one can take $Q = Q'$. The numerical statistical methods [Kanit et al. 2003] are also based on the relation (2-2). Since ϕ_2 is fixed in numerical computations, (2-2) becomes $\Delta\widehat{\Lambda} \approx 0$.

Instead of (2-2), Mityushev proposed to compare the basic elements of the expansion of the effective tensor. These basic elements are introduced as follows. Let a cell Q contain N inclusions with centers a_k . Let $E_m(z)$ denote the Eisenstein function of order m (see for instance Appendix A of [Czapla et al. 2012a]). Let \mathbf{C} denote the operator of complex conjugation, which satisfies $\mathbf{C}^q z = z$ for even q and $\mathbf{C}^q z = \mathbf{C}z = \bar{z}$ for odd q .

The following sums, of multi-order (m_1, \dots, m_q) , were introduced in [M2006]:

$$e_{m_1 \dots m_q} := \left(\frac{\pi}{\phi_2}\right)^{1+\frac{1}{2}(m_1+\dots+m_q)} \sum_{k_0, k_1, \dots, k_q} r_{k_0}^2 r_{k_1}^{2t_1} \dots r_{k_q}^{2t_q} E_{m_1}(a_{k_0} - a_{k_1}) \overline{E_{m_2}(a_{k_1} - a_{k_2})} \dots \times \mathbf{C}^q E_{m_q}(a_{k_{q-1}} - a_{k_q}), \quad (2-3)$$

where $k_s = 1, 2, \dots, N$ for $0 \leq s \leq q$, $t_0 = 1$ and $t_s = m_s - t_{s-1}$. We call (2-3) the M -sum of order (m_1, \dots, m_q) .¹ For instance, the M -sum of order $(2, 2)$ has the form

$$e_{22} := \left(\frac{\pi}{\phi_2}\right)^3 \sum_{k_0, k_1, k_2} r_{k_0}^2 r_{k_1}^2 r_{k_2}^2 E_2(a_{k_0} - a_{k_1}) \overline{E_2(a_{k_1} - a_{k_2})}. \quad (2-4)$$

It is justified in [M2006] that the effective conductivity tensor for 2D composites can be presented in the form of a power series in the total concentration ϕ_2 with coefficients linearly depending on $e_{m_1 \dots m_q}$. An explicit iterative scheme for the coefficients of this series was explicitly presented in [Berlyand and Mityushev 2001; 2005; Mityushev 2001]. Plane elastic stress and strain fields are described by biharmonic functions [Grigolyuk and Filshinsky 1991]. Any harmonic function is biharmonic. Therefore, harmonic functions describe not only conductivity problems but also special elastic stress and strain fields. This implies that the M -sums also describe (perhaps partially) macroscopic properties of elastic composites. We conjecture that this description is complete for the following reason. An iterative scheme analogous to [Berlyand and Mityushev 2001; 2005; Mityushev 2001] for conductivity problems can be extended to 2D elastic problems. Then, a formula for the effective elastic tensor could be deduced. Such a scheme was actually constructed in particular cases for regular structures [Grigolyuk and Filshinsky 1991]. Preliminary results in [ibid.] and [Mityushev 2000] demonstrate that the effective elastic constants linearly depend on the M -sums and, let us say, M^* -sums having the same structure as (2-3), but with the quasi-elliptic functions $E_m^*(z)$ introduced in Appendix 2 of the book [Grigolyuk and Filshinsky 1991] instead of the Eisenstein functions $E_m(z)$. Hence, the effective elastic tensor can be expressed through a linear combinations of the M - and M^* -sums (the form of this linear combination is not known, but it exists). The quasi-elliptic functions $E_m^*(z)$ are expressed via the Eisenstein functions by algebraic equations [ibid.]. Therefore, it is sufficient to consider only the M -sums (2-3) for elastic media.

Not all the M -sums participate in the effective tensor. For instance, the effective conductivity up to $O(\phi_2^5)$ contains eight M -sums: $e_2, e_{22}, e_{33}, e_{222}, e_{44}, e_{322}, e_{223}, e_{2222}$. For macroscopically isotropic composites, $e_2 = \pi$, and many other M -sums are dependent [Mityushev and Rylko 2012]. This reduces the number of basic elements to achieve the accuracy $O(\phi_2^4)$ to the following four M -sums:

$$e_{22}, e_{33}, e_{2222}, e_{44}. \quad (2-5)$$

The M -sum $(2, 2)$ can be calculated by (2-4). Explicit forms of other M -sums (2-5) are given by the following formulae:

$$e_{33} = \left(\frac{\pi}{\phi_2}\right)^4 \sum_{k_0, k_1, k_2} r_{k_0}^2 r_{k_1}^4 r_{k_2}^2 E_3(a_{k_0} - a_{k_1}) \overline{E_3(a_{k_1} - a_{k_2})}, \quad (2-6)$$

$$e_{2222} = \left(\frac{\pi}{\phi_2}\right)^5 \sum_{k_0, k_1, k_2, k_3, k_4} r_{k_0}^2 r_{k_1}^2 r_{k_2}^2 r_{k_3}^2 r_{k_4}^2 E_2(a_{k_0} - a_{k_1}) \overline{E_2(a_{k_1} - a_{k_2})} E_2(a_{k_2} - a_{k_3}) \overline{E_2(a_{k_3} - a_{k_4})}, \quad (2-7)$$

$$e_{44} = \left(\frac{\pi}{\phi_2}\right)^5 \sum_{k_0, k_1, k_2} r_{k_0}^2 r_{k_1}^6 r_{k_2}^2 E_4(a_{k_0} - a_{k_1}) \overline{E_4(a_{k_1} - a_{k_2})}. \quad (2-8)$$

¹ M -sum is short for Mityushev's sum.

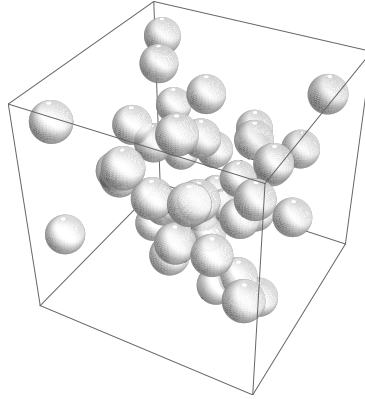


Figure 2. 3D RVE, which can be triply periodically continued to the whole space.

Remark. The M -sums (2-3), in particular (2-5), can be considered as the moments of the correlation functions [Torquato 2002]. Hence, the RVE theory [M2006] implicitly uses the correlation functions and does not require their explicit computations.

3. 3D RVE theory

The 2D M -sums (2-3) can be applied to the 3D RVE by use of the sections method. Consider a 3D cell P with fundamental translation vectors ω_j ($j = 1, 2, 3$). For simplicity, consider the unit cubic cell P , where $\omega_1 = (1, 0, 0)$, $\omega_2 = (0, 1, 0)$ and $\omega_3 = (0, 0, 1)$. Suppose that sufficiently many identical balls (n , say) are uniformly located in P without overlapping (see Figure 2). This distribution corresponds to perfectly mixed balls of the same radius R in a uniform host with prescribed volume concentration

$$\phi = \frac{4\pi n}{3} R^3. \quad (3-1)$$

Consider a typical section of P parallel to the plane generated by ω_1 and ω_2 (see Figure 1). This section can be considered as a plane cell Q_0 with the complex coordinates introduced in Section 2. Let Q_0 contain N disks of radii r_k with centers located at a_k . The concentration of disks in Q_0 has the form

$$\phi_2 = \sum_{k=1}^N \pi r_k^2 \quad (3-2)$$

since Q_0 is the unit square. The uniform nonoverlapping distribution of the identical balls in P yields a uniform nonoverlapping distribution of disks in Q_0 with radii distributed in a special way described by a distribution denoted for definiteness by \mathcal{R}_s . Let r be the random value distributed in accordance with \mathcal{R}_s . It can be described by the uniformly distributed 1D random variable on the segment $(0, R)$. Then the mathematical expectation of the area of a disk is calculated by formula

$$\langle \pi r^2 \rangle = \frac{1}{R} \int_0^R \pi (R^2 - x^2) dx = \frac{2\pi}{3} R^2. \quad (3-3)$$

Let $\langle N \rangle$ denote the expected number of disks in the cell Q_0 . Then (3-2) and (3-3) imply that

$$\frac{\phi_2}{\langle N \rangle} = \left\langle \frac{1}{N} \sum_{k=1}^N \pi r_k^2 \right\rangle = \frac{2\pi}{3} R^2. \quad (3-4)$$

The volume concentration (3-1) is equal to the probability that a point from P belongs to one of the balls. The concentration (3-2) is equal to the probability that a point from Q_0 belongs to one of the disks. The balls are uniformly distributed in P . Moreover, Q_0 is a typical section of P , hence the 2D and 3D concentrations coincide:

$$\phi_2 = \phi. \quad (3-5)$$

Then (3-4) and (3-1) yield

$$\langle N \rangle = 2Rn. \quad (3-6)$$

This formula relates the expected number $\langle N \rangle$ of disks in the cell Q_0 with the given number n of balls per cell.

The expected values of (2-4), (2-6)–(2-8) are calculated by use of (3-3)–(3-4) as

$$\langle e_{m_1 \dots m_q} \rangle = q_{m_1 \dots m_q}, \quad (3-7)$$

where

$$q_{m_1 \dots m_q} := \frac{1}{\langle N \rangle^{1 + \frac{1}{2}(m_1 + \dots + m_q)}} \sum_{k_0 k_1 \dots k_q} E_{m_1}(a_{k_0} - a_{k_1}) \overline{E_{m_2}(a_{k_1} - a_{k_2})} \dots \mathbf{C}^q E_{m_q}(a_{k_{q-1}} - a_{k_q}). \quad (3-8)$$

The M -sums (3-8) correspond to the distribution of the identical disks when the centers a_k obey the uniform nonoverlapping distribution \mathcal{U}_s consistent with the special radii distribution \mathcal{R}_s . The relation (3-7) contains the mathematical expectation $\langle e_{m_1 \dots m_q} \rangle$ over the radii distribution \mathcal{R}_s . We now write the mathematical expectation of (3-7) over the distribution \mathcal{A}_s of centers in the form

$$\langle\langle e_{m_1 \dots m_q} \rangle\rangle = \langle\langle q_{m_1 \dots m_q} f \rangle\rangle. \quad (3-9)$$

It is difficult to calculate analytically the operator $\langle\langle \cdot \rangle\rangle$ because the distribution \mathcal{A}_s has a complicated support domain for the centers of nonoverlapping disks. However, numerical statistical estimations of $\langle\langle q_{m_1 \dots m_q} \rangle\rangle$ can be performed by algorithms developed in [Czapla et al. 2012a; 2012b]. Consider the M -sums (2-5) to estimate the RVE with the accuracy $O(\phi^4)$. It was proved in [Mityushev and Rylko 2012] that

$$q_{ppp} = \frac{(-1)^p}{\langle N \rangle^{p+1}} \sum_{m=1}^{\langle N \rangle} \left| \sum_{k=1}^{\langle N \rangle} E_p(a_m - a_k) \right|^2, \quad p = 2, 3, 4, \quad (3-10)$$

and

$$q_{2222} = \frac{1}{\langle N \rangle} \sum_{k=1}^{\langle N \rangle} \left| \frac{1}{\langle N \rangle^2} \sum_{k_1, k_2} E_2(a_k - a_{k_1}) \overline{E_2(a_{k_1} - a_{k_2})} \right|^2. \quad (3-11)$$

This implies that $q^{(1)} = q_{22}$, $q^{(2)} = -q_{33}$, $q^{(3)} = q_{44}$ and $q^{(4)} = q_{2222}$ are nonnegative for any location of a_k . It was justified in [Berlyand and Mityushev 2005; Berlyand et al. 2013] that, in the framework of the shaking model, the $q^{(j)}$ ($j = 1, 2, 3, 4$) decrease when order (regularity) of the center locations increases. It is conjectured that the decrease principle for ordered structures takes place in the general case. Consider the degenerate plane radii distribution \mathcal{R}_R in which all the radii are equal to R . This distribution

yields the plane uniform nonoverlapping distribution \mathcal{U}_R of the identical disks. The probabilistic space of events described by \mathcal{U}_s is wider than that described by \mathcal{U}_R . Hence, \mathcal{U}_R is “more regular” than \mathcal{U}_s . This yields the inequality $q^{(j)}(\mathcal{U}_R) \leq q^{(j)}(\mathcal{U}_s)$. For moderate concentrations, one can expect that

$$q^{(j)}(\mathcal{U}_R) \approx q^{(j)}(\mathcal{U}_s), \quad j = 1, 2, 3, 4. \quad (3-12)$$

4. Applications

In this section, various applications of the RVE theory are demonstrated. Section 4 is devoted to the size problem of the RVE. It is a traditional problem of the RVE which can be easily solved by simple and fast computations based on the M -sums. Sections 4–4 concern investigations of the structure of the special composites.

Example 1: size of the RVE. We consider a polydisperse random “shaking” composite [Berlyand and Mityushev 2001; 2005]. Let the periodic square array be perturbed by random deviations of the disks. Consider the model as displayed in Figure 3. The doubly periodic unit cell $Q_0 = (-0.5, 0.5) \times (-0.5, 0.5)$ contains 900 disks of radii between 0.0045 and 0.0135, displaced from their position in a regular array by the distance d , taken for each disk as a random variable uniformly distributed on the interval $(0, 0.006)$. Following the RVE theory [M2006], we have to restrict the infinite set of M -sums $\{e_2, e_{22}, e_{33}, e_{2222}, \dots\}$. For definiteness, take the set $\{e_2, e_{22}\}$. Now, let the unit cell Q_0 be cut to the cells $Q_c = (-0.5c, 0.5c) \times (-0.5c, 0.5c)$, where $0 \leq c \leq 1$. New M -sums $\{e_2(c), e_{22}(c)\}$ with reduced numbers of disks $N(c)$ are calculated (after necessary normalization to the unit cell) and presented in Figures 4 and 5. Here, the parameter c is omitted and dependencies of the M -sums on the number of inclusions per cell are shown.

Theoretically, $e_2 = \pi \approx 3.14159$. Hence, the imaginary part $\frac{1}{\pi} \text{Im } e_2$ can be considered as a measure of accuracy. For instance, if the precision 1% is chosen, it is sufficient to take 100 inclusions per cell. The presented computations were performed in about 40 seconds on a standard computer. The results of the computations are given in Table 1.

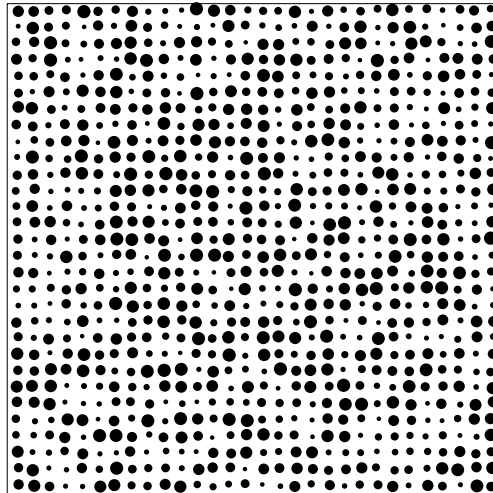


Figure 3. Shaking array of disks.

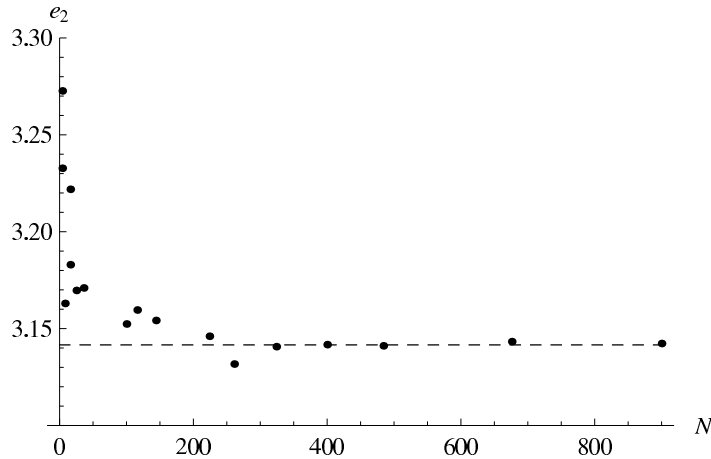


Figure 4. Plot of e_2 against N , the number of disks in the corresponding cut cell.

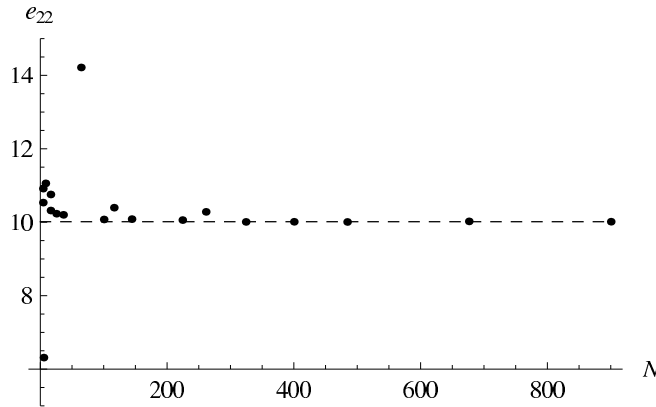


Figure 5. Plot of e_{22} against N .

It is worth noting that representation of the shaking geometries (and any other random geometry) by one inclusion per cell gives the worst possible approximation of the effective properties, since the effective conductivity of the periodic regular structure attains extremal values in locally disturbed composites with a fixed concentration [Berlyand and Mityushev 2001; 2005].

N	4	5	8	16	25	36	64	100
$\text{Re } e_2$	3.27	1.59	3.16	3.61	3.17	3.171	3.40	3.15
$\text{Im } e_2$	0.122	0.461	-0.00165	0.294	0.0172	0.01	0.061	-0.001
e_{22}	10.915	6.314	11.059	10.319	10.232	10.202	14.214	10.075
N	224	261	324	400	484	676	900	
$\text{Re } e_2$	3.1461	3.1317	3.1407	3.1417	3.1411	3.1433	3.1423	
$\text{Im } e_2$	0.0066	0.006	0.00264	-0.0013	0.000755	0.00204	0.00165	
e_{22}	10.0587	10.2828	10.0092	10.0123	10.0075	10.023	10.014	

Table 1. M -sums computed for the shaking geometry; N is the number of inclusions per cell.

concentration	0.05	0.1	0.2	0.45	0.7
q_{22}	54.462	30.334	18.195	11.525	10.056
q_{33}	-382.333	-94.686	-23.367	-3.506	-0.408
q_{44}	4190.05	554.766	77.573	7.988	1.094
q_{2222}	9643.33	2135.82	575.241	161.135	103.932

Table 2. Theoretical M -sums for the distribution \mathcal{U}_R .

q_2^*	$3.195 + 1.473i$
q_{22}^*	39.1971
q_{33}^*	-282.112
q_{44}^*	2127.11
q_{2222}^*	3527.98

Table 3. M -sums computed for data from [Kurtyka and Rylko 2013].

Example 2. The uniform distribution \mathcal{U}_R has been studied extensively, in particular, the expectations $q^{(j)}$ were computed [Czapla et al. 2012a; 2012b]. The results are gathered in Table 2. The composite material F3K.10S reinforced with SiC particles with concentration 0.1 was discussed in [Kurtyka and Rylko 2013]. This composite was obtained by a process of thermomechanical deformation (FSP), which can be considered as a stir method. The results of measurement and computations are presented in Table 3.

First of all, we have to note that the theoretical value $q_2 = \pi \approx 3.14159$ [Czapla et al. 2012a] differs from the measured data $q_2^* = 3.195 + 1.473i$, which demonstrates anisotropy of the experimental sample. This means that SiC particles were not well stirred in the host. The coefficient of anisotropy introduced in [Mityushev 2001] can be used to measure anisotropy of composites. Let us compare now the theoretical $q^{(j)}$ and experimental results $q^{(j)*}$ for high-order M -sums with the fixed concentration 0.1 (bold numbers in the tables). One can see that the $|q^{(j)*}|$ exceed the corresponding values $|q^{(j)}|$. This follows from the initial compact location of the inclusions, because smaller distances $|a_k - a_m|$ between the centers yield larger values of the Eisenstein functions $|E_p(a_k - a_m)|$, hence larger values of the M -sums. Therefore, comparison of the values from Tables 2 and 3 demonstrates that SiC particles are not sufficiently well stirred during the FSP process. Besides the macroscopic anisotropy confirmed by $q_2^* = 3.195 + 1.473i$, other values $q^{(j)*}$ of the M -sums also confirm that the final mixture is not sufficiently well stirred.

Example 3. In the present section, the structure of the Al_2O_3 composite from [Nowak et al. 2013] (see Figure 1 in that paper) is investigated. The 2D concentration of inclusions is equal to 0.52 (3D porosity 0.84 in [ibid.] gives another volume characteristic of the considered composite).

The comparison of the results in Tables 2 and 4 demonstrates the inverse situation to Example 2. First, the value q_2^* is approximately equal to π . The data from Table 4 are similar to the data from the column of Table 2 corresponding to the concentration 0.45. This implies that the “gelcasting of foams” manufacturing method [Nowak et al. 2013] yields isotropic and homogeneous structures similar to the theoretical uniform nonoverlapping distribution.

q_2^*	$3.126 + 0.06118i$
q_{22}^*	11.7983
q_{33}^*	-5.0835
q_{44}^*	9.61203
q_{2222}^*	163.672

Table 4. M -sums computed for digitized data obtained from Figure 1 of [Nowak et al. 2013].

5. Conclusion

In the present paper, we extend the RVE theory of [M2006] to 2D polydisperse composites and to 3D monodisperse composites with spherical inclusions and apply it to the mixture problem. The considered example refers to Al_2O_3 composites obtained by gelcasting of foams and to F3K.10S samples reinforced with SiC particles obtained by FSP.

The developed method gives a simple procedure to construct a typical RVE whose existence is predicted by the homogenization theory. Further, the effective constants can be computed by numerical methods.

The presented methodology can be applied to arbitrary dispersed composites. In the present paper, we consider balls uniformly distributed in host material. This follows from the restriction that we have at our disposal only those theoretical M -sums computed in [Czapla et al. 2012a; 2012b]. Other distributions can be investigated by simulations described in these papers.

Acknowledgement

I am grateful to Professor Barbara Gambin (Warsaw) for useful references.

References

[Adler et al. 2012] P. M. Adler, J. F. Thovert, and V. V. Mourzenko, *Fractured porous media*, Oxford University Press, Oxford, 2012.

[Bakhvalov and Panasenko 1989] N. Bakhvalov and G. Panasenko, *Homogenisation: Averaging processes in periodic media*, Mathematics and its Applications (Soviet Series) **36**, Kluwer, Dordrecht, 1989.

[Benveniste 1987] Y. Benveniste, “A new approach to the application of Mori–Tanaka’s theory in composite materials”, *Mech. Mater.* **6**:2 (1987), 147–157.

[Berlyand and Mityushev 2001] L. Berlyand and V. Mityushev, “Generalized Clausius–Mossotti formula for random composite with circular fibers”, *J. Stat. Phys.* **102**:1-2 (2001), 115–145.

[Berlyand and Mityushev 2005] L. Berlyand and V. Mityushev, “Increase and decrease of the effective conductivity of two phase composites due to polydispersity”, *J. Stat. Phys.* **118**:3-4 (2005), 481–509.

[Berlyand et al. 2013] L. Berlyand, A. G. Kolpakov, and A. Novikov, *Introduction to the network approximation method for materials modeling*, Encyclopedia of Mathematics and its Applications **148**, Cambridge University Press, 2013.

[Czapla et al. 2012a] R. Czapla, W. Nawalaniec, and V. Mityushev, “Effective conductivity of random two-dimensional composites with circular non-overlapping inclusions”, *Comput. Mater. Sci.* **63** (2012), 118–126.

[Czapla et al. 2012b] R. Czapla, W. Nawalaniec, and V. Mityushev, “Simulation of representative volume elements for random 2D composites with circular non-overlapping inclusions”, *Theor. Appl. Inform.* **24**:3 (2012), 227–242.

[Golden and Papanicolaou 1983] K. Golden and G. Papanicolaou, “Bounds for effective parameters of heterogeneous media by analytic continuation”, *Commun. Math. Phys.* **90**:4 (1983), 473–491.

- [Grigolyuk and Filshinsky 1991] E. Grigolyuk and L. Filshinsky, *Periodical piece-homogeneous elastic structures*, Nauka, Moscow, 1991. In Russian.
- [Gross and Seelig 2011] D. Gross and T. Seelig, *Fracture mechanics: With an introduction to micromechanics*, 2nd ed., Springer, Berlin, 2011.
- [Gusev 1997] A. A. Gusev, “Representative volume element size for elastic composites: A numerical study”, *J. Mech. Phys. Solids* **45**:9 (1997), 1449–1459.
- [Huet 1990] C. Huet, “Application of variational concepts to size effects in elastic heterogeneous bodies”, *J. Mech. Phys. Solids* **38**:6 (1990), 813–841.
- [Jaworska et al. 2006] L. Jaworska, M. Rozmus, B. Krolicka, and A. Twardowska, “Functionally graded cermets”, *JAMME* **17**:1-2 (2006), 73–76.
- [Jikov et al. 1994] V. V. Jikov, S. M. Kozlov, and O. A. Oleĭnik, *Homogenization of differential operators and integral functionals*, Springer, Berlin, 1994.
- [Kanit et al. 2003] T. Kanit, S. Forest, I. Galliet, V. Mounoury, and D. Jeulin, “Determination of the size of the representative volume element for random composites: Statistical and numerical approach”, *Int. J. Solids Struct.* **40**:13-14 (2003), 3647–3679.
- [Kurtyka and Rylko 2013] P. Kurtyka and N. Rylko, “Structure analysis of the modified cast metal matrix composites by use of the RVE theory”, *Arch. Metall. Mater.* **58**:2 (2013), 357–360.
- [Milton 2002] G. W. Milton, *The theory of composites*, Cambridge Monographs on Applied and Computational Mathematics **6**, Cambridge University Press, 2002.
- [Mityushev 1999] V. Mityushev, “Transport properties of two-dimensional composite materials with circular inclusions”, *Phil. Trans. R. Soc. A* **455**:1987 (1999), 2513–2528.
- [Mityushev 2000] V. Mityushev, “Thermoelastic plane problem for material with circular inclusions”, *Arch. Mech.* **52**:6 (2000), 915–932.
- [Mityushev 2001] V. Mityushev, “Transport properties of doubly periodic arrays of circular cylinders and optimal design problems”, *Appl. Math. Optim.* **44**:1 (2001), 17–31.
- [Mityushev 2006] V. Mityushev, “Representative cell in mechanics of composites and generalized Eisenstein–Rayleigh sums”, *Complex Var. Elliptic Equ.* **51**:8-11 (2006), 1033–1045.
- [Mityushev and Rylko 2012] V. Mityushev and N. Rylko, “Optimal distribution of the nonoverlapping conducting disks”, *Multiscale Model. Simul.* **10**:1 (2012), 180–190.
- [Mityushev and Rylko 2013] V. Mityushev and N. Rylko, “Maxwell’s approach to effective conductivity and its limitations”, *Quart. J. Mech. Appl. Math.* **66**:2 (2013), 241–251.
- [Nowak et al. 2013] M. Nowak, Z. Nowak, R. B. Pecherski, M. Potoczek, and R. E. Sliwa, “On the reconstruction method of ceramic foam structure and the methodology of Young modulus determination”, *Arch. Metall. Mater.* **58**:4 (2013), 1219–1222.
- [Ostoja-Starzewski 2008] M. Ostoja-Starzewski, *Microstructural randomness and scaling in mechanics of materials: Modern Mechanics and Mathematics*, Chapman & Hall/CRC, Boca Raton, FL, 2008.
- [Ostoja-Starzewski 2011] M. Ostoja-Starzewski, “Stochastic finite elements: Where is the physics?”, *Theor. Appl. Mech.* **38**:4 (2011), 379–396.
- [Rozmus et al. 2009] M. Rozmus, L. Jaworska, B. Krolicka, and P. Putyra, “Gradient microstructure of PCD composites assigned for cutting tools”, *Ceram. Mater.* **61**:3 (2009), 192–196. In Polish.
- [Segurado and LLorca 2006] J. Segurado and J. LLorca, “Computational micromechanics of composites: The effect of particle spatial distribution”, *Mech. Mater.* **38**:8-10 (2006), 873–883.
- [Telega 2004] J. J. Telega, “Stochastic homogenization: Convexity and nonconvexity”, pp. 305–347 in *Nonlinear homogenization and its applications to composites, polycrystals and smart materials*, edited by P. Ponte Castañeda et al., NATO Sci. Ser. II Math. Phys. Chem. **170**, Kluwer, Dordrecht, 2004.
- [Torquato 2002] S. Torquato, *Random heterogeneous materials*, Interdisciplinary Applied Mathematics: Microstructure and macroscopic properties **16**, Springer, New York, 2002.

[Zohdi and Wriggers 2008] T. I. Zohdi and P. Wriggers, *An introduction to computational micromechanics*, Lecture Notes in Applied and Computational Mechanics **20**, Springer, Berlin, 2008.

Received 17 Jan 2014. Revised 17 May 2014. Accepted 13 Jun 2014.

NATALIA RYLKO: nrylko@up.krakow.pl

Institute of Technology, Pedagogical University, ul. Podchorążych 2, 30-084 Krakow, Poland

SMALL AMPLITUDE ELASTIC BUCKLING OF A BEAM UNDER MONOTONIC AXIAL LOADING, WITH FRICTIONLESS CONTACT AGAINST MOVABLE RIGID SURFACES

FRANCESCO GENNA AND GUIDO BREGOLI

The elastic buckling of planar beams in the presence of frictionless unilateral contact against rigid surfaces is reconsidered, taking also into account a possible elastic translation of the rigid surfaces with respect to each other. Exclusive reference is made to the case of small amplitude deflections, such as it is expected to occur in the engineering application of buckling-restrained braces, where the gap between the brace itself and the external containment structure is normally extremely small. Even though this case precludes the occurrence of several deformed shapes possible for the general case of large displacement (to be treated like Euler's elastica), already described in the literature, a significant variety of behaviors is still possible. Only monotonic loading is considered. The main variables under investigation are (i) the wavelength of the buckled beam for a given value of the axial shortening and (ii) the total thrust exerted by the buckled beam against the rigid constraints. It is found that both variables can assume several possible values under the same load; in some cases, their values can be bounded analytically. It appears that, even in the extremely simplified case considered here, the actual behavior is dominated by the existing imperfections, both mechanical and geometrical, thus being quite difficult to be predicted with accuracy.

1. Introduction

The work herein described concerns the post-buckling analysis of a compressed elastic beam placed between two rigid surfaces, that create a frictionless unilateral constraint to the deflection amplitude. The work done so far, which seems to have started with [Villaggio 1979], approaches this problem in a general framework, i.e., for arbitrarily large displacements, in terms of Euler's equations for the so-called elastica. In few instances, such as [Chai 1998], a detailed analysis is developed also for the special case of small amplitude, i.e., exploiting a second-order theory. In the work published so far the main goal was to follow the evolution of the first waves of the deformed shape, once in contact against the external rigid surfaces; a remarkable variety of configurations was found to be possible.

In the present work, the attention is focused only on the case of small amplitudes. The motivation for this analysis is the determination of the buckled configuration of the core plate of a steel buckled-restrained brace (BRB)¹ for a given axial shortening displacement, as well as of the thrust exerted by the buckled core against the external confinement profiles. In this situation, the usually small gap left

Work done within a research project financed by the Italian Ministry of University and Research (MIUR).

Keywords: elastic buckling, unilateral contact.

¹ A steel-bolted BRB is an innovative type of brace, designed to dissipate energy, upon horizontal loading such as wind- or earthquake-induced, both in tension and in compression. It is made of a steel plate enclosed into two bolted steel struts that act as a retaining case, with an internal empty gap.

between the facing surfaces of the inner core of the BRB and the external containment guarantees for small amplitude buckling, so that an analysis developed in a second-order theory is fully adequate. At the same time, this analysis eliminates from the picture a significant portion of the complexity inherent into the elastica solutions, thus allowing some closed-form solutions.

The real case of the BRBs involves, of course, friction and plastic dissipation. Nevertheless, in order to obtain first indications about both the number of waves formed by the buckled core for a prescribed axial shortening, and about the lateral thrust, it appears useful to start the analysis from the simplest possible case, i.e., the one schematically illustrated in Figure 1: linear elastic material; frictionless unilateral contact between core and containment profiles; containment treated as a rigid surface.

The post-buckling deformed shape is here assumed to have a small amplitude, since the gap s between core and rigid constraints is always assumed to be very small. As a consequence, the average axial strain is given only by the axial deformation, with no contribution given by the post-buckling bending. This is true as long as the wavelength does not become extremely short, a circumstance that here is ruled out, limiting the interest to engineering situations for which the average axial shortening strain of the buckled core is of the order of 0.01.

In the present work, no attempt is made at dealing with cyclic loading, which seems to cause a very strange inelastic behavior, according to [Chai 1998], even in the presence of a fully conservative situation. This aspect alone deserves a separate analysis, for which there is no space here.

The rigid constraints are not assumed to be fully fixed to the reference system, and are thus unable to transmit reaction forces to it. In an attempt at describing the real arrangement of BRBs, the two rigid surfaces are connected to each other by an elastic spring, whose stiffness can range from any finite value up to infinity. In this situation, the rigid surfaces can only translate following the internal core thrusts, so that the lateral thrust at one side of the core must equal the one at the opposite side. This is an essential difference with respect to all the previous work published on this topic.

The main goal is to obtain in a direct way, given a value Δ of the axial shortening displacement, (i) the number of buckled waves, (ii) the associated axial force and (iii) the total lateral thrust. It is worth repeating that in all the previous analyses these were never the main points of interest. [Chai 1998] illustrates how to follow the evolution of the post-buckling configuration, but it does not provide an indication of how to calculate directly the quantities of engineering interest.

Other works [Domokos et al. 1997; Holmes et al. 1999; Tzaros and Mistakidis 2011; Alart and Pagano 2002; Pocheau and Roman 2004] consider essentially the elastica problem, and are focused to either mathematical or computational aspects. More work has been devoted to the case of plates [Muradova and Stavroulakis 2007; Chai 2001; 2002; Roman and Pocheau 2002], but never with an engineering-oriented viewpoint. In all cases, the interest has mainly been on following the evolution of the first few waves, a problem quite difficult in itself, but of little engineering interest, for instance in view of the inevitable—and uncontrollable—effect of the existing imperfections.

In the approach illustrated in the present work, two main methodological contributions could be pointed out, both potentially useful to give an answer to the problem of calculating directly the engineering quantities of interest.

A first one is the adoption of the total potential energy as a tool to identify, when necessary and when possible, the number of buckled waves. This technique was already adopted in [Genna and Gelfi 2012b], but in a more restricted framework.

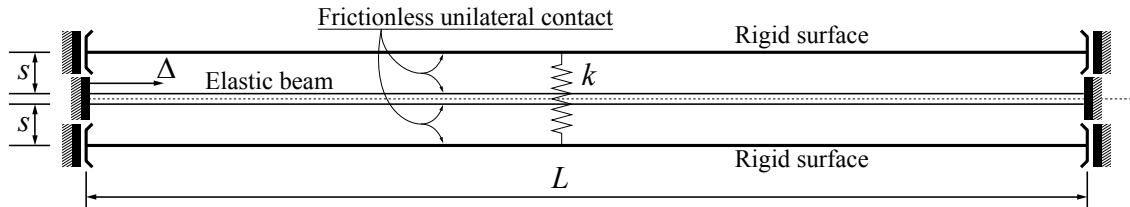


Figure 1. Geometry of the problem under consideration.

A second idea is to choose the buckled wavelength as the main unknown, instead of the number of waves as done previously (for instance, in [Chai 1998]). The number of waves is an integer number that depends on all the geometrical and material data of the problem, whereas the wavelength turns out to be governed by a parameter much easier to be computed, and independent of the total length of the beam. In the case of an infinitely rigid connection spring, such a parameter can take values in a reasonably restricted set.

Since the application envisaged here concerns the post-buckling behavior of BRBs, it is deemed important, upon examination of both numerical and experimental results [Bregoli 2014; Genna and Gelfi 2012a; 2012b; Gelfi and Metelli 2007], to take into account post-buckling shapes not previously considered in the available literature, i.e., for instance, nonsymmetric ones, with point contact at one side of the beam and line contact at the other. Even though the restriction to the small-amplitude case prevents the much wider range of shapes allowed by the elastica case, a significant potential complexity can still be shown, that requires attention.

The analysis illustrated in the sequel will consider initially the general case of an elastic spring connecting the two rigid surfaces. For the special case of a rigid connection, some closed-form results are obtained; the conflicting effects of the elasticity of the constraint will be shown.

2. Analysis of the problem

The geometry of Figure 1 is considered, which refers to rigid surfaces that can only translate according to the force generated into the connecting elastic spring by the thrust of the buckled core.

Although equilibrium is imposed on the deformed configuration, both displacements and strains are assumed to be infinitesimal (i.e., second-order approximation); shear strain contributions are neglected.

It is assumed, for simplicity, that any existing imperfection amplifies the first eigenvector of the elastic beam. Were this not the case, the initial transient phase, after first buckling of the core, might be considerably different from what described in the following, even though, eventually, some clearly defined state, among those illustrated next, should be reached anyway.

The buckled deformed shape is assumed to be periodic along the beam length. This assumption entails some difficulties. The first one concerns the initial transient stage, which is dominated by the imperfections and is hardly periodic in any real situation. When the number of waves increases, the configuration tends to be slightly less sensitive to imperfections, and to become more and more periodic, although never exactly so. If everything were perfect and periodic, each wave would buckle and form a new wave at the same time, thus causing an instantaneous multiplication of the wave number. On the contrary, as also observed in [Chai 1998], in experiments, but also in numerical simulations that

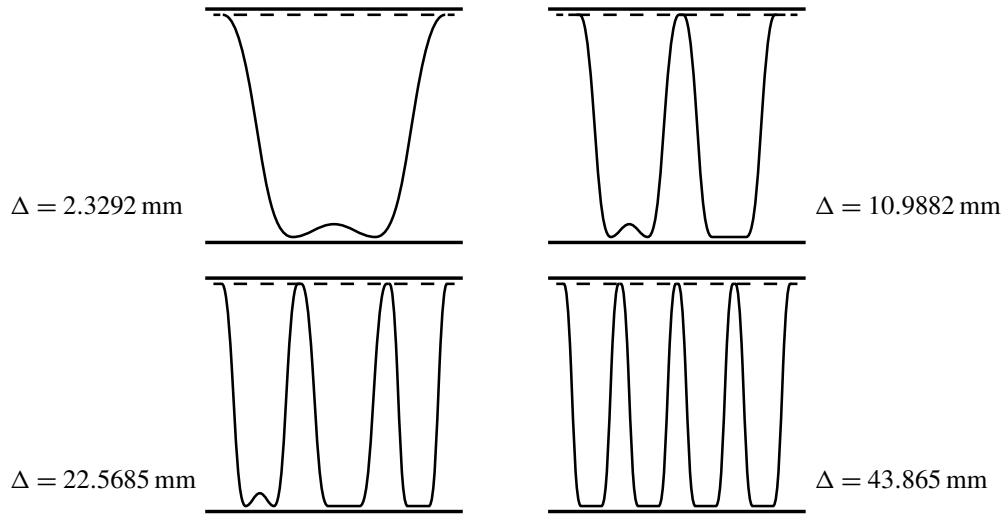


Figure 2. Deformed shape, magnified by a factor of 100, at four axial displacement values for a beam problem adopting the data of Figure 5 of [Chai 1998]. Dashed lines indicate undeformed shapes; thick solid lines indicate the final position of the rigid containment surfaces. FEM solution; 500 Timoshenko linear beam elements. Data as noted in the text.

must include some imperfection in order to exhibit buckling, the number of waves increases every time by one, for increasing axial shortening. This effect could be once more attributed to the existence of imperfections. The new configuration, when a new buckled wave is generated, is again (almost) periodic anyway.

The analysis of the possible evolution of the buckled configuration may start from the observation of a finite element (FEM) solution, shown in Figure 2. This solution is obtained by means of the commercial code ABAQUS [Hibbitt et al. 2013], and refers to the case of an infinitely rigid connection spring. The data reproduce the example analyzed in [Chai 1998], and are: length $L = 3000$ mm; rectangular cross-section 120×10 mm; gap $s = 15$ mm; Young's modulus $E = 210000$ MPa; axial shortening $\Delta = 43.865$ mm, so as to have a final value of Chai's parameter η equal to $\eta = 400$, as in Figure 5 of [Chai 1998]. The numerical analysis adopts a mesh of 500 Timoshenko 2-noded beam elements; it is conducted for prescribed axial shortening, in a regime of arbitrarily large strains and displacements. An initial geometrical imperfection is defined as an irregularity of the axis line of the beam, of the order of $\pm s/600$.

Figure 2 shows a remarkable complexity in the evolution of the buckled shape. It shows both the point and the line contacts described in [loc. cit.], but it also shows that a very common occurrence is a buckled shape having a line contact followed, along the axis line of the beam, by a point one. This occurrence is also found, both experimentally and numerically, in the analysis of BRBs in the elastic-plastic range [Genna and Gelfi 2012a], and it seems necessary to include it in the calculations concerning the lateral thrust.

A qualitative analysis of the evolution of the post-buckled shape of this type of structure seems to lead to the following possibilities.

2A. Initial contact. Before contact occurs, the situation is purely Eulerian. In the absence of imperfections a bifurcation would occur, of no practical interest. In a real case, what happens first depends strongly on the existing imperfections, that can lead to the formation of one or more than one contact points, in a way impossible to predict. As said, we will consider, for simplicity, only a case in which the first contact occurs at a single point.

Figure 3 illustrates the first stages of the post-buckled configuration. Each image shows a single wave, of length $2l_0$, of the deformed shape $v(z)$ at the top, and the corresponding bending moment $M(z)$ diagram at the bottom. Image 1, if $2l_0 = L$, refers to the time following the first contact. At the contact point, a local concentrated force (thrust) Q_i causes a local reduction of the bending moment. For increasing axial shortening, the increase of the thrust reduces the bending moment at the contact point until it becomes equal to zero (image 2). At this moment, two possibilities exist, as discussed in quantitative terms in the next section: (i, image 3a), one of the single half-waves buckles, thus forming a new wave with a new point contact situation; (ii, images 3b and 3c), the point contact becomes a line contact before any further local buckling occurs. This latter situation can be of two different types: a symmetric line contact, as in image 3c, or an asymmetric line contact, as in image 3b, with a line contact at one side and a point contact at the other. Which path will be actually followed depends on the existing imperfections; there seems to be no indication, from the theory, about a preferred path.

In order to simplify the presentation, the acronym PC will be used from now on to denote a pure point

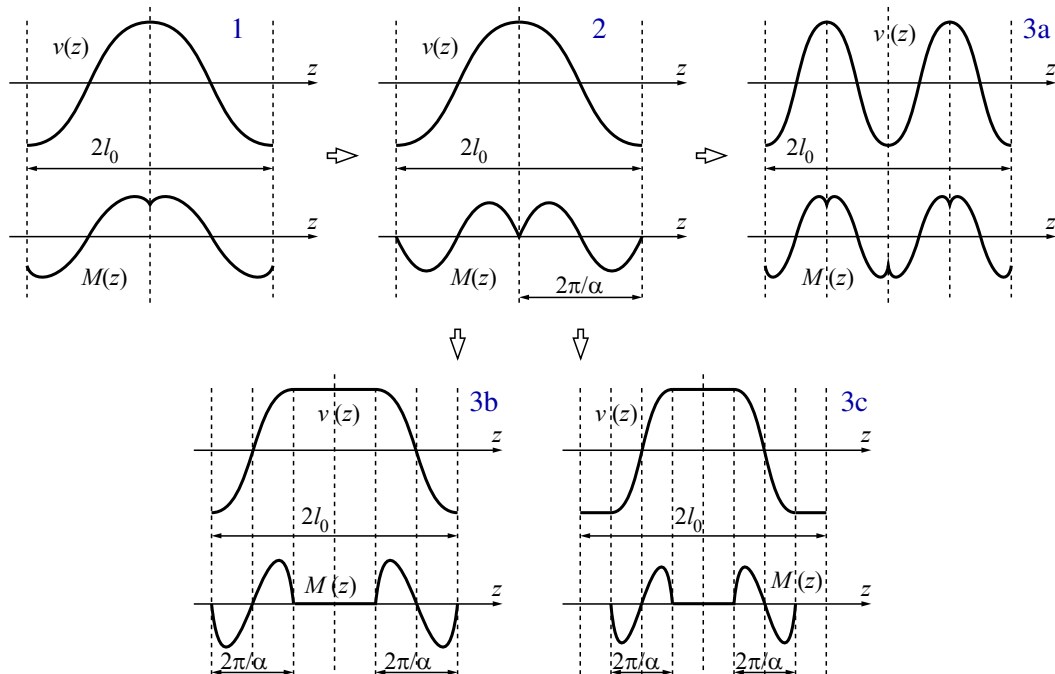


Figure 3. Possible evolution of the buckled shape after the first contact. One or two buckled waves are depicted. Image 2 refers to the instant when both the inclined portions of the beam reach a critical axial load value, with zero bending moment at the contact point. Images 3a, 3b, and 3c illustrate possible evolutions from the situation of image 2.

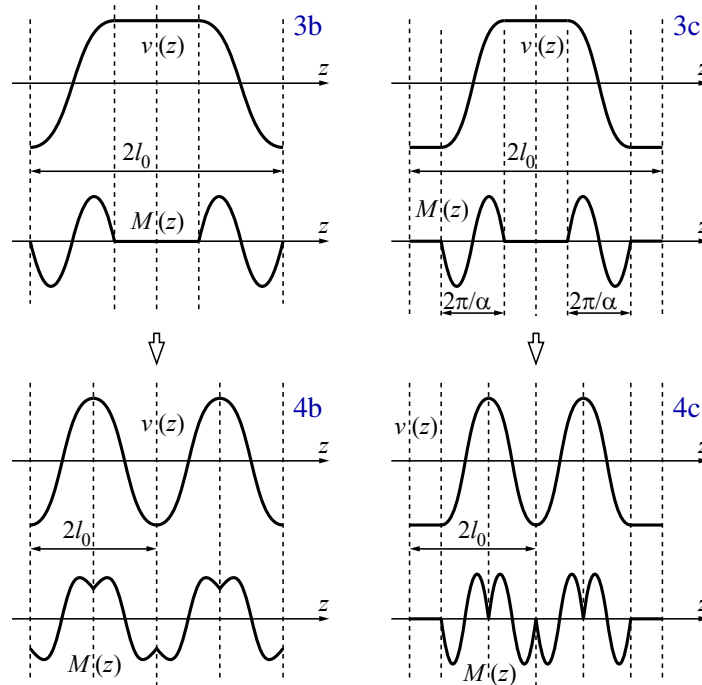


Figure 4. Possible evolution of the buckled shape from line contact situations. Images 3b and 4b refer to the evolution from an ALC configuration, and images 3c and 4c to the evolution from an SLC configuration.

contact situation; SLC will indicate a symmetric line contact, and ALC will indicate an asymmetric line contact as in image 3b of Figure 3.

2B. Evolution from a PC situation. Consider first a PC configuration like the one of image 1 in Figure 3, where now, in general, a single wave does not represent the full length of the beam. Recall that, despite the assumed periodicity, each time there is a local buckling only one new wave is generated, and the rest of the beam rearranges its configuration, according to the existing imperfections, in order to restore periodicity. Upon an increase of the axial shortening, any of the situations of Figure 3, images 3a, 3b, and 3c, can be reached next.

2C. Evolution from an ALC situation. Figure 4 shows the possible evolutions from both the line contact configurations. In the case of an ALC (images 3b and 4b), either one flat portion buckles, or one of the inclined portions buckles. In both cases, always assuming that only a single new wave can appear, and that periodicity must be restored, the next configuration has to be a PC one, illustrated in image 4b.

2D. Evolution from an SLC situation. Image 4c in Figure 4 shows the possible evolution from an SLC situation. In both the events that one flat portion or one inclined portion of a wave buckles, a new ALC configuration is reached.

It seems that in some cases, such as in Figure 4, image 4b, the bending moment at the point of the new contact can be nonzero independently of the number of preexisting waves. This condition would rule out

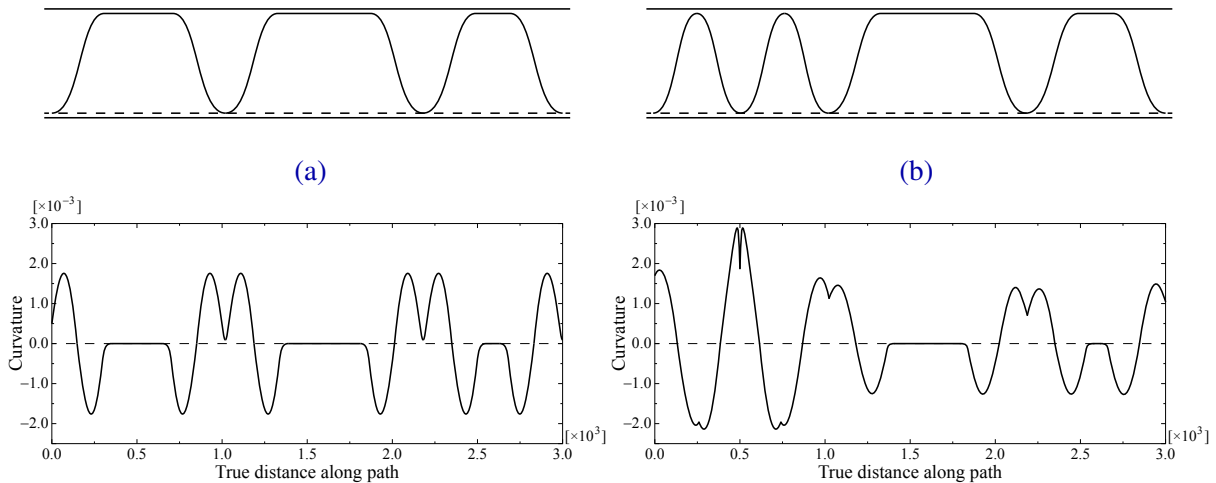


Figure 5. FEM analysis of the problem of Figure 2. Deformed shape (top, magnified by a factor of 20) and elastic curvature (bottom) at two successive times (a) and (b) during the post-buckling history. A line contact—the one at the extreme left in (a)—, with zero bending moment along it, transforms into a point contact with nonzero bending moment at the contact point, seen in (b). Dashed lines indicate undeformed shapes; thick solid lines indicate the final position of the rigid containment surfaces.

the possibility that the formation of a new wave occurs directly with a new line contact configuration: a line contact configuration, in fact, has zero bending moment all along the flattened portion of the beam. This can also be shown numerically: Figure 5 illustrates two successive instants during the deformation history of the same beam of Figure 2. At the first instant, on the left, a sequence of ALC configurations appears. At the second instant, on the right, after a little increment of the prescribed axial displacement, the left flat portion of the beam has buckled, forming a new wave with a new point contact situation. The bending moment, at the new contact point, is nonzero, as shown in the corresponding bottom image.

Several numerical solutions of this problem, with different geometries and different gaps, have always shown the evolution from one situation to another in terms of what described above. As apparent even from Figure 2, in a “real” case a full periodicity is not always reached, and, moving along the beam axis, one might encounter a sequence of PC, SLC, and ALC waves. Nevertheless, in order to perform analytical calculations to estimate the parameters of interest, full periodicity must be assumed anyway, as done in the next section.

3. Analytical calculation of the wavelength and associated lateral thrust

The technique adopted in this section is in part similar to that proposed in [Chai 1998], but has several important differences:

- Contact may occur, in general, against rigid surfaces that can translate, being connected to each other by an elastic spring. This could be either a distributed elastic foundation or, fully equivalently,

a single elastic spring as shown in Figure 1. The spring constant k of Figure 1 is in fact equivalent to the value of a foundation constant per unit length multiplied by the total length L of the beam.

- All the possibilities illustrated in the previous section are considered.
- The analysis considers as a main unknown the buckled wavelength, independent of the total length of the beam.
- The analysis aims at determining directly the wavelength corresponding to a given axial shortening.
- The beam total axial shortening Δ derives, in general terms, from both the axial deformability and the post-buckling bending, i.e., in a second-order theory,

$$\Delta = \bar{\varepsilon}L + \int_0^L \frac{1}{2}(v'(z))^2 dz, \quad (3-1)$$

where $\bar{\varepsilon}$ indicates the average membrane strain due to the axial stiffness, assumed positive if associated to shortening. In the sequel of this work, shortening and compression will always be assumed as positive.

Nevertheless, the assumption of a small value for the gap s , and the consequent adoption of a second-order theory, make it appropriate to neglect the bending contribution when considering the boundary conditions of the problem. This is true as long as the number of buckled waves does not become excessively high, a situation that can be easily ruled out in engineering applications. Therefore, in the sequel of this work the following global boundary condition will be adopted:

$$\Delta = \bar{\varepsilon}L. \quad (3-2)$$

In real applications, such as BRBs, the prescribed value of Δ can derive from any type of horizontal loading, such as wind or earthquake-induced, acting on a frame which includes the considered structural element as a bracing structure. The frame stiffness is usually much greater than the BRB stiffness; therefore, the ends of the BRB can be considered as hinged (or fully fixed, depending on the connection design), and subjected to a prescribed displacement.

3A. Equations for the case of point contact. Figure 6 shows the considered geometry and the adopted reference systems for the most general case of a point contact situation (solid lines only). The Figure shows a generic half-wave, of length l_0 , of the beam deformed shape. In this configuration, the two beam portions at the extreme left and right sides correspond to originally flat portions that have buckled simultaneously, forming each a new wave, possibly of different length at each side. Although such a situation has been ruled out a priori, previously, one can start from it from the sake of generality, and analyze its implications.

In all the calculations developed in the following, the buckled shape is assumed to be periodic along the beam length.

The two central inclined portions of the beam must have equal length, defined by the unknown parameter β , $0 < \beta \leq \frac{1}{2}$, in order to satisfy the geometric boundary conditions and in order to have the same force at the points of contact with the rigid surfaces (this could be checked analytically). This is an important consequence of the arrangement of Figure 1, which has no constraint for the absolute vertical

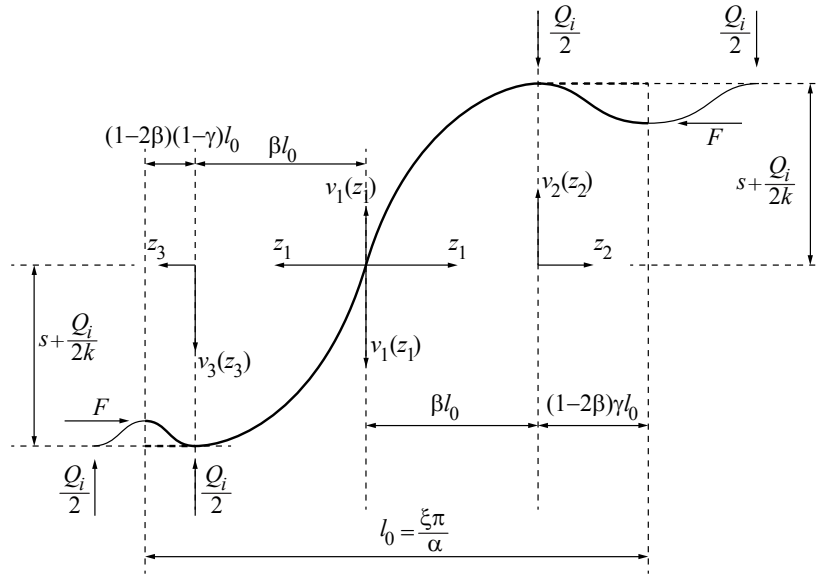


Figure 6. Structural scheme of a single half-wave of the buckled deformed shape. The solid lines represent a generic configuration of point contact. The dashed lines represent a generic configuration of line contact. Parameters ξ , β , and γ are unknown and define the geometrical properties of the half-wavelength l_0 .

translations of the rigid surfaces, in such a way that the total contact force acting on one surface must be equal to the corresponding force acting on the other.

The two lateral portions of the beam are initially assumed to have a different length, defined by the unknown parameter γ , $0 \leq \gamma \leq 1$.

As a consequence of this arrangement, only three different reference systems must be adopted for a single half-wave: one, indicated by z_1 , refers to the two central portions of the beam, whose deflection is denoted by $v_1(z_1)$; the two lateral portions of the beam are referred to systems z_2 and z_3 , respectively, and their deflections are denoted by $v_2(z_2)$ and $v_3(z_3)$, for the right and the left portions, respectively, with the conventions of Figure 6. Correspondingly, the bending moment for $z_1 = 0$, a point of flex for the deformed shape, is zero.

The axial force corresponding to the prescribed displacement Δ is denoted by F ; owing to the assumption of small displacements and linear elasticity, the following relation holds:

$$F = EA\bar{\epsilon} = \frac{EA}{L} \Delta, \tag{3-3}$$

where E denotes the Young’s modulus of the beam, and A the beam’s cross-sectional area.

At each contact point, the corresponding contact force is denoted by $Q_i/2$, Q_i indicating the unit thrust, i.e., the thrust associated to a single wave at each side of the buckled beam. The total thrust at each side of the beam, i.e., the force acting inside the connection spring, is given by

$$Q = Q_i N, \tag{3-4}$$

where N denotes the total number of buckled waves. Here, and for a while next, the following relationship is adopted, to relate the number of waves N to the half-wavelength l_0 :

$$N = \frac{L}{2l_0}. \quad (3-5)$$

Finally, the maximum amplitude of the buckled shape, at all the contact points, is given by

$$v_1(\beta l_0) = v_2(0) = v_3(0) = s + \frac{Q}{2k}. \quad (3-6)$$

This condition follows from the infinite bending stiffness of the external surfaces; one must also recall that the total elongation of the connection spring between the rigid surfaces, equal to Q/k , is twice the difference between the maximum amplitude $v_1(\beta l_0)$, at each side of the buckled beam, and the gap s .

It is possible, on the basis of the scheme of Figure 6, to write both the bending moment equations in all the beam parts, and the differential equations governing the deformed shapes:

$$\begin{aligned} M_1(z_1) &= Fv_1(z_1) - \frac{1}{2}Q_iz_1, & 0 \leq z_1 \leq \beta l_0, \\ M_2(z_2) &= Fv_2(z_2) - \frac{1}{2}Q_i\beta l_0, & 0 \leq z_2 \leq l_0(1 - 2\beta)\gamma, \\ M_3(z_3) &= Fv_3(z_3) - \frac{1}{2}Q_i\beta l_0, & 0 \leq z_3 \leq l_0(1 - 2\beta)(1 - \gamma), \end{aligned} \quad (3-7)$$

$$EIv_1''(z_1) = -M_1(z_1), \quad EIv_2''(z_2) = -M_2(z_2), \quad EIv_3''(z_3) = -M_3(z_3), \quad (3-8)$$

where the bending moments are assumed positive if causing tension in the top fibers in the two right portions of the beam, and in the bottom fibers in the two left portions of the beam, and I indicates the relevant moment of inertia of the beam cross-section: here, this will always assumed to be the minimum principal moment of inertia. Inserting (3-7) into (3-8) and rearranging terms in the usual way, one obtains:

$$\begin{aligned} v_1''(z_1) + \alpha^2 v_1(z_1) &= \frac{Q_i \alpha^2 z_1}{2F}, & v_2''(z_2) + \alpha^2 v_2(z_2) &= \frac{Q_i \alpha^2 \beta l_0}{2F}, \\ v_3''(z_3) + \alpha^2 v_3(z_3) &= \frac{Q_i \alpha^2 \beta l_0}{2F}, \end{aligned} \quad (3-9)$$

where

$$\alpha^2 = \frac{F}{EI}. \quad (3-10)$$

The half-wavelength l_0 is redefined in terms of the following nondimensional parameter ξ , which, together with parameters β and γ introduced earlier, will be the main unknown of this problem:

$$l_0 = \xi \frac{\pi}{\alpha} \quad (3-11)$$

in such a way that the following also holds:

$$F = \xi^2 \frac{\pi^2 EI}{l_0^2}. \quad (3-12)$$

This allows an immediate comparison of the results for the wavelength with the standard Euler results for elastic buckling, where $\xi = 1$ always.

The relevant boundary conditions are as follows:

$$v_1(0) = 0, \quad (3-13)$$

$$v_1(\beta l_0) = v_2(0) = v_3(0) = s + \frac{Q}{2k}, \quad (3-14)$$

$$v_1'(\beta l_0) = 0, \quad (3-15)$$

$$v_2'(0) = v_3'(0) = 0, \quad (3-16)$$

$$v_2'[l_0(1 - 2\beta)\gamma] = 0, \quad (3-17)$$

$$v_3'[l_0(1 - 2\beta)(1 - \gamma)] = 0. \quad (3-18)$$

The integration of equations (3-9) yields the following results:

$$v_1(z_1) = C_1 \cos \alpha z_1 + C_2 \sin \alpha z_1 + \frac{Q l_0 z_1}{FL}, \quad (3-19)$$

$$v_2(z_2) = C_3 \cos \alpha z_2 + C_4 \sin \alpha z_2 + \frac{Q \beta l_0^2}{FL}, \quad (3-20)$$

$$v_3(z_3) = C_5 \cos \alpha z_3 + C_6 \sin \alpha z_3 + \frac{Q \beta l_0^2}{FL}. \quad (3-21)$$

It is convenient to start with the analysis of functions v_2 and v_3 in (3-20) and (3-21). The equations (3-16) yield immediately $C_4 = C_6 = 0$. The equations (3-17) and (3-18) are then rewritten as:

$$-\alpha C_3 \sin [\alpha l_0(1 - 2\beta)\gamma] = 0 \quad \text{and} \quad -\alpha C_5 \sin [\alpha l_0(1 - 2\beta)(1 - \gamma)] = 0, \quad (3-22)$$

respectively. These can be satisfied in the following ways:

- (1) By setting $C_3 = C_5 = 0$, which would correspond to line contact solutions, for the moment of no interest; or
- (2) By prescribing what follows:

$$\alpha l_0(1 - 2\beta)\gamma = \pi, \quad (3-23)$$

$$\alpha l_0(1 - 2\beta)(1 - \gamma) = \pi, \quad (3-24)$$

which, making use of (3-11), gives

$$\gamma = \frac{1}{\xi(1 - 2\beta)} \quad \text{and} \quad 1 - \gamma = \frac{1}{\xi(1 - 2\beta)}. \quad (3-25)$$

These conditions imply

$$\gamma = \frac{1}{2}, \quad \beta = \frac{1}{2} - \frac{1}{\xi}, \quad (3-26)$$

which corresponds to a situation in which, starting from a pure SLC case, both the flat portions of the wave have just buckled, and there are two new contact points at each side of each wave.

This case, in the framework herein considered, has been ruled out, since only the formation of a single new wave at a time is allowed; nevertheless, it can, and will, be easily incorporated into the next calculations, so as to take into account also the result for ξ associated to it.

In addition to these cases, two more possibilities can be obtained from the above equations, by setting equal to zero either one or both the lengths of the lateral extremities of the wave.

The first additional case corresponds to setting, equivalently, $\gamma = 0$ or $\gamma = 1$. Let's consider only the latter choice; then, only functions $v_1(z_1)$ and $v_2(z_2)$ survive, and only the boundary condition (3-23) must be considered, which yields

$$\gamma = 1 \implies \beta = \frac{1}{2} \left(1 - \frac{1}{\xi} \right). \quad (3-27)$$

This corresponds to a situation in which, starting from a pure ALC case, the flat portion of the wave has just buckled. There is one contact point at one side of the wave, and two contact points at the opposite side.

A second additional possibility derives from setting $\gamma = 0$ and $\beta = \frac{1}{2}$, which describes a pure PC situation, in which only function $v_1(z_1)$ survives and there is only one contact point at each side of a single wave.

In this way, it is seen that the case of point contact has three possible subcases, of which one, defined by (3-26), has only a purely theoretical interest since, in practice, the existence of imperfections makes it impossible to occur.

The determination of parameter ξ for the three possible subcases follows.

For all of them, function $v_1(z_1)$ is uniquely defined by the same conditions. Prescribing the boundary conditions (3-13), (3-14), and (3-15) one obtains

$$v_1(z_1) = \frac{2\pi\xi ks[\sin(\alpha z_1) - \alpha z_1 \cos(\pi\xi\beta)]}{\cos(\pi\xi\beta)(\alpha^2 FL - 2\pi^2\xi^2\beta k) + 2\pi\xi k \sin(\pi\xi\beta)}, \quad (3-28)$$

$$Q_i = \frac{4\pi\xi\alpha k F s \cos(\pi\xi\beta)}{\cos(\pi\xi\beta)(2\pi^2\xi^2\beta k - \alpha^2 FL) - 2\pi\xi k \sin(\pi\xi\beta)}. \quad (3-29)$$

Correspondingly, the bending moment associated to the function $v_1(z_1)$ is given by:

$$M_1(z_1) = EI \frac{2\pi\xi\alpha^2 ks \sin(\alpha z_1)}{\cos(\pi\xi\beta)(\alpha^2 FL - 2\pi^2\xi^2\beta k) + 2\pi\xi k \sin(\pi\xi\beta)}. \quad (3-30)$$

In all these expressions, the wavelength parameters ξ and β are still to be computed.

As proposed in [Genna and Gelfi 2012b], the parameter ξ is computed by prescribing the stationarity of the total potential energy (TPE) with respect to it. Unless one is ready to follow the complete history of the prescribed axial displacement, in fact, there seems to be no other way to determine the correct configuration associated to a given value of Δ . Even following the actual loading history, it seems difficult, in the absence of specific information about the existing imperfections, to prescribe a priori, as done in [Chai 1998], the number of waves generated by a local buckling, starting from any given configuration. Therefore, it appears that the minimization of the total potential energy is the safest tool to obtain the correct response.

In order to write the TPE, for the problem under examination, it is convenient to reconsider it as force-driven, and to express the force, at the end of the calculations, as a function of the prescribed axial shortening by means of (3-3).

The TPE for an axially compressed beam of length L , whose transversal deflection is indicated by $v(z)$ and axial displacement by $u(z)$, can be written, in a second-order theory, as follows:

$$\text{TPE}[v(z), u(z)] = \frac{1}{2} \int_0^L (EI(v'')^2(z) + EA(u')^2(z)) dz - F\Delta. \quad (3-31)$$

In this equation, the boundary condition (3-1) should be considered for the axial shortening Δ . If one wants to distinguish between the bending and the axial contribution to the beam shortening, then the average membrane strain $\bar{\epsilon}$ is an unknown, that can be calculated once the $u(z)$ function is obtained.

It must now be recalled that the stationarity of the TPE of equation (3-31), in a second-order theory, would furnish a bending result $v(z)$ fully uncoupled from the axial one $u(z)$.

As a consequence, exploiting the smallness of the gap s , and in order to avoid the useless complication of calculating also the unknown function $u(z)$ and the associate average strain $\bar{\epsilon}$, here, as said, the average axial strain is assumed as known, given by (3-2), and the axial contribution to the TPE is completely ignored. Some comments about this simplification will be given in Section 4. Therefore, for the problem under investigation, the total potential energy TPE can be written, for the general configuration of Figure 6, as follows:

$$\begin{aligned} \text{TPE}[\xi] = & 4N \frac{1}{2} \int_0^{\beta l_0} (EI(v_1'')^2(z_1) - F(v_1')^2(z_1)) dz_1 + 2N \frac{1}{2} \int_0^{l_0(1-2\beta)\gamma} (EI(v_2'')^2(z_2) - F(v_2')^2(z_2)) dz_2 \\ & + 2N \frac{1}{2} \int_0^{l_0(1-2\beta)(1-\gamma)} (EI(v_3'')^2(z_3) - F(v_3')^2(z_3)) dz_3 + \frac{1}{2} 4k(v_1(\beta l_0) - s)^2 H[(v_1(\beta l_0) - s)], \end{aligned} \quad (3-32)$$

where $H[\cdot]$ indicates the Heaviside function, required here to prescribe the existence of a contact force only if the maximum deflection of the core equals or exceeds the nominal gap s .

By prescribing the stationarity of the TPE of equation (3-32) with respect to ξ , for any choice of β and γ among the three listed above, one obtains a nonlinear equation in ξ , that, in general, must be solved numerically.

3A1. Pure PC case, single contact point at each side. This is the case already considered in [Genna and Gelfi 2012b], where, though, only fully fixed rigid surfaces were introduced. This corresponds to setting $\beta = \frac{1}{2}$ in the previous equations, in such a way that both functions $v_2(z_2)$ and $v_3(z_3)$, which do not exist, disappear from (3-32).

The numerical results will be presented in the next section. Nevertheless, it is of interest to furnish immediately the result in the limit $k \rightarrow \infty$. In such a case, the stationarity equation reduces to

$$\tan(\xi\pi) = \xi\pi, \quad (3-33)$$

which has the solution

$$\xi \approx 1.4303, \quad (3-34)$$

i.e., the result found in [loc. cit.]. In the limit $k \rightarrow \infty$, equation (3-29) for the unit thrust reduces to

$$Q_{i,\infty} = \frac{2\alpha F s \cos(\pi\xi\beta)}{\pi\xi\beta \cos(\pi\xi\beta) - \sin(\pi\xi\beta)}, \quad (3-35)$$

which holds for all the values of β and ξ deriving from a situation of pure contact at both sides of the beam.

3A2. *Symmetric case, double contact point at each side.* In this case (3-26) holds. Adopting these values, one can obtain both the integration constants C_3 and C_5 from the boundary conditions (3-14). The result is:

$$C_3 = C_5 = \frac{2\pi\xi ks \sin\left(\frac{\pi\xi}{2}\right)}{\cos\left(\frac{\pi\xi}{2}\right)(\alpha^2 FL - \pi^2(\xi - 2)\xi k) + 2\pi\xi k \sin\left(\frac{\pi\xi}{2}\right)}. \quad (3-36)$$

Accordingly, the two remaining equations for the buckled shape are:

$$v_2(z_2) = v_3(z_3) = \frac{\pi\xi ks \left(\pi(\xi - 2) \cos\left(\frac{\pi\xi}{2}\right) - 2 \sin\left(\frac{\pi\xi}{2}\right) \cos(\alpha z_{2(3)}) \right)}{\cos\left(\frac{\pi\xi}{2}\right) (\pi^2(\xi - 2)\xi k - \alpha^2 FL) - 2\pi\xi k \sin\left(\frac{\pi\xi}{2}\right)}, \quad (3-37)$$

and the TPE of equation (3-32) can be computed as a function of ξ .

As before, it is of interest to furnish immediately the result for ξ in the limit $k \rightarrow \infty$. In such a case, the equation expressing the stationarity of the TPE of equation (3-32) reduces to

$$\pi(\xi - 1) \cos(\xi\pi) = \pi + \sin(\xi\pi), \quad (3-38)$$

which has the solution

$$\xi \approx 3.58639. \quad (3-39)$$

3A3. *Asymmetric case, double contact point at the top side, single contact point at the bottom side.* In this case (3-27) holds, with $\gamma = 1$. Adopting these values, function $v_3(z_3)$ disappears from the picture, and one obtains the integration constant C_3 from the relevant boundary condition of (3-14). The result is:

$$C_3 = \frac{2\pi\xi ks \cos\left(\frac{\pi\xi}{2}\right)}{2\pi\xi k \cos\left(\frac{\pi\xi}{2}\right) - \sin\left(\frac{\pi\xi}{2}\right) (\alpha^2 FL - \pi^2(\xi - 1)\xi k)}. \quad (3-40)$$

Accordingly, the remaining equation for the buckled shape is:

$$v_2(z_2) = \frac{\pi\xi ks \left(2 \cos\left(\frac{\pi\xi}{2}\right) \cos(\alpha z_2) + \pi(\xi - 1) \sin\left(\frac{\pi\xi}{2}\right) \right)}{2\pi\xi k \cos\left(\frac{\pi\xi}{2}\right) - \sin\left(\frac{\pi\xi}{2}\right) (\alpha^2 FL - \pi^2(\xi - 1)\xi k)}. \quad (3-41)$$

Once more, it is of interest to furnish immediately the corresponding result in the limit $k \rightarrow \infty$. In such a case, the equation expressing the stationarity of the TPE of equation (3-32) reduces to

$$\pi(1 - 2\xi) \cos(\xi\pi) = \pi - 2 \sin(\xi\pi), \quad (3-42)$$

which has the solution

$$\xi \approx 2.52875. \quad (3-43)$$

3B. Equations for the case of line contact. A line contact starts occurring at the instant when the bending moment, at the extremities of an inclined portion of the buckled wave, becomes equal to zero. The first occurrence of this situation is illustrated in Figure 3, image 2. Upon an increase of the axial shortening, after a PC situation, the unit thrust Q_i increases until the bending moment, at the contact point, becomes zero. Thereafter, three possibilities exist, as discussed in Section 2B. A first one implies the return to a pure PC situation, with a complete rearrangement of the waves; two others imply the progressive flattening of a portion of the beam included between the points of application of half the unit thrust, as shown in images 3b and 3c of Figure 3.

In all the cases when the bending moment is zero at the extremities of an inclined portion of the beam, it is immediate to obtain the corresponding length of the inclined portion itself from (3-30), by prescribing the following condition:

$$M_1(z_1 = \beta l_0) = 0 \implies \sin(\alpha \beta l_0) = 0. \quad (3-44)$$

This implies (recall also (3-11)):

$$\beta l_0 = \frac{\pi}{\alpha} \implies \beta = \frac{1}{\xi}. \quad (3-45)$$

For the specific situation of Figure 3, image 2, i.e., the limiting case of a pure PC situation, with $\beta = \frac{1}{2}$, one thus gets

$$\xi_{\max} = 2. \quad (3-46)$$

This is the result always adopted in [Genna and Gelfi 2012b] to relate the buckled wavelength to a prescribed value of axial shortening, since the value $\xi = 2$ gave a better prediction than the theoretical result of (3-34). Genna and Gelfi [2012b], however, took into account only a PC configuration, whereas, in the previous paragraphs of the present work, it was already shown that, upon considering more general cases, even larger values for the coefficient ξ can be found.

In all the configurations of Figure 3 with zero bending moment at the extremities of the inclined parts of the wave, under the validity of (3-45), both these inclined parts have reached a local buckling load. What happens for an increase of axial shortening is not uniquely defined: as observed in Section 2, either the inclined portions buckle, or the line contact portion buckles, or, if a line contact portion does not exist yet, when $\xi = 2$ for a PC situation, flattening starts developing at the contact point. In this latter case, the unit thrust Q_i splits into separate forces of intensity $Q_i/2$ each, acting at the lateral extremities of the line contact zone. What really happens depends on the existing imperfections.

If a line contact has already developed, such as in Figure 3, images 3b and 3c, condition (3-45) allows one to easily compute all the limit situations that can derive from a line contact in the case that the next critical phenomenon is the local buckling of the flat portion. One can consider the most general situation of a line contact, which includes, as special cases, both the ALC and SLC situations considered so far. This is the configuration depicted by the dashed lines in Figure 6, where the lengths of the two flat portions can be in any ratio between each other.

The maximum value that can be reached by the wavelength parameter ξ , starting from the configuration described by the central portion of the beam plus the lateral dashed lines in Figure 6, corresponds to the first local buckling of the flat portions. Assume, with no loss of generality, that $\gamma \geq \frac{1}{2}$, so that the right flat portion of the beam buckles first. In this case, according to (3-45) and recalling definition (3-11), one has

$$(1 - 2\beta)\gamma l_0 = \left(1 - \frac{2}{\xi}\right)\gamma \frac{\xi\pi}{\alpha} = l_1. \quad (3-47)$$

The maximum value for the corresponding wavelength is obtained under the following value of the critical axial load F^* :

$$F^* = \frac{\pi^2 EI}{l_1^2}. \quad (3-48)$$

This condition, using (3-47), implies

$$\xi_{\max} = \frac{1+2\gamma}{\gamma}. \quad (3-49)$$

If one now recalls that the only possible values for $\gamma \geq \frac{1}{2}$ are $\gamma = \frac{1}{2}$ or $\gamma = 1$, one obtains immediately:

- For $\gamma = \frac{1}{2}$, i.e., starting from an SLC configuration:

$$\xi_{\max} = 4. \quad (3-50)$$

Note that, immediately after this situation, in principle both the flat portions of the wave would buckle, thus creating a new situation for which result (3-39) holds: the wavelength decreases in a discontinuous way.

- For $\gamma = 1$, i.e., starting from an ALC configuration:

$$\xi_{\max} = 3. \quad (3-51)$$

Note that, immediately after this situation, the flat portion of the wave buckles, thus creating a new situation for which result (3-43) holds: the wavelength decreases in a discontinuous way.

If the bending moment for $z_1 = \beta l_0$ vanishes, the unit thrust Q_i can be obtained directly from the global equilibrium of the central inclined portion of the beam, i.e., (see Figure 6):

$$F\left(s + \frac{Q}{2k}\right) = \frac{Q_i}{2}\beta l_0 \implies F\left(s + \frac{Q_i L \alpha}{4k\pi\xi}\right) = \frac{Q_i}{2} \frac{\pi}{\alpha}, \quad (3-52)$$

and has the following final expression:

$$Q_{i, M_1(\beta l_0)=0} = \frac{4\pi\xi\alpha k F s}{2\pi^2\xi k - \alpha^2 F L}, \quad (3-53)$$

which, in the limit $k \rightarrow \infty$, yields the following trivial result, independent of both ξ and L (see also [Genna and Gelfi 2012b]):

$$Q_{i, M_1(\beta l_0)=0, \infty} = \frac{2F\alpha s}{\pi}. \quad (3-54)$$

Equation (3-53) is also a particularization of (3-29) for the case in which equations (3-45) and (3-47) hold.

4. Numerical results and discussion

It was shown that the wavelength associated to a given axial shortening can be governed, according to the different possible situations, by several different values of parameter ξ . Even in the case of a rigid connection spring, the coefficient ξ takes values in the range $1.4303 \leq \xi \leq 4$. In the case of a deformable connection spring, the situation becomes definitely more complex.

In the presence of a line contact, either fully developed or incipient, the results of equations (3-46), (3-50), and (3-51), for the maximum value of ξ before a change of configuration under the condition of (3-45), hold for any value of the spring stiffness k .

On the contrary, in all the possible cases of point contact both the parameter ξ and the thrust Q depend on the stiffness of the connection spring in a complex way, illustrated, for the pure PC case (i.e., $\beta = \frac{1}{2}$), in Figures 7, 8, and 9. These figures plot, as a function of the spring stiffness k normalized by $\alpha^2 F L$, the corresponding values for ξ , Q_i , and Q , respectively. In Figures 8 and 9 the values of the thrusts have been normalized to obtain dimensionless quantities. The values for ξ have been calculated numerically, solving the stationarity equation of the TPE of equation (3-32) by means of Newton's method.

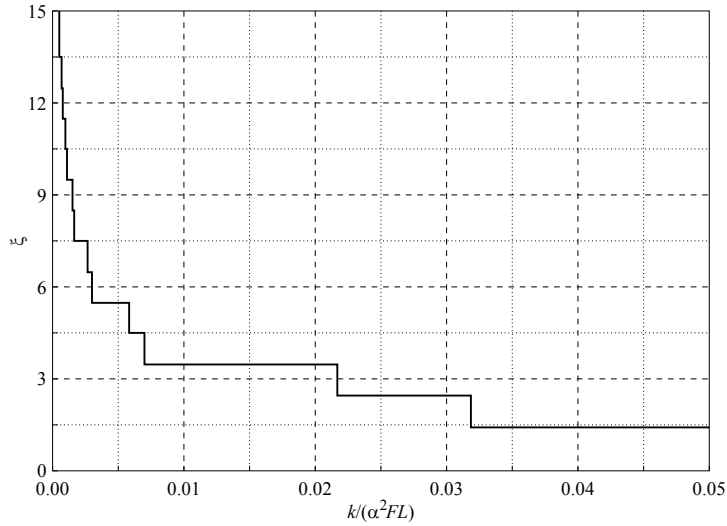


Figure 7. Values for the parameter ξ as a function of the connection spring stiffness k normalized by $\alpha^2 FL$, as computed from the stationarity of the TPE of equation (3-32) for the case $\beta = \frac{1}{2}$.

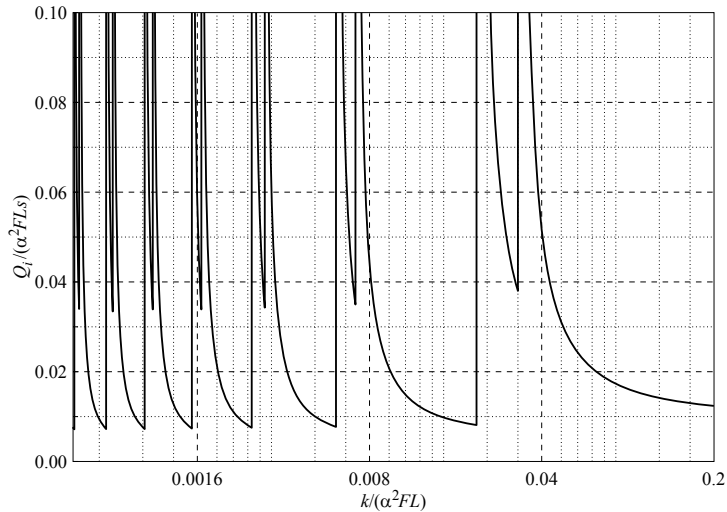


Figure 8. Values of the unit thrust Q_i , normalized by $\alpha^2 FLs$, as a function of the normalized spring stiffness $k/\alpha^2 FL$, for $\beta = \frac{1}{2}$ and ξ as in Figure 7, as given by (3-29). Other data are: rectangular cross-section 5×50 mm, $E = 210000$ MPa, $L = 560$ mm, $s = 0.5$ mm, $\Delta = 11.2$ mm.

Similar results could be shown (they are not for the sake of brevity) for different cases of point contact, i.e., for the other possible choices of the parameters β and γ as computed in Section 3A1.

The jumps of the values for ξ correspond to infinite values of the unit thrust Q_i . As can be seen from the denominator of (3-29), the normalization of k by $\alpha^2 FL$ yields values for ξ that do not depend on any further parameter.

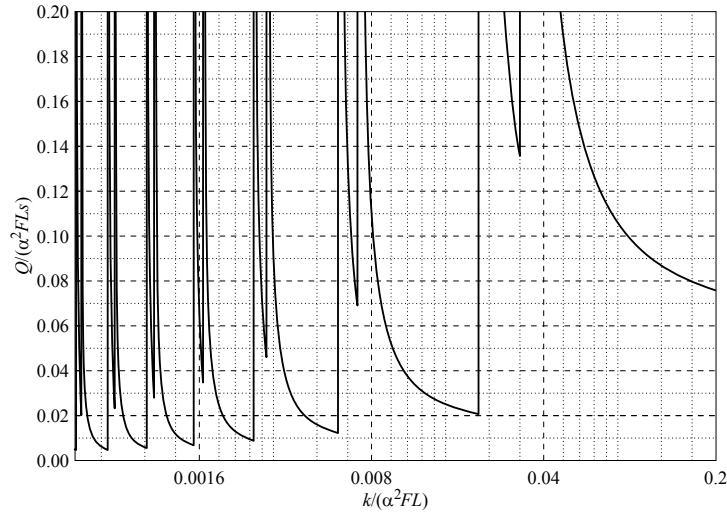


Figure 9. Values of the total thrust Q , normalized by $\alpha^2 FL_s$, as a function of the normalized spring stiffness $k/\alpha^2 FL$, for $\beta = \frac{1}{2}$ and ξ as in Figure 7, as given by (3-4) and (3-5). Other data as in Figure 8.

The values for ξ take a descending step shape, staying constant in a range of values for k and then jumping to a smaller value for an infinitesimal increase of k , until the limiting value $\xi \approx 1.4303$ is reached. The jumps in the values of ξ are not of constant value, although they are all quite close to unity. In the considered range of values for k , ξ goes from $\xi \approx 15.49$ to $\xi \approx 1.4303$, which is its minimum possible value. As said, here ξ depends only on the normalized value of k , and is independent of L . This fact makes its determination simpler than the determination of the wave number N , as done in [Chai 1998] (there only for $k \rightarrow \infty$).

All the results tend to their corresponding counterparts in the limit $k \rightarrow \infty$. For finite values of k , one sees an interplay between the tendency to form less and less waves as the spring stiffness decreases (in the limit $k \rightarrow 0$ only one wave would be formed), which would imply smaller and smaller lateral thrusts, and to produce a higher thrust as the maximum displacement of the buckled shape increases, i.e., as k decreases with a constant number of waves.

The unit thrust of Figure 8 increases rapidly with decreasing k , for constant values of ξ , tending to an infinite value. The total thrust of Figure 9 follows a similar trend, in which, in addition, the tendency towards smaller values as k decreases, but for an increasing number of waves, is more apparent.

All the values of the thrust depend on all the parameters of the problem; even the value for Q_i in the limit $k \rightarrow \infty$, given by (3-54), depends linearly on the gap s and on the product αF . In addition, all the values for Q depend also on the total length L .

It is worth commenting about the effect of replacing the boundary condition in (3-2) with the boundary condition (3-1). These comments will be restricted, for the sake of simplicity, to the case of infinite stiffness of the connection spring, and only to the situation of a PC contact.

If one treats the membrane strain $\bar{\epsilon}$ of equations (3-2) and (3-1) as an unknown, given a value of the prescribed shortening displacement Δ , then, still following the path described in the previous section, the axial force corresponding to Δ is unknown, defined by the first relationship in (3-3), and the total

potential energy of (3-31) becomes a function of the two unknowns ξ and $\bar{\varepsilon}$. In order to compute both unknowns, the easiest way is to impose (3-1) in strong form, and couple it with the stationarity of the TPE of (3-32) with respect to ξ . One thus obtains in any case the result $\xi \approx 1.4303$, and values for $\bar{\varepsilon}$ that depend essentially on the value of the gap s . For small gaps, the membrane strain tends to coincide with the nominal strain Δ/L ; only for large gaps the effect of the bending strain becomes important.

Consider, as an example, the problem extensively studied in [Genna and Gelfi 2012a], which has the following set of data: $L = 560$ mm; $E = 210000$ MPa; rectangular cross-section 5×50 mm; gap $s = 0.5$ mm; $\Delta = 11.2$ mm. If one adopts (3-2), one has immediately $\bar{\varepsilon} = 0.02$, and $F = 1050000$ N as the applied axial force; if one adopts the boundary condition in (3-1), one computes $\bar{\varepsilon} = 0.01978$ and $F = 1038600$ N. If one considers a gap $s = 1.0$ mm, then (3-1) yields $\bar{\varepsilon} = 0.01915$ and $F = 1005190$ N; but with $s = 5.0$ mm one finds $\bar{\varepsilon} = 0.009438$ and $F = 495491$ N, with a substantial difference between the two approaches. In this last case, the bending contribution to the axial displacement, given by the second term in (3-1), is $\Delta_b = 5.91476$ mm.

Similar results are obtained using a very different set of data, taken from the example studied in [Gelfi and Metelli 2007]: $L = 3000$ mm; $E = 210000$ MPa; rectangular cross-section 10×120 mm; gap $s = 1.0$ mm; $\Delta = 60.0$ mm. Using (3-2) one has $\bar{\varepsilon} = 0.02$ and $F = 5040000$ N; using (3-1) one finds $\bar{\varepsilon} = 0.01978$ and $F = 4983680$ N. Only with a gap $s = 10.0$ mm one finds a significant difference between the two approaches, (3-1) providing $\bar{\varepsilon} = 0.0094$ and $F = 2371250$ N.

Therefore, it seems reasonable to conclude that, if one restricts the attention to the case of small gaps and small buckled amplitudes, the use of (3-2) is perfectly adequate. In the presence of exceedingly large gaps a second-order approximation would lose validity altogether.

Some comments are now given about the important topic of the meaning of the obtained analytical results with reference to the calculation of the lateral thrust in actual BRBs. We still refer to a fully ideal BRB situation, in which linear elasticity holds for the core material, no friction exists between core and containment profiles, and the loading is monotonic.

Even in this ideal case, it seems impossible, in practice, to predict with accuracy the half-wavelength l_0 . Owing to the effect of the imperfections, in fact, the actual configuration under any given value of the axial shortening Δ could be any of those herein considered, and the relevant value for ξ can take any of the values computed accordingly.

This fact could be confirmed numerically. The problem of [Genna and Gelfi 2012a] has been solved numerically several times using the FEM code ABAQUS [Hibbitt et al. 2013] using a mesh of 3000 Timoshenko linear beam elements, with frictionless unilateral contact against rigid surfaces in the case $k \rightarrow \infty$. Each analysis introduced a different type of initial imperfection, which was either a deviation from linearity of the beam axis or the presence of a small transversal load, in some case having a quick temporal variation in order to influence in a “random” way the formation of new buckled waves. Changing the type of this imperfection, for $\Delta = 11.2$ mm, i.e., $\bar{\varepsilon} = 0.02$, quite different solutions were predicted, with a number of waves variable from 1 to 3, with l_0 variable from 250 mm to 90 mm, and with a total lateral thrust variable from 17073 N to 103366 N.

Suggestions about a reasonable engineering compromise for the choice of parameter ξ will be given shortly.

Another difficult point concerns the calculation of the total thrust Q . Even though the unit thrust Q_i is not strongly dependent on the value of ξ in several cases (see for instance (3-54); but also in other

situations the unit thrust, for reasonable values of the parameters, does not depend too much on the value of ξ — see also Tables 1 and 2 on page 461), the value of the total thrust Q exhibits always a strong dependence on both ξ and, of course, L . The difficulty, here, derives from the adoption of (3-5) to relate the wave number to the wavelength: this expression furnishes real (as alternative to integer) values for N , which is not correct, since N has to be an integer.

This problem is of difficult solution as long as one needs to take into account also the stiffness k of the elastic connection spring. In this case, in fact, all the aspects of the solution become strongly coupled, and all the parameters of interest vary in a quite large range of values, depending on the actual value of k ; the thrust can jump to infinity, which makes it completely unpredictable.

Nevertheless, considering that a correct estimate of the spring constant k is not so easy, and considering that the good functioning of a BRB depends anyway on a high stiffness of the containment structure, it can be safely concluded that an engineer should endeavor to design the containment profiles stiff enough to make them behave as almost rigid, i.e., in the range of values for k associated to the result $\xi \approx 1.4303$ for the pure PC situation for all the expected values of the axial force.

Then, by restricting the attention to the case $k \rightarrow \infty$, it is possible to reach some acceptable results. In the first place, the admissible values for ξ are now limited in the range $1.4303 \leq \xi \leq 4$. Considering that, in practice, asymmetric configurations will be more likely than fully symmetric ones, as also shown by experiments and numerical simulations (see for instance [Genna and Gelfi 2012a] and [Bregoli 2014]), one is lead to adopt values in the range $2.52875 \leq \xi \leq 3$, $\xi = 3$ being the simplest choice, not so far from the trivial average value $\xi = (1.4303 + 4)/2 = 2.72$.

One further reason for adopting the value $\xi = 3$ as an estimate for the wavelength derives from thinking in terms of elastic-plastic behavior, obviously important in engineering applications such as BRBs. In the elastic-plastic case, the axial force F can definitely reach and overcome the elastic limit for the compressed core. This means that at the contact points the bending moment contribution can not be high anyway, considering that the cross-section has almost fully exhausted its stress-carrying capacity because of the axial force alone. Therefore, one should reasonably expect a situation in which the bending moment is zero, or nearly so, at the contact points, which implies that coefficient ξ can assume the limit value $\xi_{\max} = 2$ for a PC situation, $\xi_{\max} = 3$ for an ALC situation, or $\xi_{\max} = 4$ for an SLC one. Considering that all these values are the maximum possible in each case, and that in a real situation (elastic-plastic, with friction, etc.) symmetry is less and less likely, it seems more appropriate to choose the asymmetric case value, i.e., $\xi = 3$.

Finally, recall also that values $\xi > 3$, with $k \rightarrow \infty$, correspond to situations in which two new waves would be formed simultaneously, a case that in reality does never occur; $\xi = 3$ seems therefore to be the highest possible value that can be reached in the case of an infinitely rigid connection spring, and a reasonable engineering choice, in the absence of information about imperfections.

According to this choice, the expression for the unit thrust to be adopted becomes (3-53), which, in the case of a rigid connection spring, reduces to (3-54).

Once agreed on this, then it is finally possible to tackle the problem of computing the total thrust on the basis of an integer number of waves.

If one attempts to make the TPE extreme with respect to feasible values of N , with N an integer (this can be easily done numerically), one finds results not much distant from the analytical ones given by the use of (3-5). It can be seen, actually, that, given ξ , the corresponding choice, for the correct integer N_{int} ,

is given by

$$N_{\text{int}} = \text{Int}(N + 0.5), \quad (4-1)$$

i.e., the nearest integer to N given by (3-5). Therefore, in computing the unit thrust Q for a given ξ , on the basis of (3-4), it is suggested to adopt expression (4-1) instead of (3-5).

In order to have an idea of the approximation provided by the proposed procedure, one can once more consider the two examples of [Genna and Gelfi 2012a] and [Gelfi and Metelli 2007]. Both geometries have been studied using the FEM code ABAQUS [Hibbitt et al. 2013], adopting a full 3D mesh for the core, with linear elasticity for the core material, and frictionless rigid surfaces for the containment. In the case of 3D analyses, the adopted imperfection was only a small fraction of the self weight of the beam, considered acting as a transversal load. In general, the FEM solutions obtained by means of continuum models tend to be less sensitive to imperfections than solutions given by beam models, and even less sensitive in the elastic-plastic range, as was also found in [Genna and Gelfi 2012a], and as will be discussed in work under way. The following numerical results have been obtained:

- geometry of [Genna and Gelfi 2012a] with $\Delta = 11.2$ mm; $l_0 \approx 70$ mm, $\xi \approx 2.06$; $N = 4$; $F = 938464$ N; $Q_i = 24438$ N; $Q = 97750$ N;
- geometry of [Gelfi and Metelli 2007] with $\Delta = 60.0$ mm; $l_0 \approx 150$ mm, $\xi \approx 2.44$; $N = 9$; $F = 5466330$ N; $Q_i = 143060$ N; $Q = 1287540$ N.

The corresponding analytical results, for $k \rightarrow \infty$, are shown in Tables 1 and 2, respectively, where all the possible choices of parameters ξ and β have been considered, in order to show the relevant differences.

ξ	β	l_0 [mm]	N_{int}	Q_i [N]	Q [N]
1.4303	0.5	45.86	6	29447	176682
2	0.5	64.13	4	32747	130989
2.52875	0.3023	81.08	4	31037	124148
3	0.3333	96.2	3	32747	98242
3.58639	0.2212	114.99	2	31641	63282
4	0.25	128.26	2	32747	65495

Table 1. Analytical results for the example of [Genna and Gelfi 2012b] with $k \rightarrow \infty$. $\Delta = 11.2$ mm; $F = 1050000$ N.

ξ	β	l_0 [mm]	N_{int}	Q_i [N]	Q [N]
1.4303	0.5	91.72	16	141345	2261514
2	0.5	128.26	12	157187	1886244
2.52875	0.3023	162.16	9	148978	1340798
3	0.3333	192.4	8	157187	1257495
3.58639	0.2212	229.99	7	151878	1063143
4	0.25	265.51	6	157187	943122

Table 2. Analytical results for the example of [Gelfi and Metelli 2007] with $k \rightarrow \infty$. $\Delta = 60$ mm; $F = 5040000$ N.

It is apparent that the total thrust Q takes values in a quite large range, even though the unit thrust Q_i does not depend much on the considered configuration. Adopting the proposed values for ξ and β ($\xi = 3$, $\beta = 1/\xi = 0.3333$), the error on the most interesting quantity, i.e., the total lateral thrust Q , is of the order of 0.02 in the worst case, which appears satisfactory, under the circumstances.

5. Conclusions

New calculations have been developed for the problem of the buckling of an elastic compressed beam restrained by unilateral frictionless contact against rigid surfaces that can translate elastically with respect to each other. Special attention has been devoted to devising a technique for obtaining directly the wave number and the associated thrust produced by the beam, when in contact against the rigid surfaces, for a prescribed value of the axial shortening. Even though some analytical results could be obtained, it appears that a precise calculation of the current number of buckled waves, and thus of the total lateral thrust, is impossible. Several alternative configurations can in principle occur under the same axial load, and the one actually followed depends on the existing imperfections, which can not be defined with precision.

With reference to the design of BRBs, the calculations developed herein lead to conclude that a good engineering choice is to enforce as strongly as possible a rigid constraint between the rigid surfaces, and that, also in view of the likely preference of buckled shapes for nonsymmetric configurations, a good choice for the coefficient ξ of the equation (3-11) governing the wavelength should be $\xi = 3$. The comparison with some numerical simulations has shown that, in this way, reasonably accurate results can be found under the assumptions of validity of the theory herein developed.

It is worth remarking that the choice $\xi = 3$ provides a relationship, between axial force and buckled wavelength, that implies an axial force 9 times larger than the one given by Euler's formula (see (3-12)), which is obviously not applicable in this situation.

The obtained results should constitute a starting point for the engineering design of BRBs, although the real situation, with BRBs, includes plastic deformations, contact with friction, and cyclic loading. Further work, based on the results herein presented, will tackle these more general aspects.

Acknowledgements

The authors wish to thank Dr. Giovanni Metelli of the Department of Civil Engineering, University of Brescia, for several useful discussions.

References

- [Alart and Pagano 2002] P. Alart and S. Pagano, "Confined buckling of inextensible rods by convex difference algorithm", *C. R. Mécanique* **330**:12 (2002), 819–824.
- [Bregoli 2014] G. Bregoli, *Studio di dispositivi in acciaio per il miglioramento sismico di edifici in c. a.*, Ph.D. Thesis, Dept. Civil Engineering, University of Brescia, 2014.
- [Chai 1998] H. Chai, "The post-buckling response of a bi-laterally constrained column", *J. Mech. Phys. Solids* **46**:7 (1998), 1155–1181.
- [Chai 2001] H. Chai, "Contact buckling and postbuckling of thin rectangular plates", *J. Mech. Phys. Solids* **49**:2 (2001), 209–230.
- [Chai 2002] H. Chai, "On the post-buckling behavior of bilaterally constrained plates", *Int. J. Solids Struct.* **39**:11 (2002), 2911–2926.

- [Domokos et al. 1997] G. Domokos, P. Holmes, and B. Royce, “Constrained Euler buckling”, *J. Nonlinear Sci.* **7**:3 (1997), 281–314.
- [Gelfi and Metelli 2007] P. Gelfi and G. Metelli, “Prova sperimentale di un elemento diagonale di controvento ad instabilità controllata”, in *Proceedings, XXI Congresso C.T.A.: Costruire con l'acciaio*, 1–3 October 2007, Catania, Italy, 169–176 (2007).
- [Genna and Gelfi 2012a] F. Genna and P. Gelfi, “Analysis of the lateral thrust in bolted steel buckling-restrained braces, 1: Experimental and numerical results”, *J. Struct. Eng. (ASCE)* **138**:10 (2012), 1231–1243.
- [Genna and Gelfi 2012b] F. Genna and P. Gelfi, “Analysis of the lateral thrust in bolted steel buckling-restrained braces, 2: Engineering analytical estimates”, *J. Struct. Eng. (ASCE)* **138**:10 (2012), 1244–1254.
- [Hibbitt et al. 2013] D. Hibbitt, B. Karlsson, and P. Sorensen, *ABAQUS user's manuals*, Release 6.13, Dassault Systèmes/Simulia, Providence, RI, 2013, <http://50.16.176.52/v6.13>.
- [Holmes et al. 1999] P. Holmes, G. Domokos, J. Schmitt, and I. Szeberényi, “Constrained Euler buckling: an interplay of computation and analysis”, *Comput. Methods Appl. Mech. Eng.* **170**:3–4 (1999), 175–207.
- [Muradova and Stavroulakis 2007] A. D. Muradova and G. E. Stavroulakis, “A unilateral contact model with buckling in von Kármán plates”, *Nonlinear Anal. Real World Appl.* **8**:4 (2007), 1261–1271.
- [Pocheau and Roman 2004] A. Pocheau and B. Roman, “Uniqueness of solutions for constrained Elastica”, *Physica D* **192**:3–4 (2004), 161–186.
- [Roman and Pocheau 2002] B. Roman and A. Pocheau, “Postbuckling of bilaterally constrained rectangular thin plates”, *J. Mech. Phys. Solids* **50**:11 (2002), 2379–2401.
- [Tzaros and Mistakidis 2011] K. A. Tzaros and E. S. Mistakidis, “The unilateral contact buckling problem of continuous beams in the presence of initial geometric imperfections: an analytical approach based on the theory of elastic stability”, *Int. J. Non-Linear Mech.* **46**:9 (2011), 1265–1274.
- [Villaggio 1979] P. Villaggio, “Buckling under unilateral constraints”, *Int. J. Solids Struct.* **15**:3 (1979), 193–201.

Received 21 Mar 2014. Revised 15 Apr 2014. Accepted 28 Apr 2014.

FRANCESCO GENNA: francesco.genna@unibs.it

Department of Civil Engineering, University of Brescia, Via Branze, 43, I-25123 Brescia, Italy

GUIDO BREGOLI: g.bregoli@unibs.it

Department of Civil Engineering, University of Brescia, Via Branze, 43, I-25123 Brescia, Italy

SUBMISSION GUIDELINES

ORIGINALITY

Authors may submit manuscripts in PDF format online at the Submissions page. Submission of a manuscript acknowledges that the manuscript is original and has neither previously, nor simultaneously, in whole or in part, been submitted elsewhere. Information regarding the preparation of manuscripts is provided below. Correspondence by email is requested for convenience and speed. For further information, write to contact@msp.org.

LANGUAGE

Manuscripts must be in English. A brief abstract of about 150 words or less must be included. The abstract should be self-contained and not make any reference to the bibliography. Also required are keywords and subject classification for the article, and, for each author, postal address, affiliation (if appropriate), and email address if available. A home-page URL is optional.

FORMAT

Authors can use their preferred manuscript-preparation software, including for example Microsoft Word or any variant of $\text{T}_{\text{E}}\text{X}$. The journal itself is produced in $\text{L}^{\text{A}}\text{T}_{\text{E}}\text{X}$, so accepted articles prepared using other software will be converted to $\text{L}^{\text{A}}\text{T}_{\text{E}}\text{X}$ at production time. Authors wishing to prepare their document in $\text{L}^{\text{A}}\text{T}_{\text{E}}\text{X}$ can follow the example file at www.jomms.net (but the use of other class files is acceptable). At submission time only a PDF file is required. After acceptance, authors must submit all source material (see especially Figures below).

REFERENCES

Bibliographical references should be complete, including article titles and page ranges. All references in the bibliography should be cited in the text. The use of $\text{BibT}_{\text{E}}\text{X}$ is preferred but not required. Tags will be converted to the house format (see a current issue for examples); however, for submission you may use the format of your choice. Links will be provided to all literature with known web locations; authors can supply their own links in addition to those provided by the editorial process.

FIGURES

Figures must be of publication quality. After acceptance, you will need to submit the original source files in vector format for all diagrams and graphs in your manuscript: vector EPS or vector PDF files are the most useful. (EPS stands for Encapsulated PostScript.)

Most drawing and graphing packages—Mathematica, Adobe Illustrator, Corel Draw, MATLAB, etc.—allow the user to save files in one of these formats. Make sure that what you're saving is vector graphics and not a bitmap. If you need help, please write to graphics@msp.org with as many details as you can about how your graphics were generated.

Please also include the original data for any plots. This is particularly important if you are unable to save Excel-generated plots in vector format. Saving them as bitmaps is not useful; please send the Excel (.xls) spreadsheets instead. Bundle your figure files into a single archive (using zip, tar, rar or other format of your choice) and upload on the link you been given at acceptance time.

Each figure should be captioned and numbered so that it can float. Small figures occupying no more than three lines of vertical space can be kept in the text (“the curve looks like this:”). It is acceptable to submit a manuscript with all figures at the end, if their placement is specified in the text by means of comments such as “Place Figure 1 here”. The same considerations apply to tables.

WHITE SPACE

Forced line breaks or page breaks should not be inserted in the document. There is no point in your trying to optimize line and page breaks in the original manuscript. The manuscript will be reformatted to use the journal's preferred fonts and layout.

PROOFS

Page proofs will be made available to authors (or to the designated corresponding author) at a Web site in PDF format. Failure to acknowledge the receipt of proofs or to return corrections within the requested deadline may cause publication to be postponed.

Journal of Mechanics of Materials and Structures

Volume 9, No. 4

July 2014

- Random vibration of shear deformable FGM plates** **VEDAT DOGAN 365**
- Mechanical behavior of brick masonry panels under uniaxial compression**
HACER BILIR ÖZHAN and ISMAIL HAKKI CAGATAY 385
- Collapse mechanisms of metallic sandwich structures with aluminum foam-filled corrugated cores** **BIN HAN, LEI L. YAN, BO YU, QIAN C. ZHANG, CHANG Q. CHEN and TIAN J. LU 397**
- Representative volume element in 2D for disks and in 3D for balls** **NATALIA RYLKO 427**
- Small amplitude elastic buckling of a beam under monotonic axial loading, with frictionless contact against movable rigid surfaces**
FRANCESCO GENNA and GUIDO BREGOLI 441



1559-3959(2014)9:4;1-6